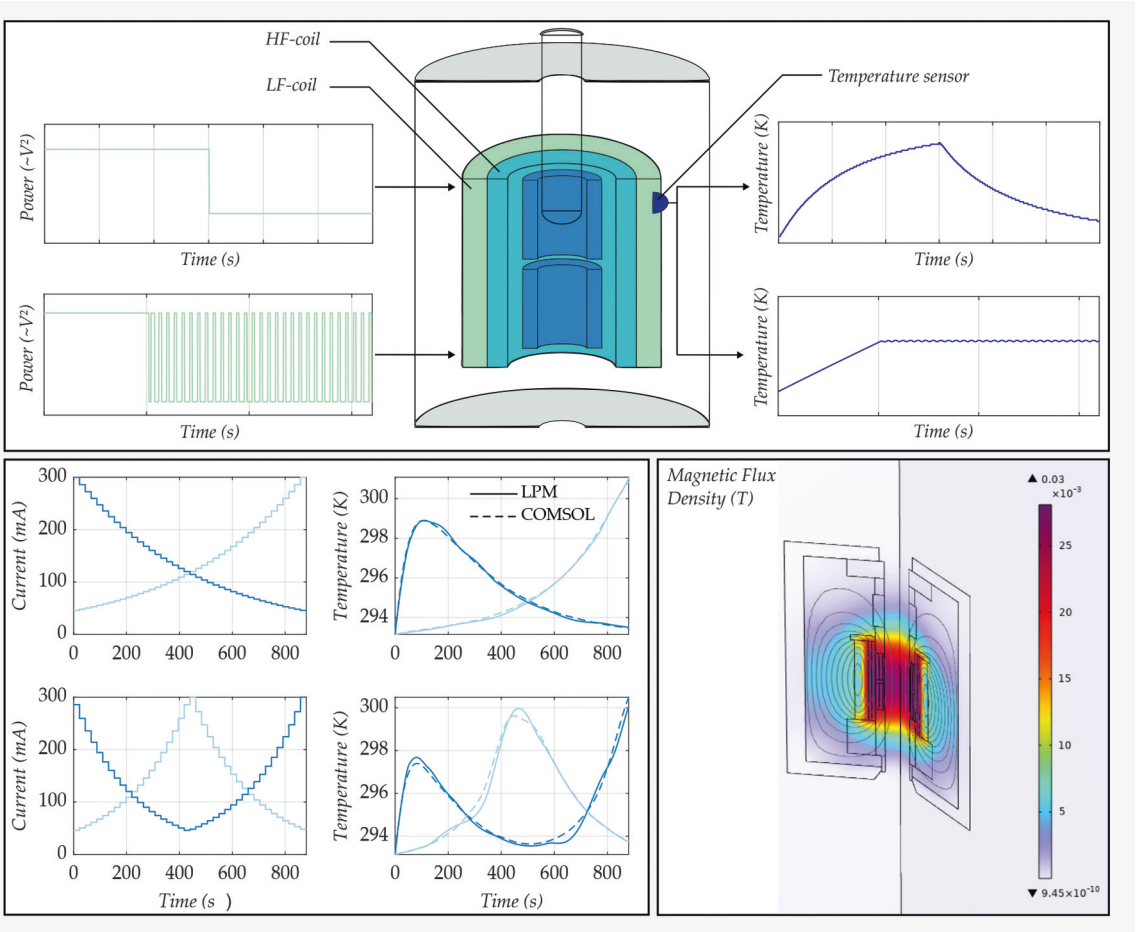

Temperature Influences on Frequency Mixing Magnetic Detection for mobile Drinking Water Analysis in Crisis Areas

Max Jessing

Information
Band / Volume 125
ISBN 978-3-95806-902-2

Mitglied der Helmholtz-Gemeinschaft

JÜLICH
Forschungszentrum

Schriften des Forschungszentrums Jülich
Reihe Information / Information Band / Volume 125

Forschungszentrum Jülich GmbH
Institut für Biologische Informationsprozesse (IBI)
Bioelektronik (IBI-3)

Temperature Influences on Frequency Mixing Magnetic Detection for mobile Drinking Water Analysis in Crisis Areas

Max Jessing

Schriften des Forschungszentrums Jülich
Reihe Information / Information Band / Volume 125

ISSN 1866-1777 ISBN 978-3-95806-902-2

Bibliografische Information der Deutschen Nationalbibliothek.
Die Deutsche Nationalbibliothek verzeichnet diese Publikation in der
Deutschen Nationalbibliografie; detaillierte Bibliografische Daten
sind im Internet über http://dnb.d-nb.de abrufbar.

Herausgeber und Vertrieb:	Forschungszentrum Jülich GmbH Zentralbibliothek, Verlag 52425 Jülich Tel.: +49 2461 61-5368 Fax: +49 2461 61-6103 zb-publikation@fz-juelich.de www.fz-juelich.de/zb
Umschlaggestaltung:	Grafische Medien, Forschungszentrum Jülich GmbH
Druck:	Grafische Medien, Forschungszentrum Jülich GmbH
Copyright:	Forschungszentrum Jülich 2026

Schriften des Forschungszentrums Jülich
Reihe Information / Information, Band / Volume 125

D 82 (Diss. RWTH Aachen University, 2026)

ISSN 1866-1777
ISBN 978-3-95806-902-2

Vollständig frei verfügbar über das Publikationsportal des Forschungszentrums Jülich (JuSER)
unter www.fz-juelich.de/zb/openaccess.

Abstract

The field of biomarker detection is constantly in search of novel methods to improve speed of detection, measurement accuracy, lower detection limits, specificity and applicability in mobile settings without the need for trained personnel. Most existent techniques like microbiological analysis, cell culturing, but also more novel techniques with electrical readouts suffer from either slow response time, are expensive or need well-trained operators. Very fast response lateral flow assays on the other hand, often show false negative results due to a lack of specificity. Furthermore, a plethora of, e.g., fluorescence-based techniques cannot be used in turbid samples like waste water or blood and require excessive sample pre-treatment.

The global covid pandemic and the German Ahrtal flooding in 2021 are just some vivid examples of quickly evolving outbreaks and disasters of our time. Such crisis scenarios have taught us once and again that quick, safe and mobile Point of Care Testing (PoCT) is needed.

For biomarker detection, the **F**requency **M**ixing **M**agnetic **D**etection (FMMD) technology provides a useful combination of advantages with its very high specificity, fast response times and mobile applicability. FMMD relies on the utilization of magnetic nanoparticles (MNP)s bound to the analyte of interest as magnetic markers which further provides highly selective signal acquisition. The readout of the magnetic particle signal in this magnetic immunoassay (MIA) upon application of two distinct magnetic excitation fields offers potential for multiplexed signal acquisition.

However, the requirements in actual disaster situations go further than the 'potential benefits' of a technology. Applicability and accuracy despite harsh conditions outside the lab, very low susceptibility to errors by untrained users and low false negatives rates are crucial for on-site decision making and rapid detection of for example a pathogen. FMMD is sensitive to changes in temperature due to the signal-dependency on a biological reaction, the magnetization behavior of the magnetic markers and the Ohmic resistance of the miniaturized induction coil environment.

Consequently, we mimic in-field rather than lab-based conditions to investigate the thermal dependencies of different aspects of the FMMD signal acquisition. We found indication of diverse signal variation depending on constant ambient temperature level. Therefore, aiming at finding optimal input excitation signals for thermal stability and signal-invariability, we further propose a methodology to test these input and ambient influences computationally. Our 3-parameter transient model utilizes non-integer order Padé approximations to follow the thermal dynamics of the FMMD sensor unit. The incorporation of Joule heating feedback emphasizes physical significance of the model. A cross-identification with finite element analysis (FEA) in COMSOL promises potential for thermal and electromagnetic

property analysis and sensor design.

Furthermore, it is possible to find low-frequency input schemes for the excitation fields of FMMD, that improve the accuracy of measuring biological probes while minimizing the measurement time. It also promises to reduce the error susceptibility for the magnetic reader user in terms of sample handling in PoCT and improves functionality in terms of sample preparation in the measurement head (MH).

Zusammenfassung

Im Forschungsfeld der Biomarker-Detektion ist man ständig auf der Suche nach neuartigen Methoden zur Verkürzung der Detektionszeit, Verbesserungen der Messgenauigkeit, niedrigerer Nachweisgrenzen, höherer Spezifität und besserer Anwendbarkeit in mobilen Umgebungen, ohne dass geschultes Personal erforderlich ist. Die meisten vorhandenen Verfahren wie mikrobiologische Analyse, Zellkultivierung, aber auch neuartigere Techniken mit elektrischer Signalerfassung haben den Nachteil langsamer Detektionszeit, sind teuer oder erfordern gut ausgebildetes Personal. Besonders schnelle Lateral-Flow-Assays hingegen können aufgrund mangelnder Spezifität falsch negative Ergebnisse liefern. Darüber hinaus kann eine Vielzahl von z.B. fluoreszenzbasierten Verfahren nicht bei trüben Proben wie Abwasser oder Blut eingesetzt werden, ohne dass eine Probenvorbehandlung notwendig ist.

Die globale Covid-Pandemie und die Überschwemmung im deutschen Ahrtal im Jahr 2021 sind nur einige anschauliche Beispiele für sich schnell entwickelnde Pandemien und Katastrophen unserer Zeit. Solche Krisenszenarien haben uns immer wieder gelehrt, dass schnelles, sicheres und mobiles PoCT benötigt wird.

Für die Biomarker-Detektion bietet die FMMD-Technologie mit ihrer sehr hohen Spezifität, schnellen Detektionszeiten und mobilen Anwendbarkeit eine nützliche Kombination von Vorteilen. FMMD beruht auf der Verwendung von MNPs als Marker, die an den Analyten gebunden sind, was außerdem eine hochselektive Signalerfassung ermöglicht. Die Auslesung des magnetischen Teilchensignals in diesem MIA bei Anwendung zweier unterschiedlicher magnetischer Anregungsfelder bietet Potenzial für die Erfassung von multiplex Signalen.

Die Anforderungen in tatsächlichen Katastrophensituationen gehen jedoch über den '*potenziellen Nutzen*' einer Technologie hinaus. Anwendbarkeit und Genauigkeit trotz rauer Bedingungen außerhalb des Labors, sehr geringe Fehleranfälligkeit für ungeschulte Nutzer und geringe Falsch-Negativ-Raten sind wichtig für die Entscheidungsfindung vor Ort und die schnelle Detektion z.B. eines Pathogens. FMMD reagiert empfindlich auf Temperaturänderungen aufgrund der Signalabhängigkeit von einer biologischen Reaktion, des Magnetisierungsverhaltens der magnetischen Marker und des Widerstands der miniaturisierten Induktionsspulenumgebung.

Folglich ahmen wir anwendungsnahe anstelle Labor-basierter Bedingungen nach, um die thermischen Abhängigkeiten verschiedener Aspekte der FMMD-Signalerfassung zu untersuchen. Wir fanden Hinweise auf sich ändernde Signalschwankungen in Abhängigkeit von konstanten Umgebungstemperaturniveaus. Um optimale Eingangs- bzw. Anregungssignale für thermische Stabilität und Signalinvariabilität zu finden, schlagen wir daher außerdem eine Methodik vor, um Eingangs- und Umgebungseinflüsse rechnerisch zu testen. Unser zeitabhängiges 3-Parameter-Modell nutzt nicht ganzzahlige Padé-Annäherungen, um der thermischen Dynamik der FMMD-Sensoreinheit zu folgen. Die Einbeziehung der

Rückkopplung von Joule-Erwärmung unterstützt die physikalische Bedeutung des Modells. Eine Kreuzidentifikation mit FEA in COMSOL verspricht Potenzial für die Analyse thermischer und elektromagnetischer Eigenschaften, sowie die Möglichkeit zum Sensordesign im Computer. Darüber hinaus is es möglich, niederfrequente Eingangsschemata für die Anregungsfelder von FMMD zu finden, welche die Genauigkeit bei der Messung biologischer Sonden verbessern und gleichzeitig die Messdauer minimal halten. Die Fehleranfälligkeit für den Nutzer des magnetischen Messgeräts in Bezug auf die Probenhandhabung in PoCT kann verringert werden und die Funktionalität in Bezug auf die Probenvorbereitung im MH kann verbessert werden.

List of Figures

List of Tables

List of Acronyms

AC alternating current

ACS AC suceptometry

AMF alternating magnetic field

BPF band pass filter

CCD charge-coupled device

CFU colony forming units

CV coefficient of variation

DAC digital to analog

DAQ data acquisition card

DC direct current

DDS direct digital synthesis

DE differential evolution

DNA desoxyribonucleic acid

dNTP desoxynucleotide triphosphate

EM electromagnet

EMF electromotive force

FEA finite element analysis

FEM finite element method

FFT fast fourier transform

FMMD **F**requency **M**ixing **M**agnetic **D**etection

GND ground

HF high frequency

IC integrated circuit

IFC immunofiltration column

IQR interquartile range

KDE kernel density estimate

LAMP loop mediated isothermal amplification

LF low frequency

LM Levenberg-Marquardt

LNA low noise amplifier

LoD Limit of Detection

LPF low pass filter

LPM lumped parameter model

MH measurement head

MIA magnetic immunoassay

MISO multi-input single-output

MNP magnetic nanoparticles

MPI magnetic particle imaging

MPS magnetic particle spectroscopy

MRI magnetic resonance imaging

NA nucleic acid

NASBA nucleic acid sequence based amplification

NP nanoparticles

NRMSE normalized root mean square error

PCB printed circuit board

PCR polymerase chain reaction

PEEK polyether ether ketone

PoC Point of Care

PoCT Point of Care Testing

PWM pulse width modulation

RCA rolling cycle amplification

RNA ribonucleic acid

RMSE root mean square error

RPA recombinase polymerase amplification

SEE standard error of estimate

SMD surface mounted device

SNR signal-to-noise-ratio

SPION superparamagnetic iron oxide nanoparticles

SPM superparamagnetic

SQUID superconducting quantum interference device

SSB single-stranded binding protein

ssDNA single-stranded desoxyribonucleic acid

STD standard deviation

TBE Tris Borate Ethylene Diamine Tetraacetic Acid

TEM transmission electron microscopy

TF transfer function

THW Technisches Hilfswerk

Contents

Chapter 1

Introduction

Drinking water hygiene is fundamental to modern civilization due to many known water-borne pathogens such as bacteria and viruses [1, 2, 3, 4], some of which are tied to lasting diseases [5, 6, 7, 8, 9]. In Europe and the Western world, clean drinking water is generally ensured through waste water treatment, good hygiene conditions, and advanced sanitation facilities [3]. But even in industrialized countries, disasters such as floods (flooding in Germany, Ahrtal, 2021) or droughts can occur. In such cases, sewage treatment plants may be flooded, and contaminated water may mix with drinking water or seep into the groundwater. Water treatment can consequently not be maintained. Accordingly, fast action must be taken to prevent the spread of disease waves. To do so, the first step is, to identify the germs present in order to be able to assess appropriate measures.

The Federal Agency for Technical Relief (THW [10]) is a German disaster relief organization operating both domestically and abroad. In addition to providing medical, technical, and logistical first aid, the THW also sets up a needs-based ad hoc infrastructure, organizes volunteers, and conducts drinking water testing. This is possibly followed by the installation of mobile purification plants. The standard method of the THW for conducting germination testing is a on-site cell culture technology combined with fluorescence dye detection using the Tecta® system from IDEXX [11]. The advantage of this technology is its particularly high sensitivity and low detection limits of just a few colony-forming units, in order to comply with German drinking water regulations. However, even with this sophisticated system, depending on the type of organism, it takes $24 - 72\,\mathrm{h}$ to determine a test result.

Therefore, it is of great interest to the THW to develop Point of Care (PoC) systems, that can be deployed mobily and detect germs selectively with a fast response time. Ideally, even multiple types of organisms can be quantified simultaneously. Furthermore, such a detection method should be quickly and safely usable even by untrained personnel. Accordingly, the susceptibility to errors in a single measurement should be kept very low during device usage, even under a wide range of environmental conditions.

In 2003, Quentin Pankhurst et al., reviewed versatile use-cases of MNPs in biomedical applications and discussed its manipulability by external magnetic field gradients at a distance [12]. Since then, a plethora of MNP use-cases have emerged. For example, MNPs can be coated with specific biological compounds to target a certain type of tissue and then be used in targeted drug delivery applications [13, 14, 15, 16]. Further, magnetic fluid hyperthermia applications are summarized in numerous reviews [17, 18, 19]. Especially in

cancer treatment, this methodology gains increasing attention [20, 21]. Additionally, MNPs find use in magnetic resonance imaging (MRI) or magnetic particle imaging (MPI), as contrast agents [22, 23, 24, 25] or are used for magnetic separation purposes after labelling biological components of interest [26, 27].

In magnetic bioassays, MNPs have also been utilized extensively as labeling agents [28, 29]. The magnetic core sizes of MNPs can be determined through different techniques. For example, core sizes can be deduced from the dynamic magnetic response, measured by highly sensitive and accurate superconducting quantum interference device (SQUID) technology [30], or optical techniques like transmission electron microscopy (TEM) can be used for direct size measurement. These approaches, however, underly severe drawbacks for the use in biological applications or in the field. TEM for example is used to investigate very small sample sizes, and requires destructive sample preparation (sputtering). SQUIDs are typically cooled by liquid helium (−269 °C) or liquid nitrogen (−196 °C), which makes the development of portable devices currently impossible. Additionally, with increasing temperature, sensitivity decreases [31]. Alternative induction-based methods, like for example MPS [28] or related techniques, that can be provided in compact, portable PoC format [32, 33] and be applied at room temperature-like conditions, are way more suited for field applications. Due to the insensitivity of the magnetic signal readout towards sample turbidity, the magnetic bioassays can be applied in complex sample matrices like blood, serum or waste water, still promising highly selective signals. Using optical readout techniques, extensive sample pre-treatment would otherwise be necessary for such samples.

Besides applicability to turbid samples, the '*multiplex potential*' is a crucial factor in the selection of a suitable technique for the detection of pathogens in waste water. The concurrent quantification or so-called particle colorization refers to the capability to distinguish multiple differently sized magnetic nanoparticles in a single mixture [28, 34]. By introducing biological recognition elements of different kinds and binding them to the different particles, multiplexed magnetic bioassays become available [34, 35, 36, 37, 38, 39], which increases assay value and time-efficiency tremendously. However, it was reported that the Limit of Detection (LoD) can deteriorate by up to 3-fold in multiplexed bioassays [28]. Some effort has been taken to counteract the efficiency-loss - for example Orlov et al. suggested spatial separation of different magnetically labeled, single-plex lateral flow-assays [40] or Achtsnicht et al. presented staggered immunofiltration columns to achieve similar [41]. However, being able to detect and separate magnetic core sizes of different MNPs in a single solution stays challenging and to hold up to the sensitivity of their single-plex counterparts, accurate measurement becomes even more critical, when distinguishing nanoparticle sizes in multiplex solutions.

In the realm of magnetic bioassay sensing, MPS is an especially interesting candidate due to the relatively simple setup compared with SQUID, TEM etc.. One form of MPS is its dual-tone excitation variant, also called FMMD. FMMD is a relatively novel technique first published for MIAs in 2007 by Krause and Nikitin, independently [42], [43]. FMMD can, compared to MPS, measure additional harmonic frequencies due to the mixing of the two distinct input frequencies with the magnetic particle response. These additional mixing harmonics may provide further information about the magnetization state of the sample and may unravel magnetic behavior, that otherwise would be covered. The occurance of mixing harmonics therfore increases "the characterization potential" [44] to reconstruct magnetic core size distributions in mixed samples of multiple particles [44, 45, 46].

It has been shown that, besides well-defined and distinct magnetic properties, the number

of MNP types that can be distinguished from one another in a mixture is higher, as the signal-to-noise-ratio (SNR) improves [34]. Moreover, few articles discuss MPS and MPI signal behavior upon sample exposure to different thermal conditions, which is especially important in PoC applications. The ones that do, found significant influence of e.g. temperature on detection signal phase and amplitude even for small variation in sample temperature ($\sim 5 - 20\,^{\circ}\mathrm{C}$) [47],[48] based on a variety of factors. It has been discussed, e.g., what effect the sample state (suspension, freezed dried) has on the observed signal at different temperatures [49]. Some studies have even investigated magnetic nanothermometry to determine a sample temperature based on signal changes in MPS and related techniques, which also clearly indicates a dependency [50, 51, 52]. In these studies, mostly the harmonic signals in MPS are explored at single, stable temperatures, rather than under the continous influence of unsteady environmental or transient sample temperature conditions. Also, in literature, we did not find a simple and practical solution to stabilize measurements against thermal influences, without compromising the response time of the system. The response time is influenced either by necessary preheating times, or, depending on the ambient temperature, extensive '*off-time*' of '*simple*' thermal regulators to passively cool down the device. Therefore, the prevention of drift in the signal and background is of utmost importance, especially for '*in-field*' applications.

So far, these drifts have only been examined under controlled laboratory conditions. More specifically only different constant sample temperatures were considered, transient change or ambient temperature influence was not discussed. The temperature dependence of the magnetization curves is adequately described in the literature [53, 54, 55, 56]. However, the combinatorial influence of this particle-temperature dependency, with time-varying coil resistances, temperature behavior of the bioassay carried out and transient change in sample temperatures, must also be taken into account. This holds especially true in a PoC environment. To optimize the sensitivity and accuracy of MPS, effort has been taken towards frequency and amplitude optimization and their effect on different types of MNPs [57]. Further, permanent ring magnets were suggested for offset-field application in FMMD as a *thermally independent* option to not incur changes of the FMMD signal based on additional heat introduced by external electromagnets. While this supresses additional heat introduced by the offset-field, this approach makes FMMD "un"portable, it is not automatized and not user-friendly as stated by the authors [58]. In comparison, our aim is amongst others to optimize the amplitudes selected in a FMMD measurement from a thermal and measurement duration view point in a mobile, safe and user-friendly setup.

Therefore, this work contributes to better understanding the FMMD system in an environment with continously changing temperature conditions and to finding strategies for prevention of thermal influences based on the selected measurement input signals that minimize measurement downtime in the field. Besides providing evidence and magnitude for the influence of temperature changes on different aspects of the FMMD signal, we have investigated, whether there is a clear pattern in the temperature dependence of the harmonic FMMD signals, based on the separate factors that influence response time and measurement accuracy mentioned in the previous sections. Besides exploration of the drift of excitation amplitudes in chapter 3, we recorded the FMMD responses for immunoassays at different constant ambient conditions and the harmonic FMMD signals for unmodified MNPs (see chapter 4). We followed a model-based approach to finding the optimal LF voltage inputs that keep measurement downtime minimal, while causing little thermal fluctuation in the entire measurement system, including the MNP sample (chapter 5). In this course, we also investigated, whether simple temperature regulation algorithms suffice for delicate biological applications that require accurate thermal control for optimized

enzymatic reaction conditions [59] (chapter 6).

This work is part of the NANObeST project [60]. NANObeST set the aim to develop equipment for pathogen detection in drinking water in collaboration with the THW. The developed equipment (magnetic reader) should be usable on-site by unspecialized personell. Besides this project, there is many further possible areas of application for the FMMD device, as for example the testing of plant viruses [61], mycotoxins [62] or the usage on animal farms for *brucella* DNA detection [63]. Due to its independence on sample turbidity also application in medical PoC analysis of blood and serum is possible [64].

Chapter 2

Theoretical Background

2.1 Basics of Magnetic Materials

Each atom creates a tiny magnetic field, that originates from the intrinsic spin of its electrons and their motion around the nucleus. The product of current I circulating around an area A, $m = I \cdot A \cdot \vec{n}_A$ with $\vec{n}_A$ being a vector normal to the plane, is called the the *magnetic dipole moment* $\boldsymbol{m}$. By the superposition of the electron spin and orbital motion, the resulting magnetic moment might be zero. The magnetization of a material corresponds to the sum of all magnetic dipole moments per unit *volume* $\boldsymbol{V}$ [65].

$$M = \frac{1}{V} \sum_{n=1}^{N} m_n \tag{2.1}$$

The SI units in which $\boldsymbol{M}$ is typically measured are Am^{-1} (amperes per meter). Mind that the magnetization $\boldsymbol{M}$ is a vector sum of all magnetic dipole moments and therefore is a vector quantity itself [66]. Following the so-called continuum approximation, the quantity $\boldsymbol{M}$ does not account for any local magnetic moment variations within a material [66]. However, in terms of their magnetic behavior, materials are usually characterized by applying an *external magnetic field* $\boldsymbol{H}$ and measuring the material's *magnetization response* $\boldsymbol{M(H)}$ as $\boldsymbol{H}$ changes. For most materials (e.g. dia-, para- and superpara-magnets) it holds, that in the absence of $\boldsymbol{H}$, the magnetic dipole moments are randomly oriented, resulting in a net magnetization of zero. The more magnetic dipole moments align in a certain volume, the larger the magnetization of the material within that volume. The torque that needs to be created in order for the magnetic moments to align, depends firstly on the strength and orientation of $\boldsymbol{H}$ and secondly on the relative orientation (angle) of the magnetic dipole moments to $\boldsymbol{H}$.

Depending on how the magnetic moment of a collection of atoms in a volume changes based on the externally applied field, the material can mainly be classified into one of four categories: Diamagnets, paramagnets, ferromagnets and superparamagnets (Antiferro -and Ferrimagnets will not be discussed in this work). Dia- and paramagnets mostly obey a linear dependency of the magnetization with respect to external field strength, following:

$$M = \chi \cdot H \tag{2.2}$$

where the proportionality constant $\boldsymbol{\chi}$ is the magnetic susceptibility which generally determines how magnetizable a material is. If $\boldsymbol{\chi} > 0$ the material under test is a paramagnet. If $\boldsymbol{\chi} < 0$ the material under test is a diamagnet. In response to small $\boldsymbol{H}$ all materials respond according to equation (2.2). However, ferromagnets and superparamagnets exhibit a nonlinear magnetization response for larger external fields ($\boldsymbol{H > H_{linear}}$). If $\boldsymbol{H}$ becomes even larger all magnetic moments align and the magnetization response reaches magnetic saturation $\boldsymbol{M_s}$. The magnitude of the externally applied field, that is needed to drive these types of magnets into their nonlinear regime or saturation, depends on the size of the investigated material.

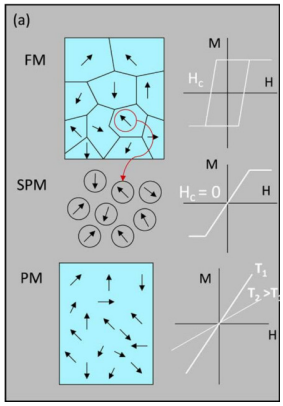

Figure 2.1: Shows the general domain structure of ferromagnetic materials (a), and the magnetic moment orientations without of superparamagnetic particles (b) and paramagnetic material (c) in the absence of an external magnetic field [67].

In this nonlinear case, $\boldsymbol{\chi}$ depends on $\boldsymbol{H}$ and the magnetization behavior does not follow (2.2) anymore (which will be described based on the magnetization behavior of a ferromagnetic material in section 2.1.1).

A second field-quantity, *magnetic induction* $\boldsymbol{B}$ arises, when the contribution of the material itself to the overall magnetic orientation is considered. In linear, isotropic and homogeneous (LIH) materials, $\boldsymbol{H}$ and $\boldsymbol{B}$ are generally tied to one another by $\boldsymbol{B = \mu \cdot H}$. The *magnetic permeability* $\boldsymbol{\mu}$ determines how well a magnetic force can be exerted within a certain material. $\boldsymbol{\mu}$ is measured in Hm^{-1} (henry per meter) and follows:

$$\mu = \mu_0 \cdot (1 + \chi) \tag{2.3}$$

where $\boldsymbol{\mu_0}$ is the permeability of free space ($\boldsymbol{\mu_0} = 4\pi \cdot 10^{-7}\mathrm{Hm}^{-1}$) and $\boldsymbol{1 + \chi}$ is also called the relative permeability $\boldsymbol{\mu_r}$. While $\boldsymbol{\mu_0}$ is a magnetic constant, $\boldsymbol{\mu_r}$ is a characteristic measure of a respective material, that determines its magnetic response to external fields. Considering the magnetization $\boldsymbol{M}$ as part of the intrinsic field contribution of the material, the relation between $\boldsymbol{M}$, $\boldsymbol{H}$ and $\boldsymbol{B}$ is:

$$B = \mu_0 \cdot (H + M) \tag{2.4}$$

$\boldsymbol{B}$ is measured in T (Tesla) and describes the response of a material to an externally applied magnetic field $\boldsymbol{H}$.

The four types of magnetism are extensively discussed in literature [65], [66], [68]. However, for the sake of clarity of the applied techniques in this work, the most important aspects of ferro- and superparamagnetism will be summarized in the following sections.

2.1.1 Ferromagnetism

Once magnetized by an external magnetic field $\boldsymbol{H_s}$ larger or equal to a field that drives the material into saturation magnetization $\boldsymbol{M_s}$, ferromagnetic materials like iron, nickel, cobalt and magnetite show a permanent magnetization, even in the subsequent absence of an external field. While in most other materials, the magnetic moments are randomly directed and eliminate each others effect, ferromagnetism originates from the formation of magnetic domains within ferromagnetic materials. Domains are also called Weiss' domains and are regions in the material, where the magnetic dipole moments are aligned in parallel and thus the $\sum_{n=1}^{N} m_n \neq 0$. In a neighboring domain, the magnetic moment sum is also unequal zero, but the resulting magnetic moment direction in this domain may differ from the previous one. The uniform magnetic moment orientation within a single domain arises from the tendency to reach an energetically favorable state depending on short-ranged spin interactions, the so-called exchange interactions [21]. The magnetic moment sum of the domains is randomly distributed within a collection of domains, such that in an unmagnetized state the net magnetization is zero. By applying a sufficiently high external magnetic field, it is possible to drive all domains into alignment. For some materials, like the above-mentioned, the majority of domain alignment persists, after removing the external field, leading to a permanent magnetization of the material. The flipping of whole domains instead of single magnetic moments upon the application of an external field, expresses in the form of so-called Barkhausen steps in the linear regime of the magnetization curve. The magnetization curve of such materials is nonlinear and has a hysteresis (figure 2.2)[68].

Figure 2.2 shows the magnetization behavior plotted against the applied external field and the respective sum magnetic moment orientation in individual exemplary domains of a ferromagnetic material. Initially, at $\boldsymbol{H = 0}$, the magnetic dipole moments are randomly oriented. As $\boldsymbol{H}$ grows $\boldsymbol{> 0}$, the magnetization increases and the magnetic domains start aligning. For $\boldsymbol{H = H_s}$, the magnetization reaches its maximum value, where most or all domains are aligned with the external field. When $\boldsymbol{H}$ is turned off, the material stays magnetized at a value slightly lower than $\boldsymbol{M_s}$, which is called the remnant magnetization $\boldsymbol{M_r}$. It is possible to reach $\boldsymbol{M = 0}$ within the ferromagnet again, given that $\boldsymbol{H}$ at the strength of the so-called coercivity field $\boldsymbol{H_c}$ is applied in the opposite direction of the magnetization.

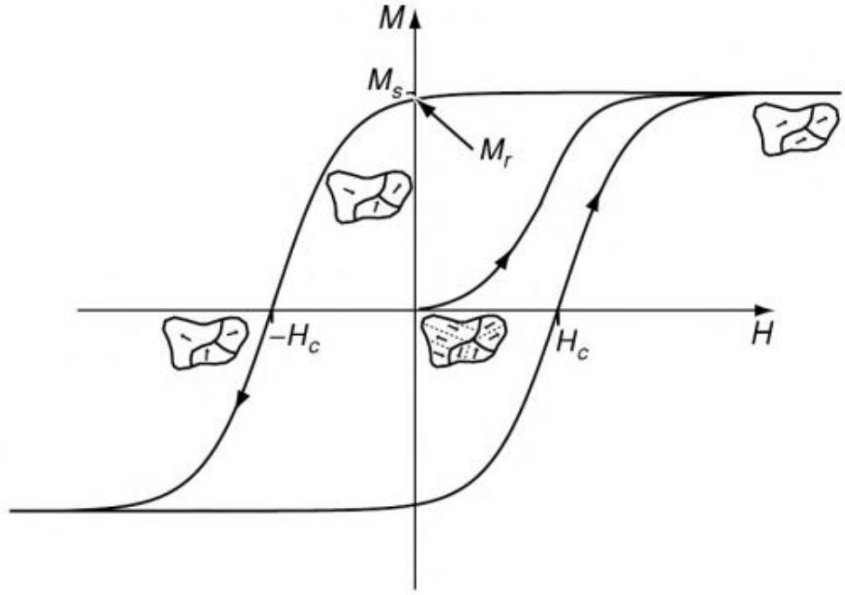

Figure 2.2: Schematic of a hysteresis loop magnetization Curve of a ferromagnetic material [68].

Besides this determined magnetization behavior, ferromagnetism is in fact temperature-dependent. When the thermal energy in the material becomes larger than the interaction energy of the magnetic moments inside the domains, the ferromagnetic behavior does no longer persist and turns into the behavior of a paramagnetic material. The temperature that is associated with the dominance of thermal energy is called the Curie-temperature T_C.

2.1.2 Superparamagnetism

Unless otherwise stated, this section will follow Alberto P. Guimaraes "Principles of Nanomagnetism" [69]. All equations in this chapter are specifically taken from [69].

When the size of a ferromagnetic material is reduced enough, it becomes superparamagnetic. We essentially speak of (typically) superparamagnetic iron oxide nanoparticles (SPION)s. The sizes that are reported to be superparamagnetic vary from a few nanometers up to 100 nm, depending on the literature considered [70, 71]. The reason for this variance in literature is, that superparamagnetism is not only size- but also material and temperature-dependent. In fact, when the superparamagnetic (SPM) regime is reached, the magnetization of the respective nanoparticles (NP)s can change its direction purely based on temperature. Additionally, whether superparamagnetic behavior is measured or not, it depends on how large the relaxation time of a magnetic particle is, relative to the measurement time.

For intuitive understanding, consider the following scenario. A collection of magnetized particles is placed at time $t = 0$ in an external field $H = 0$, but at a temperature $T \neq 0$. The sum magnetization of the collection will vary with time, as the thermal energy input ($T \neq 0$) activates energy state transitions. This time-varying magnetization can be described by:

$$\frac{dM}{dt} = -\frac{1}{\tau_0} M e^{-\frac{KV}{k_B T}} = -\frac{M}{\tau} \tag{2.5}$$

As part of this derivative, the relaxation time is described by the Néel-Arrhenius law:

$$\tau = \tau_0 e^{\frac{KV}{k_B T}} \tag{2.6}$$

τ_0 is the inverse of the energy transition attempt frequency, K is the anisotropy energy, V is the magnetic core volume, k_B is the Boltzmann constant and T is the temperature. The relaxation time describes the typical time between two magnetization flips. Note that the energy barrier to overcome for a change in magnetization is the anisotropy barrier KV and the thermal energy input to the system is described by $k_B T$. Thus, whether the relaxation time is large or small, strongly depends on the ratio of thermal energy, to anisotropy energy barrier height. Furthermore, if superparamagnetism is to be measured, the measurement time should be smaller than the relaxation time of the corresponding particles. If the time to measure the magnetization of the particles is much larger than the Néel relaxation time, their average value of magnetization appear to be zero. Thus, if $\tau < t_{measure}$, superparamagnetic behavior can be observed. If $\tau > t_{measure}$, the particles are in a blocked state, meaning a magnetization unequal to zero is observed.

Taking a large measurement time, e.g. $t_{measure} = 100s$ and a τ_0 of $10^{-9}s$ [69], it is possible to recalculate the critical volume (equation (2.7)) to be in superparamagnetic state via taking the logarithm and reformulating (2.6). The critical diameter (equation (2.8)) can than easily be obtained exemplarily for a certain material with spherical shape at a given temperature. These critical diameters vary, depending on the material.

$$V_{crit}^{spm} \approx \frac{25 k_B T}{K} \tag{2.7}$$

$$D_{crit}^{spm} = (\frac{6}{\pi} \cdot V_{crit}^{spm})^{\frac{1}{3}} \tag{2.8}$$

Neglecting the viscosity of the surrounding media of our hypothetical particle sample, with these critical diameters, an instantaneous response of the orientation of the SPIONs to an external magnetic field can be assumed. Following the concepts of randomly distributed magnetic moment orientations elaborated in section 2.1 and [65, 66, 67, 68], the response of superparamagnetic particles to varying $\boldsymbol{H}$ is visualized in figure 2.3.

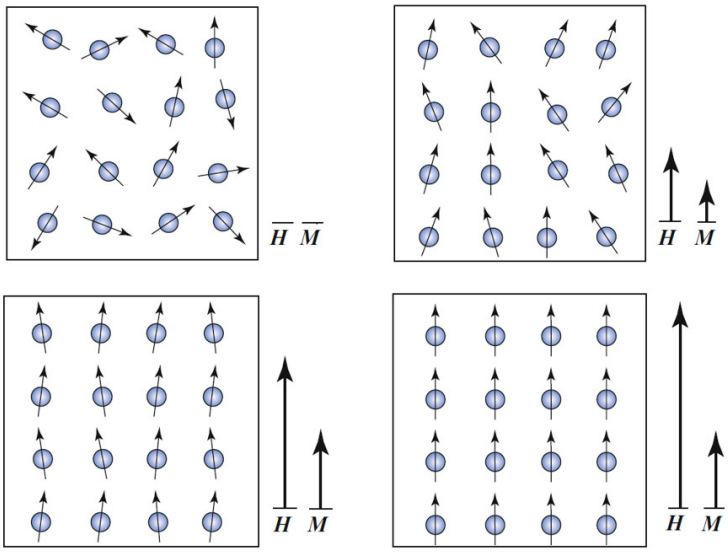

Figure 2.3: Schematic of the alignment of magnetic dipole moments and the total magnetization with respect to applied field [72].

The higher the externally applied field, the larger the magnetization response of the SPIONs until saturation magnetization is reached. Other than in larger ferromagnetic materials, however, when removing $\boldsymbol{H}$, the magnetization vanishes ($\boldsymbol{M(H = 0) = 0}$). Therefore, superparamagnetic magnetization is easily reversible by removing the external field, which makes the shape of its magnetization curve non-hysteretic. Typically the so-called Langevin function (2.9) is used to describe the magnetization's thermal behavior of magnetic nanoparticles in form of a non-hysteretic magnetization curve. As shown in figure 2.4, the Langevin function provides a clear indication for superparamagnetic instantaneous field-responsiveness.

$$M(H) = M_s \left(\coth\left(\frac{\mu H}{k_B T}\right) - \frac{k_B T}{\mu H} \right) \tag{2.9}$$

The argument of the Langevin function contains a dependency on magnetic field $\boldsymbol{H}$ and temperature $\boldsymbol{T}$.

Figure 2.4 shows the Langevin magnetization curve for a set of different temperatures (A) and for a set of different superparamagnetic particle sizes (B). As described in section 2.1, the necessary external magnetic field, that is needed to reach the nonlinear regime or saturation, depends on the particle size and temperature. As the temperature approaches the Curie temperature described in the previous section 2.1.1, the magnetization behavior gets closer to that of a paramagnetic material, generally like in the case of a ferromagnet. However, superparamagnetism is different in that it occurs far below the Curie temperature in the described size-regime.

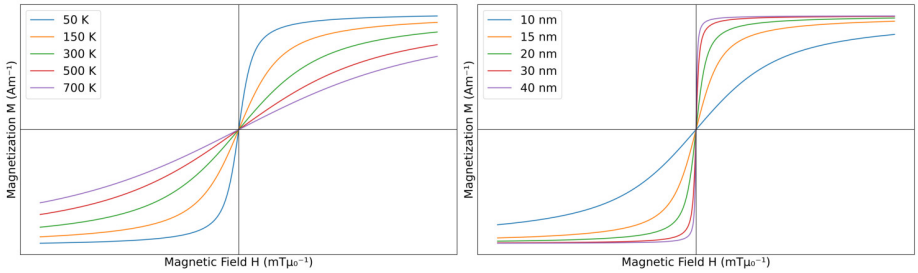

Figure 2.4: Magnetization curve of superparamagnetic materials based on the Langevin function for different temperatures (A) and different particle sizes (B).

2.2 Magnetic Particle Imaging

This Section is adopted and modified from Tobias Knopp and Thorsten M. Buzug [72]. Measurement techniques often make use of this instantaneous and reversible magnetization of superparamagnetic materials. This time-varying magnetization characteristic gives rise to the use of induction-based techniques. In practice, MPI is such a technology. In MPI, a first coil expresses a sinusoidal excitation signal (of the form shown in (2.10)), that excites superparamagnetic particles to flip their magnetic moments.

$$H(t) = H_e \cdot cos(2\pi f_e t) \tag{2.10}$$

The superposition of this excitation signal and the time-varying magnetization of the particles induces a voltage into a second coil, a receive or detection coil by means of Faraday's law of electromagnetic induction. The integral form of this law can be stated as (2.11).

$$\oint_S E(l)\, dl = -N \cdot \int_S \frac{\partial B(t)}{\partial t}\, dA = -N \cdot \frac{d}{dt}\Phi_s(t) \tag{2.11}$$

where the line integral of the electric field E along the length of a single wire loop S equals the number of wire loops in the detection coil N multiplied by Φ_s, the magnetic flux through the surface spanned by the wire loop. It can be seen, that Φ_s is the surface integral of the magnetic induction B described in (2.4) over the area A enclosed by the wire loop ($\Phi_s(t) = \int_S B(t)\, dA$). The left hand-side of (2.11) is also called the electromotive force (EMF), which is the work done on a charge in the wire loop. It equals the measurable induced voltage $U_{ind}(t)$ by definition as written in (2.12), equivalent to (2.11).

$$U_{ind}(t) = -N \cdot \frac{d}{dt}\Phi_s(t) \tag{2.12}$$

Since the induction voltage $U_{ind}(t)$ depends on both, the magnetic flux change induced by the excitation field and the magnetic flux change induced by the magnetic moment

flipping of the particles, it can also be expressed as the sum of the voltages induced by the excitation field and by the particles $U_{ind}(t) = U_e(t) + U_p(t)$. It is necessary to isolate the particle signal $U_p(t)$ from the excitation signal $U_e(t)$. It is important, that the non-linearity of the superparamagnetic magnetization curve in figure 2.4 is, what allows us to distinguish the excitation signal $U_p(t)$ from the particle signal $U_e(t)$. This is schematically shown in Figure 2.5.

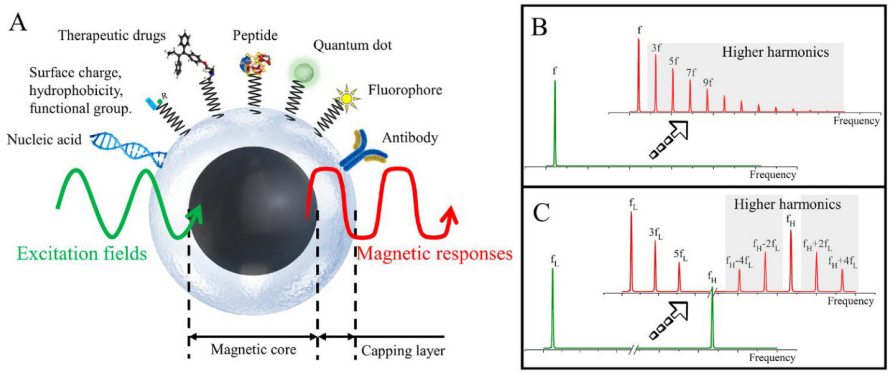

Figure 2.5: Illustration taken from [73] shows the principle of a MPS measurement. (A) shows a schematic of a magnetic nanoparticle, consisting of a magnetic core material and a matrix layer around it to bind diverse biological or chemical recognition molecules. A sinusoidal excitation magnetic field and the magnetic response of the particle is indicated. (B) shows the schematic FFT for a single excitation frequency, while (C) shows the FFT for the special case of MPS with dual frequency magnetic excitation. More information about the special case of dual-frequency excitation are given in section 2.3.

For small amplitudes of the sinusoidal excitation field H_e, the magnetization behavior of magnetic materials follows the linear relationship $\chi = \frac{M}{H}$, stemming from (2.2). If the nonlinear behavior of the magnetization curve is subject of investigation, however, a larger amplitude of H_e is necessary. Therefore, in MPI, typically excitation alternating magnetic field (AMF)s similar to $H_e \sim 20\text{mT}$ with frequencies f_e between 20kHz - 40kHz are utilized [21].

When MPI is not used as an imaging modality, but rather to detect the presence and characterize magnetic particles or even biological entities like proteins, nucleic acids, therapeutic drugs, bound fluorescence dyes or quantum dots [73], it is usually called MPS. The signal acquisition, investigation of influences and further developments of a MPS-like system are the topic of this work, therefore the spatial encoding or image reconstruction strategies for MPI respectively, will not be discussed and can be found elsewhere [74], [75], [76].

2.3 Frequency Mixing Magnetic Detection

2.3.1 Principle of Frequency Mixing Magnetic Detection

Frequency mixing magnetic detection (FMMD) can be viewed as a dual-tone mode of the previously discussed MPS technique, as it is also measuring the magnetic particle response in terms of an applied excitation stimulus [42]. However, in contrast to MPS, which uses a sinusoidal, single-tone AMF (see (2.10)) to excite a magnetic particle sample, FMMD utilizes a two-tone excitation strategy, by simultaneously applying two sinusoidal AMFs. This excitation field can be formulated as (2.13).

$$H(t) = H_1 \cdot cos(2\pi f_1 t) + H_2 \cdot cos(2\pi f_2 t) \tag{2.13}$$

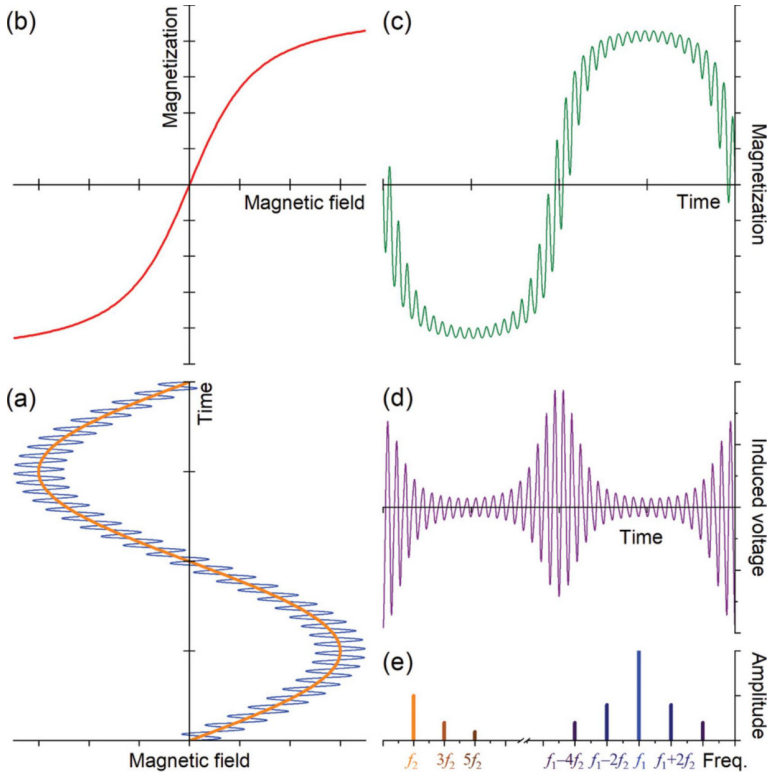

Figure 2.6: Illustration of the Frequency Mixing Magnetic Detection Principle taken from [77]. Figure (c) shows the magnetization response over time, containing mixing harmonics of superparamagnetic particles with nonlinear magnetization behavior (b) to high and low frequency excitation field sinusoids (a). (e) depicts the FFT of the induced voltage (d) resulting from the magnetization response with the spectral components of harmonic mixture.

In this strategy, a LF, high amplitude driving field component H_2, with frequency f_2 is

superimposed to a HF, low amplitude probing field component H_1, with frequency f_1. While the driving field is responsible to drive the MNPs into their nonlinear magnetization regime, the probing field is responsible to probe that nonlinear magnetization region. This leads to a discernible set of mixing harmonics in the response signal. These mixing harmonics at the sum and difference frequencies of the different excitation fields change as different particle concentrations and sizes are introduced to the measurement system. The principle of FMMD is shown graphically in figure 2.6.

The frequency selection of the driving and probing field components has some physical leeway. Typically, the frequency f_2 of the LF component is selected between 4-100 Hz, while f_1 of the HF component is selected as multiple 10ths of kHz. Besides factors like 50 Hz noise from power sources in Europe or 60 Hz in North America, the frequency selection depends on the used coil geometry and its resonance frequency. The higher LF AMF amplitudes the power electronics allow for, the smaller the particles, which can be driven into their non-linearity. However, typically LF-fields between $16 - 20\,\mathrm{mT}$ can be generated in mobile setups. The HF-field amplitudes are typically chosen around $1 - 2\,\mathrm{mT}$.

Review and explanation of the subtleties in FMMD technology can be looked up in the recently published review from Krause and Engelmann [77]. Mathematical derivation of the occurrence of additional harmonics when applying an additional static offset excitation-field, specifically in FMMD was first published by Krause et al. [42]. Additional literature on the intricacies of specific scanning modes for MPI and FMMD technology, e.g., the measurement using an additional offset magnetic field can be read upon elsewhere [45], [58, 78, 79, 80]. The usage of so-called measurement schemes as an excitation input will be discussed in section 5.2. Some applications using offset-scanning FMMD are also discussed in [78] and [58].

2.4 Heat Transfer

Unless otherwise stated, this section will follow concepts explained in [81], [82] and [83]. All thermal constants in this thesis are taken from [83, 84, 85, 86].

A very simple, yet general definition of heat transfer is provided in [87]: "Heat transfer or heat is thermal energy in transit, due to a spatial difference in temperature." The three transport laws that govern the ways of heat propagation are introduced in this section.

1. Conductive heat transfer described by Fourier's Law
2. Convective heat transfer described by Newtons law of cooling
3. Radiative heat transfer described by the Stefan-Boltzmann law

Generally, the topic of heat transfer provides ways to estimate and calculate heat transfer rates q and thus heat fluxes q''.

Before discussing heat transfer modes, some variables need to be explicitly defined, that otherwise may vary depending on the literature used. The definitions can be found in table 2.1.

Quantity	*Meaning*	*Symbol*	*Units*
Thermal Energy	Sum of kinetic energy associated with microscopic behavior in matter	U	J or $\frac{J}{kg}$
Temperature	A means of indirectly measuring the thermal energy stored in matter	T	°C or K
Heat	Amount of thermal energy that is transferred	Q	J
Heat Rate	Thermal energy transfer per unit time	q	W
Heat Flux	Thermal energy transfer per unit time and unit area	q''	$\frac{W}{m^2}$
Heat Generation Rate	Thermal energy generated per unit time and unit volume	$\dot{q}$	$\frac{W}{m^3}$

Table 2.1: Definition and units of important measures in heat transfer studies. This table was adopted from [83] and modified by Dr. Kody Powell.

2.4.1 Thermal Conduction

Typically, good electrical conductors are also good thermal conductors. Thermal conduction is associated with atoms in solids, fluids or gases, that become excited by heat and start vibrating. The vibration then effects neighboring atoms, which transfers the energy from regions of intense vibrations to regions of less intense vibrations, or in other terms, from hot to cold. Fourier's law describes the one-dimensional case of heat conduction. It can be seen in (2.14).

$$q''_x = -k \cdot \frac{dT}{dx} \tag{2.14}$$

, where q''_x is the heat flux in x-direction, k is the thermal conductivity which is a material property and $\frac{dT}{dx}$ is the change of temperature in x-direction. Although the thermal conductivity can be very small, depending on the material, it is always a positive number. Thus the negative sign belongs to the latter term. It exists, because heat always travels from hot to cold. In other words, if the temperature decreases in positive x-direction, q'' will be positive. If the temperature increases in positive x-direction however, q'' will be negative.

In practical applications, one often encounters complexities beyond the ideal assumptions of Fourier's law. Real-world materials might exhibit nonlinear behavior, where thermal conductivity varies with temperature. Furthermore, in composite materials, the differing conductivities of constituent materials add layers of complexity to heat conduction analysis.

2.4.2 Convection

Convection is a mode of heat transfer that occurs between an object in contact with a surrounding fluid. Lets consider a fan, installed perpendicular to a heated plate blowing air alongside it. The air will cool down the heated plate by "forced convection". Without a fan, however, convection might still occur based on a temperature difference within the fluid surrounding the heated plate. Here, we talk about "natural convection", where buoyancy-forces are the driving factor for creating the temperature differences in the fluid. These types of convection can also coexist in the form of "mixed convection". The heat rate due to convection can be expressed with Newton's law of cooling (2.15), regardless of the type of convection occurring.

$$q_{\text{conv}} = hA(T_s - T_\infty) \tag{2.15}$$

Here, q_{conv} is the heat rate due to convection. A is the normal area to the direction of the heat flow (similar to the area in any heat flux - perpendicular to the direction of heat flow), T_s is the surface temperature of the body and T_∞ is the temperature of the surrounding fluid by convention. The heat transfer convection coefficient h has the units $\frac{\text{W}}{\text{m}^2\cdot\text{K}}$, so that the heat rate due to convection q_{conv} is typically given in Watts. The convection coefficient h is determined by the fluid properties, the geometry of the object of interest, the flow regime (laminar, turbulent) and additional factors like the velocity of the surrounding fluid etc.

The complexity associated with convection therefore mostly evolves around determining the convection coefficient h. Generally, to determine h reliably, a thorough understanding of fluid mechanics is necessary. However, this is far beyond what will be discussed in this work.

Depending on the dimensionality of the problem at hand, simpler but significantly faster estimations of h can be performed by thermal resistance network analysis or dimensionless number correlations, ranging from general natural convection coefficient estimation [83] to specifically the determination of flow regime shifts in, e.g., vertical heated cylinders [88].

2.4.3 Radiation

Besides convection, radiation is another form of heat dissipation that can occur in systems. Other than convection, radiation can also occur in a vacuum. Generally, all bodies emit a temperature- and surface-dependent amount of energy in form of electromagnetic waves. A perfect radiator or "black body" can be described by the Stefan-Boltzmann law (2.16).

$$e_b(T) = \sigma T_b^4 \tag{2.16}$$

$e_b(T)$ is the emissive power of a black body. The subscript "b" indicates that here, it is specifically described for a black body. σ is the Stefan-Boltzmann constant ($\sigma = 5.670... \cdot 10^{-8} \frac{\text{W}}{\text{m}^2\text{K}^4}$). Since the absolute temperature in the Stefan-Boltzmann law is to the fourth power, radiation typically becomes less important for small temperature and more important for large temperature applications.

For most applications however, ideal radiators are not involved in heat transfer studies. Instead, ε is introduced as the surface emissivity of a body, a scaling factor for how emissive a surface is, so that $e(T) = \varepsilon e_b(T) = \sigma\varepsilon T$. Note that $e(T)$ is typically given in $\frac{\mathrm{W}}{\mathrm{m}^2}$, the same unit as the heat flux defined in 2.1. The counter part of ε is the surface absorptivity. In literature, the absorptivity is typically denoted with α, but since the thermal diffusivity will later be denoted with α, let us denote it as a. The absorption of thermal energy occurs, when a surface is irradiated with electromagnetic waves G and depends on the absorptivity of the surface. Alike $e(T)$, G is also given in $\frac{\mathrm{W}}{\mathrm{m}^2}$. Furthermore, it is not a single absolute temperature of the object that matters, but rather a temperature difference to the fourth power between the radiator and either another body or the surrounding media. The special case of *surface-to-ambient radiation* is of specific importance to this work, as a way of heat dissipation in large open surroundings. It can be assumed that the surroundings act as a black body, which leads to $G_{sur} = \sigma T_{sur}^4$.

As both, G and $e(T)$ are in $\frac{\mathrm{W}}{\mathrm{m}^2}$, the heat flux can then be expressed as (2.17)

$$q''_{\mathrm{rad}} = \varepsilon e(T) - aG \tag{2.17}$$

If we insert (2.16) into (2.17) and further assume that $\varepsilon = a$, the much simplified radiation rate equation becomes (2.18).

$$q_{\mathrm{rad}} = q''_{\mathrm{rad}} \cdot A = \varepsilon\sigma A(T_s^4 - T_{surr}^4) \tag{2.18}$$

Here, q_{rad} expresses the heat rate due to radiation and T_s and T_{sur} describe the temperatures of a surface-to-surroundings radiation process.

2.4.4 Steady State & Transient Formulation of Heat Transfer Problems

A special case of the first law of thermodynamics[1], if the state of matter does not change, is $q = \frac{dU}{dt} = mc\frac{dT}{dt} = \rho cV\frac{dT}{dt}$. This gives rise to the energy storage term in the time dependent formulation of any transient heat conduction problem.

In an energy balance, this would be the energy accumulation term of a small volume element $\Delta V = \Delta x\Delta y\Delta z$. The sum of the differences of all energy rates (flux times normal area) in and out of the control volume equal the sum of the fluxes times the respective areas plus a heat generation rate $\dot{q}$. Replacing the fluxes by Fourier's law separately in x,y and z direction and adding the special case of the first law of thermodynamics discussed above, one arrives at the general, *transient* three dimensional heat conduction equation written as (2.19).

$$\frac{\partial T}{\partial t} = \alpha\left(\frac{\partial^2 T}{\partial x^2} + \frac{\partial^2 T}{\partial y^2} + \frac{\partial^2 T}{\partial z^2}\right) + \dot{q} = \alpha\nabla^2 T \tag{2.19}$$

[1] Internal energy of a system has to be equal to the work being done by the system on its surroundings and the heat flowing into the system, $\dot{Q} = \dot{W} + \frac{dU}{dt}$, where $\dot{Q} = q$

where the thermal diffusivity α is a measure of the heat transfer rate inside a material, the definition of which is shown in (2.20).

$$\alpha = \frac{k}{\rho c_p} \tag{2.20}$$

with ρ, the density and c_p the specific heat capacity of the material.

From here, the stationary case for equation (2.19) can easily be reached by eliminating the time dependency of the problem ($\frac{dT}{dt} = 0$), in which case the object of interest also loses its ability to store heat. Sometimes, stationary studies can be helpful, when the temperature does not change, or even in simulations to get a rough estimation of the average convection coefficient h. However, most real systems obey a behavior that changes with time.

Fortunately, engineers and scientists today can apply many sophisticated software-strategies like COMSOL or FeniCs to avoid tedious or even impossible calculations and modelling by hand depending on the complexity of the problem of interest.

2.5 Nucleic Acid Amplification

In some applications, magnetically marked DNA can be detected using FMMD. In the working group of magnetic biosensors, Abuawad et al. reported magnetically labeled DNA assay design and detection utilizing FMMD to test for *Brucella* in livestock animals [63]. The analytes tested in these assays typically need up-concentration by polymerase chain reaction (PCR) before analysis can be performed. Amplification techniques like PCR require laboratories. Innovative technologies to replace this traditional DNA amplification approach help to facilitate this process and make it mobily accessible. Further, we see the potential for FMMD to be used to track reaction kinetics of labeled components in real-time. We tested the principles of DNA amplification in the MH unit of the magnetic reader in this work (see chapter 6). Therefore, this section will give an introduction to a popular isothermal alternative to PCR, the RPA. In general, whenever nucleic acid (NA) analysis lacks sensitivity to detect small amounts of material, when an excessive amount of NA material is needed for extended experimental studies and/or typically prior to any genotyping, the "amplification", or namely more accurate, "multiplication" of NA strands is of utmost importance. While the standard methodology to do so in a laboratory setting remains the PCR, many techniques have evolved to simplify, speed up and/or increase the yield of NA amplification.

2.5.1 Recombinase Polymerase Amplification

Over 20 years after the invention of PCR [2], RPA was developed by Piepenburg et al. in 2006 and commercialized by TwistDx™ [93]. RPA is a DNA amplification technique that

[2] In 1993, Karry B. Mullis was awarded with the noble prize for the 1983-invention of the PCR, a technology to amplify DNA. A mixture of the original DNA sequence to be amplified, dNTPs, the heat-resistant Taq-polymerase, primers and cofactors, participates in a sequence of well-controlled temperature shifts. These phases of the temperature cycle are called denaturation, annealing and elongation. Literature on the exact principle of PCR exists in excess and can be found elsewhere [89, 90, 91, 92]

does not require temperature cycling, but typically performs amplification at a constant temperature between 37-42°C. In other words, RPA is an isothermal NA amplification technique. Isothermal techniques carry the advantage of simplicity and make expensive temperature cycling equipment futile. The heating and cooling process in PCR requires a considerable amount of time, that can be saved in a RPA process, making it especially interesting for remote applications.

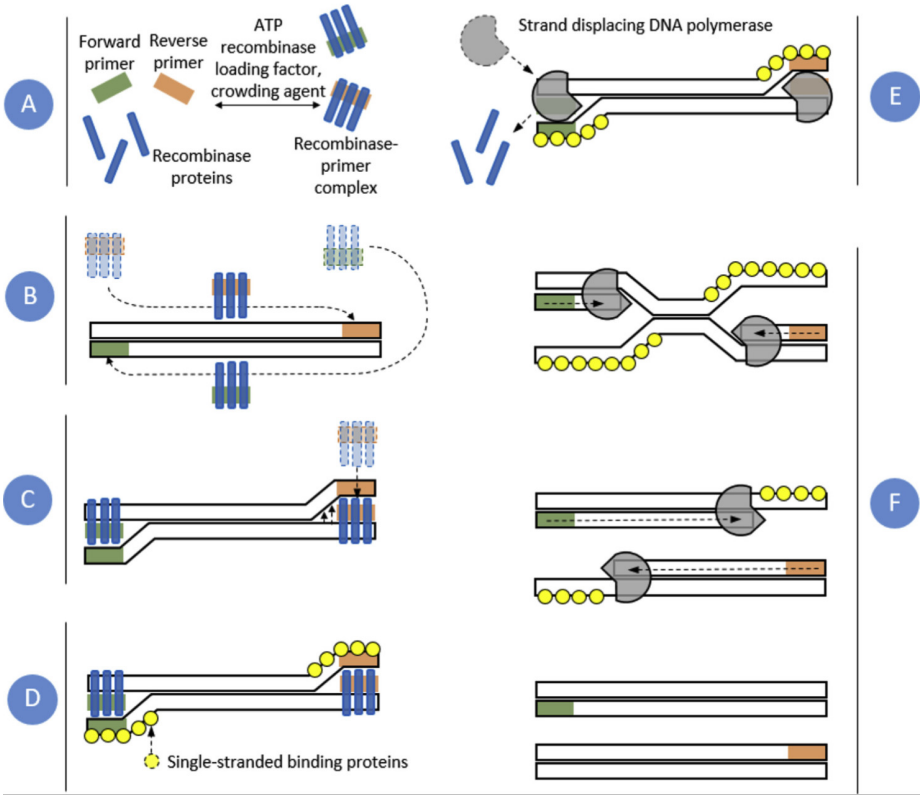

Figure 2.7: Schematic of the RPA process, including (A) formation of the recombinase-primer complex, (B) Scanning for homologue DNA sequences, (C) double helix opening and primer insertion at the complementary site, (D) single-strand stabilization by SSBs, (E) attachment of the DNA-polymerase and removal of the recombinase enzyme (F) elongation of the forward and reverse primer along the strand. [93]

In order to achieve this constant temperature procedure, additional enzymes are necessary to denature the double helix, stabilize the resulting single-stranded desoxyribonucleic acid (ssDNA) and promote the assembly, compared to the heating cycle driven PCR process. Ivan Lobato and Ciara O'Sullivan nicely reviewed the process as shown in figure 2.7.

First, the recombinase protein forms a complex with designed forward and reverse oligonucleotide primers. These primers are specific to a part of the target DNA. Recombinases are enzymes that catalyze the hybridization process of two ssDNA strands (or of a primer

and its complementary part of a ssDNA sequence). Additionally, the recombinase-primer complex is able to transiently open the double helix of the DNA to scan for homologue base-sequences that match the primer sequence. Upon finding a complementary sequence to the primer, it can be inserted to initiate the starting point for replication. This happens in forward and reverse direction simultaneously. Since the opened up DNA is likely to re-anneal under the given constant temperature conditions, SSBs help stabilizing the ssDNA strands. After this stabilization process, the DNA-polymerase starts to insert complementary desoxynucleotide triphosphate (dNTP)s to the ssDNA sequence the primer-recombinase complex is bound to. The elongation process with dNTPs can then start in forward and reverse direction.

Compared to PCR, the denaturation step is achieved without heating the sample. The process is replaced by using the recombinase enzyme that can open up the double helix of DNA. Furthermore, other then in PCR due to the temperature regulation, the stabilization at constant temperature conditions is achieved, again using additional proteins (SSB) that support the ssDNA stability.

Chapter 3

Advancements and Challenges of the Magnetic Reader System

This chapter deals with the state of readout and sensor technology for FMMD, initially introduced in 2007 by Hans-Joachim Krause [42] and adjusted by Stefan Achtsnicht in 2020 [94]. It discusses the considerations and characterization of an offset-scanner implemented in the handheld electronic readout unit and touches on important considerations for its mobile application. Section 3.1 briefly summarizes the FMMD instrumentation, including the sensory unit and the mobile electronic readout and suggests additional literature. In section 3.2, we will introduce the implementation of offset (B_0)-scanning technology in the context of mobile FMMD. We will characterize the interplay of applicable B_0-field and LF-field amplitudes, given the available power supply and power amplifiers in the mobile version of the readout unit, henceforth called the magnetic reader. In section 3.3, the stability of excitation signals will be discussed with respect to temperature induced excitation signal deviations. A concluding remark in section 3.4 will summarize the offset-scanner implementation. Possibilities and limitations of a mobile offset-scanner versus traditional offset-scans with a stationary setup in terms of available magnetic field strengths and potential influences on the signal readout will be pointed out. This section will also highlight the LF-amplitude scan in FMMD, introduced very recently [46] as a forward-thinking alternative to the offset-scan approach. This approach will be specifically looked at from the perspective of thermal drift correction and temperature effects on the FMMD signal readout in chapter 4 later on.

3.1 FMMD Instrumentation

Generally, the magnetic particle detection and signal acquisition with FMMD can be achieved using a two-component system. The first component is the sensor unit, which contains the excitation and induction-coils, hereafter referred to as the MH. The second component is the electronic readout unit that contains the circuitry for power supply, signal amplification, signal demodulation and filtering. This unit is the magnetic reader. Besides signal propagation and processing, it contains a Nextion Touch-Display (NX4827K043), a SD card storage, an ESP32 with Wi-Fi and bluetooth connectivity and a bar -or QR code reader.

3.1.1 Measurement Head

The sensor unit used in FMMD is a miniaturized induction coil setup, shielded by an eloxated aluminum housing. Three coil bodies are concentrically aligned within that housing, using thermoplastic polyether ether ketone (PEEK) coil holders. The outermost LF-coil is directly wrapped around a HF-coil, separated only by a small scotch tape stripe. With a small air gap to the HF-coil, the innermost PEEK structure will hold the differentially wound induction coil. This detection coil, captures the FMMD signal generated by the flipping action of dual-frequency excited superparamagnetic particles that will be placed in the hollow center of the cylindrical sensor geometry. The coils were wound using a copper wire with 0.18 mm diameter. The winding numbers are typically 2200 windings in the LF-coil, 500 windings in the HF-coil and 250 windings in each differential part of the detection coil. In figure 3.1 an exemplary schematic of the MH and a photograph of the housing can be seen. The exact geometrical dimensions of the MH housing and coil holders can be found in the technical drawings in appendix C.

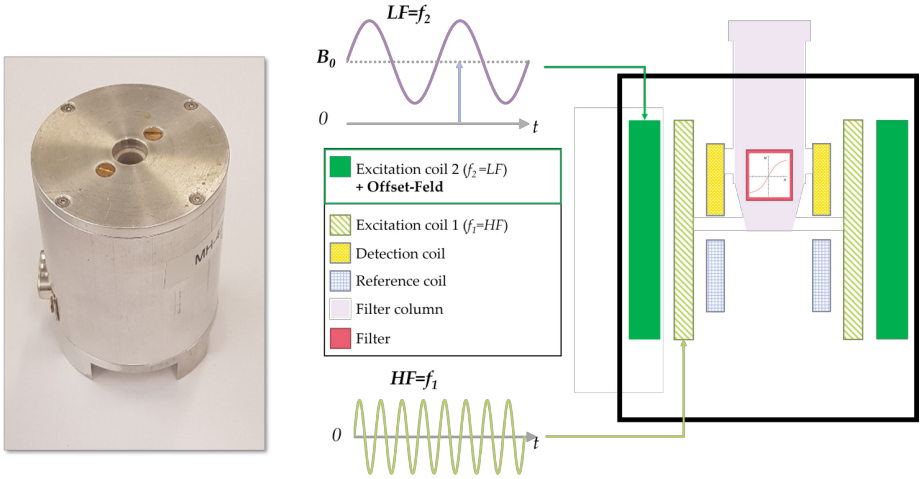

Figure 3.1: Photograph of the original measurement head (left) and schematic cross-section of the measurement head, including an illustration of the excitation signals after application of an additional offset magnetic field via LF-coil (right) [60].

Figure 3.1 also shows the principle of applying an additional offset-field by applying an additional DC through the LF coil component. This principle will be explained in 3.2 in more depth.

Besides connections to the lines of driver (LF) and probing (HF) field currents as well as a connection that forwards the induced particle signal to the preamplification circuitry of the magnetic reader, a ground (GND) connection and connections to the installed digital temperature sensor DS18B20 from Dallas semiconductors are established using a i/o Dsub-9 connector. This i/o plug is connected to its female counterpart on the magnetic reader, described in the section 3.1.2.

In this work two different MHs were used. Let us call them A1 and A3. Important electrical characteristics of the coils in these measurement heads can be found in table 3.1.

MH	Coil Type	Inductance	Resistance	Mutual Inductance
A1	LF	53.1 mH	96 Ω	$M(LF, HF) = 7.7\,\text{mH}$
A3	LF	–	75.8 Ω	–
A1	HF	1.6 mH	20.1 Ω	$M(LF, D) = 171\,\mu\text{H}$
A3	HF	–	37.5 Ω	–
A1	Detection	829 μH	17.2 Ω	$M(HF, D) = 131\,\mu\text{H}$
A3	Detection	–	17.3 Ω	–

Table 3.1: Coil parameters (resistance, inductance and mutual inductance) of different measurement heads used in experiments. The coil was characterized using a LC-meter HM8018 from HAMEG.

The mutual inductance was measured to test if for high temperatures, we observe a volumetric expansion. The measurement was performed by separately connecting the HF-coil to the LF-coil, the HF-coil to the detection coil and the LF-coil to the detection coil in series, respectively and measuring the total inductance of the serial connections. Following formula 3.1, the mutual inductance was calculated.

$$M = \frac{1}{2} \cdot (L_{serial} - L_1 - L_2) \tag{3.1}$$

where L_{serial} is the serial inductance of the two respective coils connected in series and L_1 and L_2 are the corresponding single inductances [95].

No changes in inductance were observed when heating up the measurement head. Therefore, the COMSOL simulations discussed in chapter 5 do not consider volume expansion.

3.1.2 Magnetic Reader

The PCB of the magnetic reader is shown in figure 3.2.

The core piece of the magnetic reader is a Arduino Due microcontroller, U5 ATSAM3X8EA-AU (marked in yellow) via which the DDS surface mounted device (SMD) chips (green) are set to desired frequencies. It also manages other key functions such as the power amplifiers (red) for excitation signal generation and signal preamplification circuitry (grey) and the frequency settings for the implemented tandem demodulation (bright blue). The DAC settings for application of a DC through the LF-coil (orange) that internally generates an offset-voltage for the application of an offset magnetic field in the MH (figure 3.1) is likewise controlled by the microcontroller.

Most of the concepts and functioning of these circuit components have already been comprehensively described in previous studies [94], [96]. Therefore, a full explanation of the setup will not be repeated here. Instead, this chapter focusses on device-internal offset-field application and introduces specific challenges related to the reliable application of the mobile version of the magnetic reader in crisis areas for PoC applications.

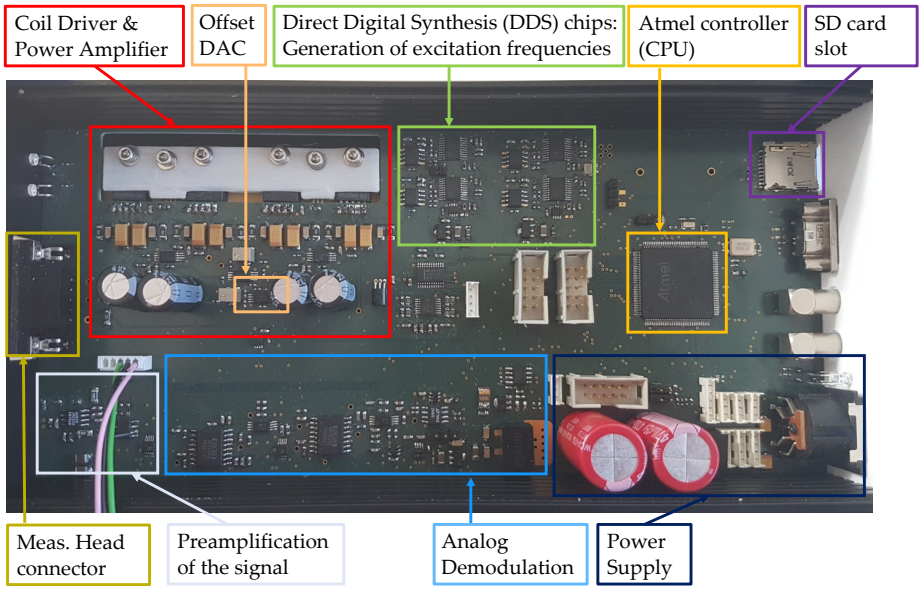

Figure 3.2: Readout electronics of the magnetic reader. The colored boxes highlight different essential parts of the signal processing and excitation field generation circuitry including the MH connector, signal preamplification, signal demodulation, filtering and more.

As a side project, a compact circuitry was put together to support mobile power supply, which is detailed in the supplementary material H.

3.2 Mobile Offset-Field Scanner Integrated Circuit and Magnetic Field Characterization

An extension of the FMMD principle followed thoroughly in recent years was the application of an additional offset-field (B_0), described in 2.3 superimposed to the HF and LF magnetic fields. The shapes of the offset-scans were reported to be characteristic for certain magnetic core sizes and materials of superparamagnetic nanoparticles [96], [78]. In order to perform an offset scan, one first needs to generate an offset-voltage which, until recently, was achieved by an additional external electromagnet (EM) with an active cooling module in a stationary laboratory setting [94], [96] or an additional pair of permanent ring-magnets [94], [58]. In the 2020 version of the magnetic reader, a major change was the integration of a circuitry for internal offset-field generation [60]. Here, the application of this circuitry in a practical context will be characterized. Figure 3.3 shows the corresponding integrated circuit (IC) via an analog devices AD5620 DAC for offset-application.

The first characterization measurement was carried out, measuring the voltage at R159 (transparent green) in the DAC offset circuit of the magnetic reader V2020 (3.3) with an oscilloscope tip connected to a digital oscilloscope to test the linearity of the offset-voltage generation and its voltage saturation.

After successful voltage linearity verification in the implemented offset-voltage generating

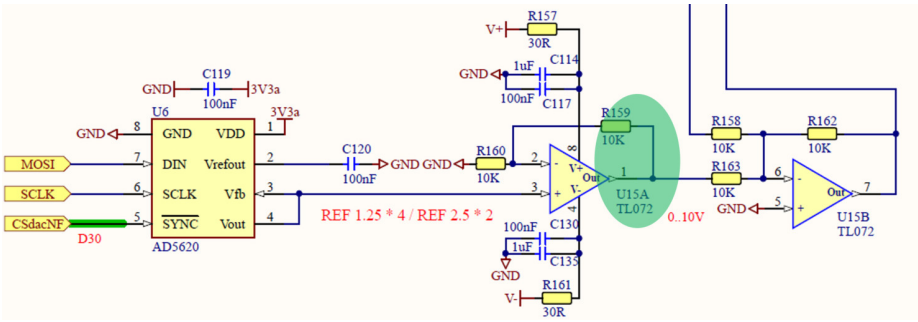

Figure 3.3: Integrated electronic circuitry for generation and amplification of an adjustable offset-voltage. The transparent green highlight shows the signal tap for measurement of the offset voltage linearity.

circuitry, the LF and B_0 magnetic field amplitudes were determined in terms of their linearity and stand-alone maximum magnetic field-strength (figure 3.4) with a secondary magnetic sensor (Hall sensor of type Allegro 1324) at the sample position of the measurement head. The Hall sensor was used to measure the offset magnetic field strength in the connected MH, generated through the DC voltage in the LF excitation coil. It was also used in combination with a lock-in amplifier to measure the LF excitation field amplitude, locked in at the frequency $f_2 = 62$Hz of the LF-signal. While the lock-in measurements were conducted analogously, the DC measurements were performed by connecting the magnetic reader and Hall sensor to a National Instruments DAQ,type USB-6251. The signal was tracked in a custom LabVIEW program for automatized and digitalized data extraction and storage [94].

The digital 12-bit potentiometer offers settings of amplitude between 0 to 4095 (which totals a resolution of 4096 values). In case of the B_0-field, 0 is defined as the minimum value, while 4095 is defined as the maximum value. The maximum offset field strength is already reached at values of approximately 2800, which is indicated by an abrupt flattening of the green curve in figure 3.4. The graph was recorded with a step-width of 200. In the case of the LF magnetic field (red curve in 3.4), the amplitude is controlled inversely, ranging from 4095 (minimum) to 0 (maximum). Therefore, high field strengths correspond to low step values.

With R^2 values of 0.99-1.0, clear linear relationships are observed for both the offset-field and the LF-field. To translate numeric amplitude setting values to field-strength, these fits will be used in the further data analysis.

An important aspect is the limitation imposed by the supply voltage (± 15 V) and the maximum coil current (≈ 250 mA). This maximally available power must be considered when simultaneously applying an LF-field signal and an offset-field to the LF coil. For example, the maximum achievable LF-field amplitude can no longer be applied once a certain offset field is reached. If the LF amplitude is further increased, the result is a distorted sine wave applied to the LF coil. Since a distorted driver signal in frequency-mixing magnetic detection leads to the generation of additional intermodulation frequencies, such distortion of the excitation must be strictly avoided. Therefore, a strategy for characterization of the interplay between LF-amplitude and offset-field was developed. This results in indication graphics, that give an orientation for the determination of the maximum applicable offset-field for each applied LF-field before a deformation of the LF driver field occurs.

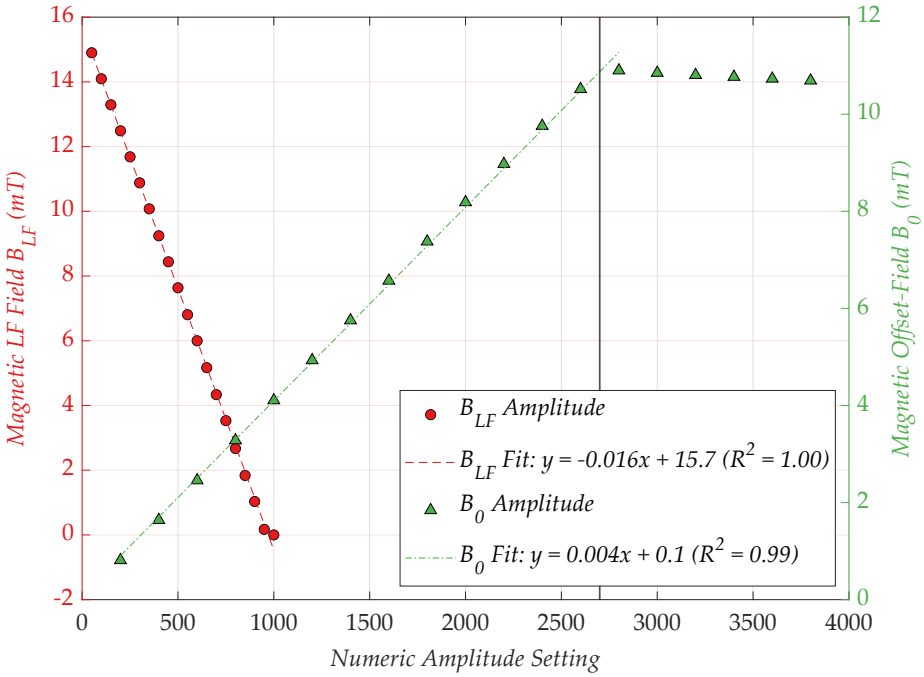

Figure 3.4: Achievable magnetic field strength extracted from Hall sensor measurements for the applied offset magnetic field B_0 (red) at different DAC settings and the LF magnetic field (blue).

This indication graphics was deduced from multiple complete offset-field scans. The magnetic field was measured with a Hall probe at the sample position, similar to the validation of magnetic field linearity shown in Figure 3.4. For each scan, a specific LF amplitude was selected. If the entire offset-field scan could be performed without distortion of the LF driver signal, the corresponding LF amplitude is applicable across the entire range of offset-fields. As discussed before, the smallest possible distortion will create unpredictable output in the FMMD-signal. The visual identification of sine wave deformations in the oscilloscope is therefore not sufficient. To unveil the magnetic field settings, at which deformation happens, first the offset-scans were recorded by changing the B_0 amplitude by about 0.8mT, equivalent to a change in numeric amplitude value of 200 each step (similar to the procedure in figure 3.4). This scan was repeated using different LF amplitude settings. The data were recorded using the National Instruments DAQ, each step (each setting) being recorded for ca. 30 seconds (or 10 data points, respectively) (figure 3.5).

At a certain point of each offset-scan, a clear saturation was observed. For some offset scan recordings in the lower LF magnetic-field amplitude region, this saturation occurs as the maximally allowed digital potentiometer setting is reached. Thus, these scans are not limited by the maximally allowed coil currents. For example, at the LF setting of 800 numeric amplitude value, and the maximum achievable B_0 setting of 2800, saturation sets in. In this case, still both magnetic fields (B_{LF} and B_0) can be used at its set amplitude and they add up to the sum of offset magnetic field and the positive peak amplitude of the LF field. At higher LF amplitude settings however (e.g. LF0 in the most severe case),

while still keeping the maximum B_0 setting of 2800, the saturation sets in significantly earlier then in the previously discussed case. Here, the limitation is given by the maximally allowed coil currents.

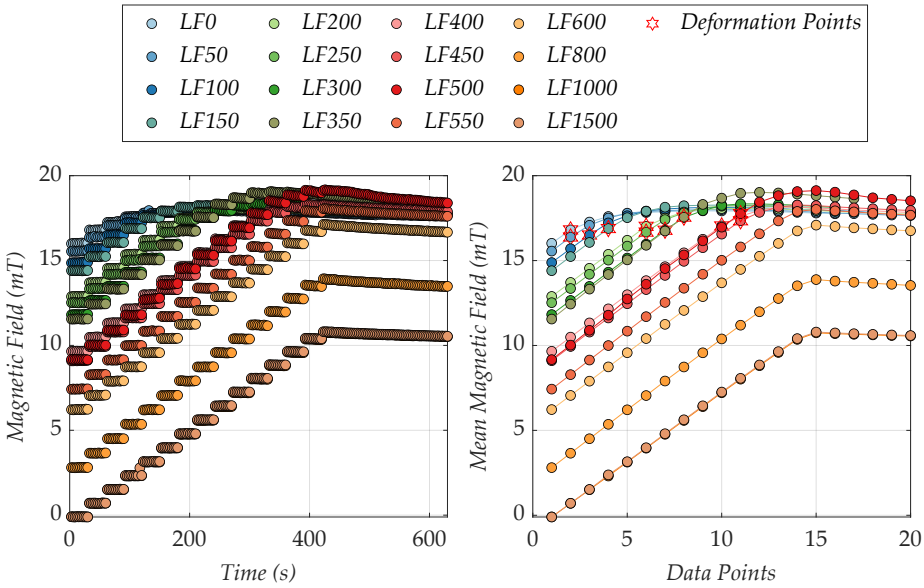

Figure 3.5: Hall sensor extracted magnetic field strengths, measured at the sample position of the MH. The recordings were performed at different LF amplitudes, across the entire range of B_0 amplitude settings. The legend indicates the numeric amplitude setting value for the LF component. The magnetic field strength of each B_0 setting was collected ten times. The magnetic field value at which the driver sine wave starts deforming is indicated by a red marker.

To identify the '*deformation points*', the difference of the means of each two consecutive steps was calculated and is depicted in figure 3.6 to find any deviation in step-height within the given 200 offset or 50 LF amplitude step resolution, respectively. The indices used on the horizontal axis are the number of averaged step distances from the original data collection. It becomes obvious, that besides a '*natural*' occurring signal drift (which will be discussed in 3.3), a sharp kink in the sets of mean differences for each LF setting arises. For the offset-scans, recorded with lower LF settings (1500,1000,800,600,550), the kinks indicate the previously mentioned maxima. However, the higher the LF-field amplitude setting (the lower the LF setting), the sooner the kink leaves 2.5×STD of the data with '*natural*' drift. This is due to reaching the maximum coil current already at lower offset magnetic fields, because of an increased LF driving field alternating current (AC). Crossing the $-2.5\times$STD mark (equivalent to approx. 1% tolerance level, assuming normally distributed data) was defined as the point of signal deformation and is indicated with a red circle.

With this definition, the index at which the mean difference signal starts redirecting strongly, depends on the resolution of the recording. However, it will give an orientation to what LF and B_0 magnetic-field strengths can maximally be achieved simultaneously with a good degree of confidence.

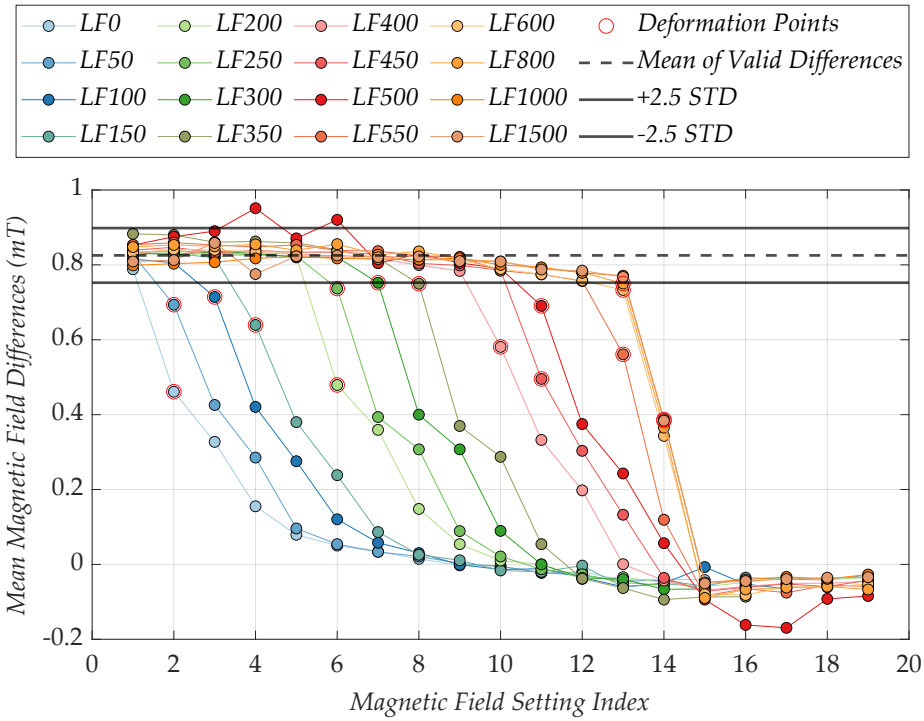

Figure 3.6: Mean difference magnetic field strength between each two consecutive 200 numeric amplitude value steps of Hall sensor extracted magnetic field recordings for different LF amplitudes. Mean (black dashed line) and $2.5\times STD$ *of the drifting data (black solid line) are indicated. The differences at which the applied LF signal tends to deform are indicated by red circles.*

For a more intuitive understanding, the identified '*deformation points*' were translated to the initial offset-scan collection. To not overcrowd the depiction, the collected data were averaged for each step in the set of offset scans at each LF setting in figure 3.5 B.

One can see at which measured magnetic field strengths the LF and B_0 settings resulted in a deformed sine wave. If the magnetic field strengths of these '*deformation points*' are now mapped against the LF amplitude at which the deformation occurred, the previously announced indication graphic can be created.

Figure 3.7 therefore shows which B_0 and LF magnetic field strengths are allowed (green) to be used simultaneously and which settings are forbidden (red) to prevent any excitation signal deformations. While this mapping shows a clear linear relationship, small deviations can already have drastic effects on the signal readout. The sharp transition between valid and forbidden region can therefore cause problems. To prevent accidentally selecting forbidden settings, an easy solution to make sure one can ever only select valid settings, despite small magnetic field fluctuations due to e.g. changing conditions in the surroundings, is introducing a buffer measure. The yellow marked area in figure 3.7 indicates this safety measure for any magnetic field fluctuations using $-3\times$STDs of the residue of the measured data to the linear regression line. This results in '*safe*' settings for the green region that

will not deform the driver sine wave, even when considering the signal drift. Nuances of this signal drift will be discussed in 3.3.

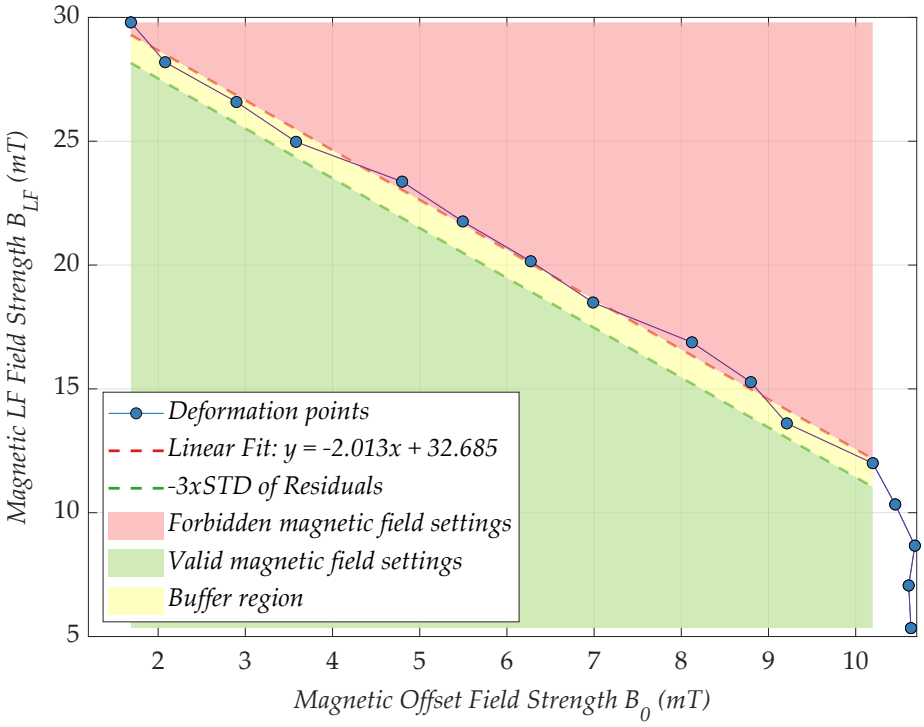

Figure 3.7: Graphic, indicating the maximally allowed (green) and forbidden (red) LF and B_0 magnetic field settings to prevent the LF driver signal from deforming. The yellow region indicates a buffer measure, between $-3\times STD$ of the residues between the measured points and the linear fit.

3.2.1 Internal Analog Offset Field Scan

Finally, the internally generated offset magnetic field was applied to SPM NPs and an automatized internal analog offset field scan was exemplarily recorded for synomag and perimag particles (figure 3.8) from Micromod Partikeltechnologie GmbH. These particles are commonly used in FMMD. When modified with a biocompatible matrix, they can be used for antibody or DNA modification. This allows for flexible usage in magnetic bioassays.

Similar graphs can be found in multiple peer-reviewed journal articles, where they constituted the basis for an approach to estimate a magnetic particle size, either depending on the position of zeros and extremes or later based on log-normal fits without considering the positions of zeros [78], [97]. Additionally, in an in silico study from Engelmann et al., the core-size dependent changes in offset-scan intensities [79] were investigated. However, in these contexts, the offset-scans were recorded using a stationary setup. This setup utilizes an additional external EM for offset-field application.

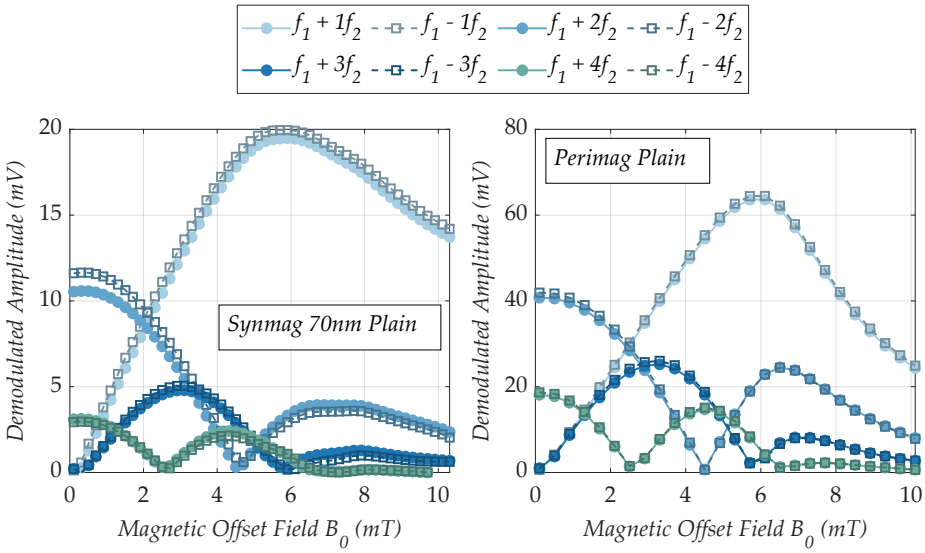

Figure 3.8: Offset-scan recorded with an offset magnetic field, generated through a DC in the LF coil in superposition to the LF magnetic field. This scan was recorded for Synomag 70nm (left) and Perimag (right) particles from Micromod Partikeltechnologie GmbH.

While generating up to 24 mT offset field strength by applying higher electrical currents, it required additional water cooling infrastructure, due to significantly higher rates of heat-generation. This hinders mobile usability. As compared to the laboratory setup, only half the offset-field magnitude can be applied in the mobile setting. The maximum applicable B_0-field in the internal offset-scanner is limited to ca. 11mT, even when applying a suitable (allowed) LF magnetic field that does not lead to deformation of the excitation signals. The maximum reachable LF amplitude, while maintaining the highest possible B_0 amplitude is also limited to ca. 12mT. The clear advantage, however, is its general mobile applicability.

3.3 Stability of Excitation Signals

The underlying type of distribution of the data population in the analysis of the change in mean differences (figure 3.5 B) is unknown. It can be estimated, however, using the so-called kernel density estimate (KDE) [98], [99]. In the present case, it provides an estimate of the relative likelihood to measure (observe) values of a certain magnitude between two different B_0 settings for a certain LF setting and can give additional insight into how the applied magnetic field strengths behaves throughout the measurement.

Often, even though a data distribution is not perfectly symmetrical, a very good first estimate is a Gaussian normal distribution [100]. The principle of KDE is, to use a kernel K (e.g. a function describing a normal distribution) of the form:

$$K(x) = \frac{1}{\sqrt{2\pi}} \exp\left(-\frac{x^2}{2}\right) \tag{3.2}$$

and overlay it to each measured data point.

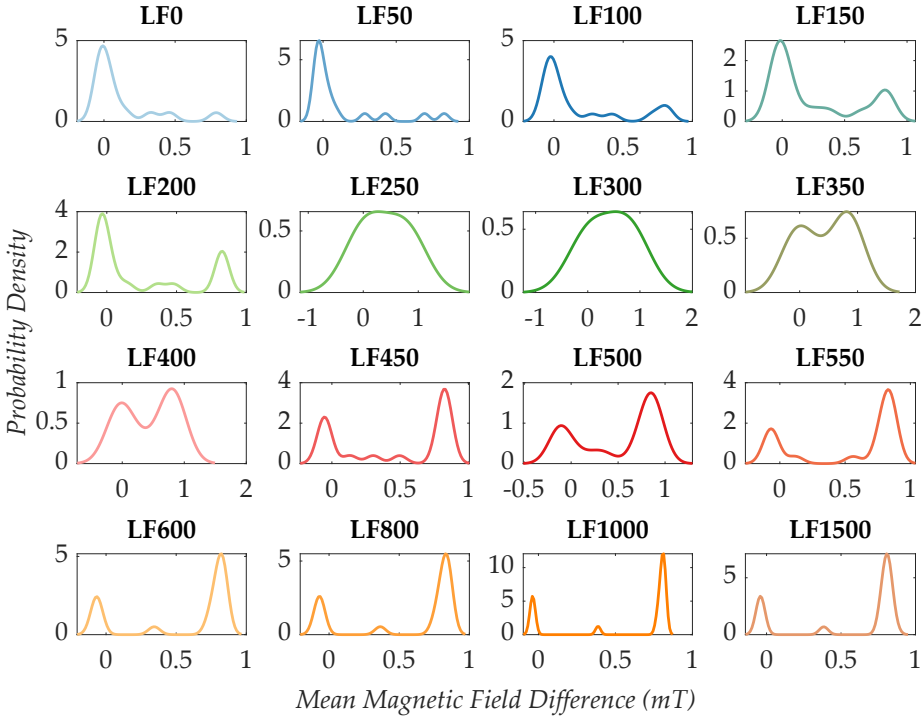

Figure 3.9: Kernel density estimate of mean differences for multiple recorded offset-scans at 16 different LF amplitudes.

The bandwidth h (in other words, the factor that determines the width of the estimated distributions) was estimated by *silverman's rule of thumb* [100]:

$$h = 0.9 \cdot \min\left(\hat{\sigma}, \frac{IQR}{1.34}\right) \cdot n^{-1/5} \tag{3.3}$$

Here, n is the number of data points, $\hat{\sigma}$ is the STD of a dataset, that is used to estimate the width of the selected kernel. Alternatively a fraction of the interquartile range (IQR) can be utilized for a similar purpose. It is scaled by $\frac{1}{1.34}$ to bring it to a similar scale as the STD. The bandwidth h is used rather than the STD σ because we do not know if the underlying distribution is actually normal.

Finally, knowing the bandwidth and the type of distribution and summing up all distributions around all measured data points of a single LF setting, will lead to an estimate for the probability density of certain "step heights" to occur (figure 3.9).

$$\hat{f}(x) = \frac{1}{nh} \sum_{i=1}^{n} K\left(\frac{x - x_i}{h}\right) \tag{3.4}$$

In formula 3.4, $\hat{f}(x)$ is the function that describes the complete density distribution estimation and K is the kernel for a normal distribution from equation 3.2.

The estimated probability density distributions in figure 3.9 of magnetic-field strengths differences for the settings LF1500-LF550 generally show two narrow peaks. The higher-valued peak represents the setting-separated magnetic-field differences up to the maximum possible magnetic-fields (maximum coil currents). The second and smaller peak reflects the portion of differences after the maximally possible fields are already reached. As the LF setting gets lower (the magnetic-field amplitude gets higher), the ratio of the large-to-small probability density peaks get smaller until its basically inverted. This is associated with the progressively earlier deformation of the driver sine wave. An interesting observation is that the shifting process does not seem to be clearly definite for the measured data, but rather continuous - already starting at settings where the driver sine wave does not deform. More specifically, the large peak already varies in width and height, before the excitation signal deforms (between LF1500-LF550). This suggest a LF and/or B_0 excitation signal change/drift. This drift was partially also identified from figure 3.5B in section 3.2 and can possibly be associated with changes in temperature in the coil environment. In fact, the maximum coil current might be so strongly dependent on temperature that (when using the highest possible field settings for LF and B_0) a very small thermal shift can already cause intermodulation frequencies to be induced, which may severely alter our frequency mixing signal. In the end of section 3.2, it was concluded that a simple buffer measure like $-3\times$STDs in the valid region of settings makes the determination of allowed amplitude settings '*safe*'. Because of this amplitude reduction by $-3\times$STDs however, the maximally possible magnetic-field amplitudes are not utilized, which can be crucial.

This holds especially true e.g., for smaller SPM NPs with a high magnetization saturation. Additionally, the scanning mode of the magnetic reader plays an important role, as it introduces either additional heat or less heat. Not indicating a buffer measure however, slight temperature changes can already fraud the FMMD signal by altering the excitation signal shape.

Another indication of a temperature dependency is that the drift of total magnetic field amplitude in figure 3.5 becomes more severe for offset scans, after reaching higher maximum achievable magnetic fields (maximum coil currents). The fact that the highest achievable magnetic field strength changes is already an indication for a change in temperature. Additionally, the offset-scans that reached higher maximum magnetic field strengths (e.g. at settings of LF350 and LF500) were the ones that experienced the lowest temperature during their data acquisition (see appendix I) compared to other data samples. Lower temperatures lead to lower resistances, which generally allow for higher electrical currents. This consequently increased the saturation values initially.

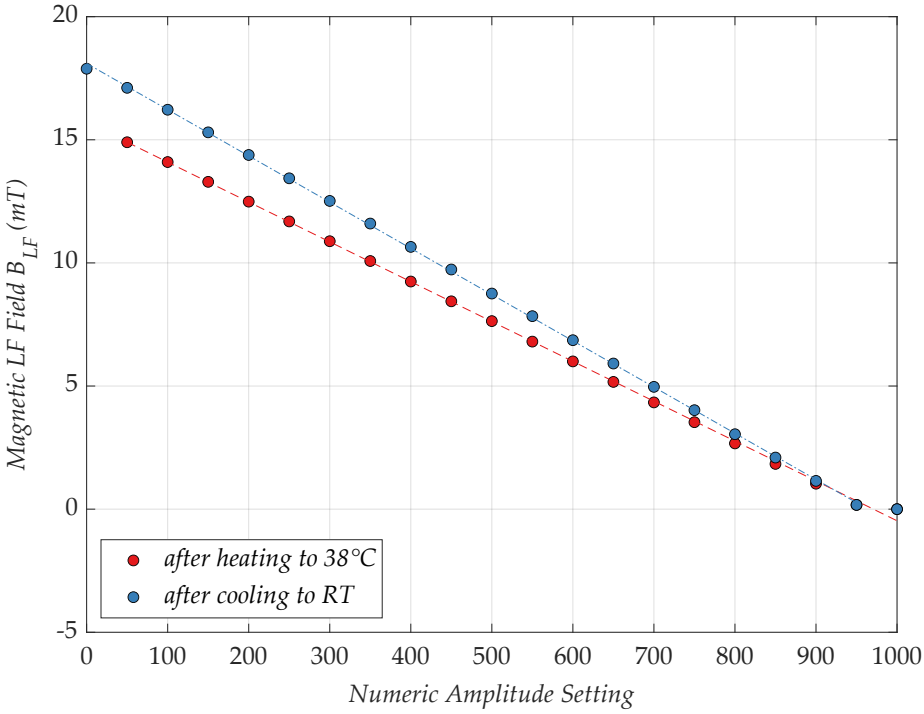

Figure 3.10: The graphic depicts the LF magnetic field strength for different digital potentiometer settings, starting from two different initial temperatures.

The magnetic reader is voltage-regulated, it delivers a defined voltage but does not provide a direct regulation of electrical currents. Consequently, the higher the load resistance, the lower the electrical currents. Since the highest load resistance in the present setup is the LF coil, its heat dissipation was hypothesized to be the major contributor for a change in MH temperature. In order to specifically measure, that there is a temperature-dependence of the LF magnetic field amplitude, its magnitude was tracked for different settings.

Initially, the measurement was started with a coil temperature of approximately 294 K. The same measurement was repeated, starting at 314 K, see figure 3.10. This proved, that there is a change in LF excitation amplitude that declined as the temperature equilibrated.

From temperature-independent inductances and mutual inductances, it was concluded that the volume expansion was negligible. However, the resistances of LF,HF and detection coils changed by about 8 to 10% in a temperature range of ca. 20 K (figure 3.11), which in turn results in changes for e.g. the applied LF excitation field by a similar amount (see figure 3.12).

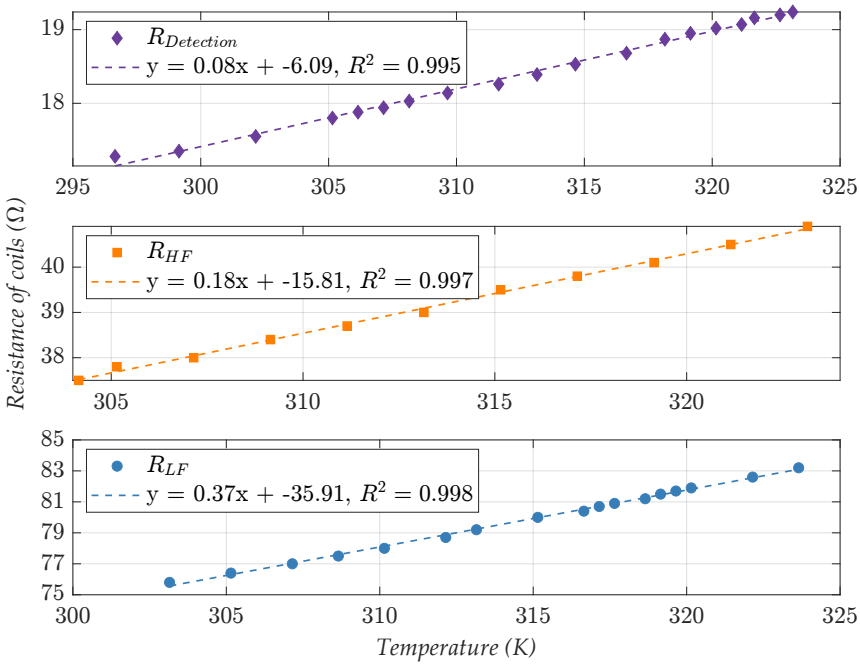

Figure 3.11: The plot shows the dependence of LF,HF and detection coil resistance on temperature.

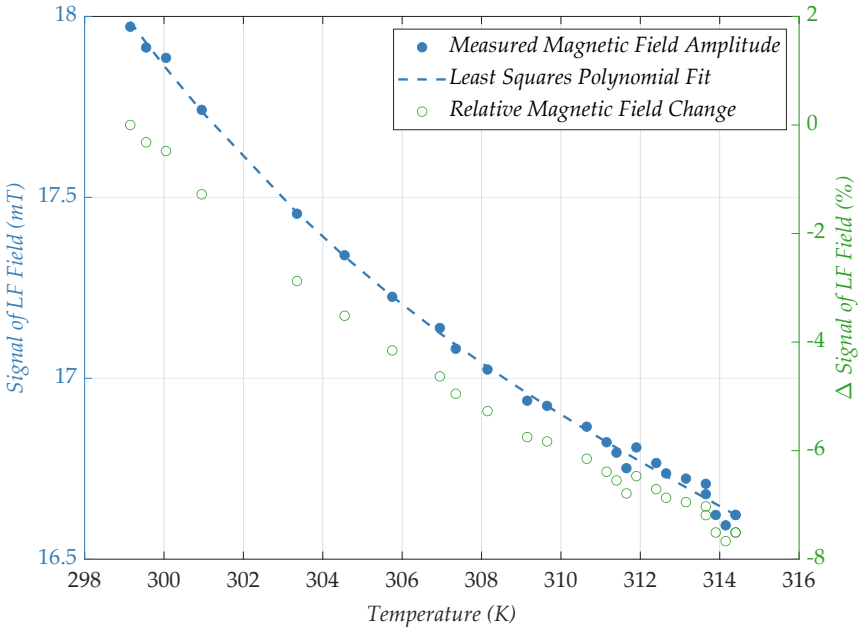

Figure 3.12: Change of absolute and relative LF-magnetic field strength in mT *with temperature.*

While the HF and detection coils are also affected by the changes in temperature, the major contributor to resistive heat generation is the LF coil component. This resistive heating is sufficient reason to investigate a possible countermeasure. Chapter 5 will suggest strategies to improve the stability of the LF coil resistance. Automatically, this will lead to an improvement in temperature stability of the entire induction coil sensor.

3.4 Concluding Discussion and Outlook

The magnetic reader internal offset magnetic field generation was characterized in terms of its maximum applicable field, while still applying LF-amplitudes suitable for FMMD measurements. It was shown that, although limited by the magnetic field scanning range, internal offset-scans can be automatically recorded. Depending on the application and used magnetic particle type, this implementation, together with the determination of allowed settings, enables mobile offset-scans.

The scanning range, however, is a crucial factor that limits the size of magnetic particles that can be used in assay applications, as the nonlinear part of their magnetization curve needs to be reached by the applicable driver-field amplitude.

Furthermore, it was found that besides the electrical current-limitation, thermal effects play a critical role when selecting settings for offset-scans as well as in general terms of excitation signal stability. While the resistive heat in case of the magnetic reader internally generated magnetic offset field is not as strong as from the external EM in the stationary setup [96], [94], [101], [37], [41] the strategies for cooling the device in a mobile setting are harshly limited, whereas the stationary setup is water-cooled. The wire resistances of the coils in the MH were shown to change by about 10% in a 20K temperature range. Besides the effects of a temperature-induced change in LF amplitude, the B_0 amplitude, plotted on the x-axis of the offset-scans, can lead to an unintended position change of zeros and extremes compared to the stationary measurements when not using a temperature-corrected offset magnetic field reference. In a practical context, this is especially challenging when the conditions in which the magnetic reader is operated are constantly changing.

The temperature of the coils in the MH is not solely determined by the LF-currents, although the LF coil is the biggest contributor to heat development. The rate of temperature change in the MH, depends specifically on the difference between ambient temperature and MH temperature, which may make the regulation of thermal influences in a mobile setting more challenging, as a stable laboratory condition can not be assumed.

In 2022 Timur Bikulov introduced a scanning principle [46] for FMMD that is closely related to strategies applied in AC suceptometry (ACS). The principle is relying on a change in LF amplitude rather than an additional offset-field for scanning the particle sample. This approach does not suffer from the limitation of maximum field-magnitude in mobile deployment in the same way. Eliminating the need for a static offset-field also simplifies the determination of influential factors, like resistance changes.

In this context, this work will investigate strategies of keeping the resistance changes minimal and therefore attempting to optimize FMMD reliability in terms of temperature sensitivity. This will be discussed in chapter 5.

Chapter 4

Temperature Dependency of the FMMD Signal

Besides the thermally induced changes in driver amplitude and settings, discussed in chapter 3, changes during FMMD signal acquisition of magnetic immunoassays, which were recorded under different temperature-controlled environmental conditions, were observed. Additionally, indications of signal change associated with the sample temperature were observed. Therefore, using a laboratory grade setup, the amplitude of the harmonic signal $f_1 \pm 2 \cdot f_2$ will be exemplarily investigated over longer time periods. In trial to prevent possible changes caused by thermal drift, a 2-point temperature regulation will be implemented. Both, the LF coil surface temperature and changes in the environmental temperature were tracked. It will be discussed whether the signal drift is constant and reproducible in both cases.

4.1 Magnetic Immunoassay Application Readout

As laid out in the introduction 1, the final target is to quantify pathogenic compounds sensitively, fast and reliably using the FMMD device for drinking water analysis, dairy industry or at animal farms. For some of these applications, it is necessary to detect very low concentrations of the respective bacteria due to strict regulations for the number of colony forming units (CFU) that are considered critical. Furthermore it is desirable to differentiate between different pathogenic components in a single measurement, using multiple types of magnetic beads and separating their magnetic signals. Therefore, it is especially important to keep the variation in the signal low and to reduce error sources in the measurement.

Signal variations in MIAs were tested by measuring the FMMD harmonic component $f_1 \pm 2 \cdot f_2$ for different *enterococcus faecium* analyte concentrations in a sandwich type immunoassay.

4.1.1 Immunofiltration Column Preparation

For the detection of *enterococcus faecium*, ABICAP immunofiltration column (IFC)s [102], purchased from Senova GmbH (Weimar, Germany) were prepared in collaboration with the Fraunhofer IME in Aachen, equivalently to the procedure described in [61] and for different applications in [103], [104], [105], [62]. In short, IFCs with a pore size of 20-50 µm in diameter were first treated in an ethanol bath in a desiccator for ca. 20-30 minutes for degassing purposes. A thorough rinsing with 50% ethanol and 50% water followed by deionized water and an immobilization buffer for primary antibody coating was performed. The IFCs were afterwards stored in carbonate buffer.

4.1.2 Sandwich Immunoassay Preparation

The following assay preparation steps for the Anti-*enterococcus* sandwich MIA were performed at room temperature (20-25°C) following an internal SOP [106]. The filter was pre-coated with antibodies, specific to the *enterococcus* bacteria as described in 4.1.1. The analyte solution was applied to the filter column and incubated for ca. 15 minutes. After washing, the biotinylated secondary antibodies were then applied to the IFC and incubated for 10 minutes. After another washing step, the magnetic particle solution was applied. In this step, the secondary antibodies were modified with magnetic nanoparticles. Here, Nanomag®-CLD/synomag®-CLD hybrid particles with 700 nm hydrodynamic diameter in a dextran matrix were used. The steptavidinated surface enabled binding to the biotinylation of the secondary antibodies. Last, a final washing step was performed.

4.1.3 Temperature Dependence of Anti-Enterococcus Assay

The measurements of *enterococcus faecium* were carried out in regulated constant ambient conditions in specialized thermally regulated incubation chambers (typically used for cell-culture purposes) at 4, 15, 21, 28 and 37°C. A dilution series was prepared and each assay was performed twice for the analyte concentrations $250 \cdot 10^6$, $15.6 \cdot 10^6$, $977 \cdot 10^3$, $61.03 \cdot 10^3$, $3.81 \cdot 10^3$ CFU/ml, respectively. Since, at the time of these experiments no temperature controller was installed, the measurement device was always pre-heated in the respective surrounding conditions for 70 minutes. The excitation amplitudes were turned on to reach a thermal saturation and prevent signal variation caused by resistance and setting changes (discussed in chapter 3). After inserting a sample filter column, a temperature adaptation time of 10 minutes was kept. The influence of sample heating on the FMMD signal in particular will be discussed in section 4.2.

The dependence of the average measured signal on temperature, as shown in Figure 4.1 is modelled using the linear regression given by $\hat{y}_i = ax_i + b$. The residuals are the differences of the measured signal y_i and trend line value $\hat{y}_i$, namely $r_i = y_i - \hat{y}_i$. The standard deviation of the residuals therefore is:

$$\sigma_r = \sqrt{\frac{1}{n-1}\sum_{i=1}^{n} r_i^2} \tag{4.1}$$

Relating the STD of residuals to the mean of the measured data RSD $= \frac{\sigma_r}{\bar{y}} \times 100\%$, where $\bar{y}$ is the mean, puts the fluctuations in context of the overall signal magnitude.

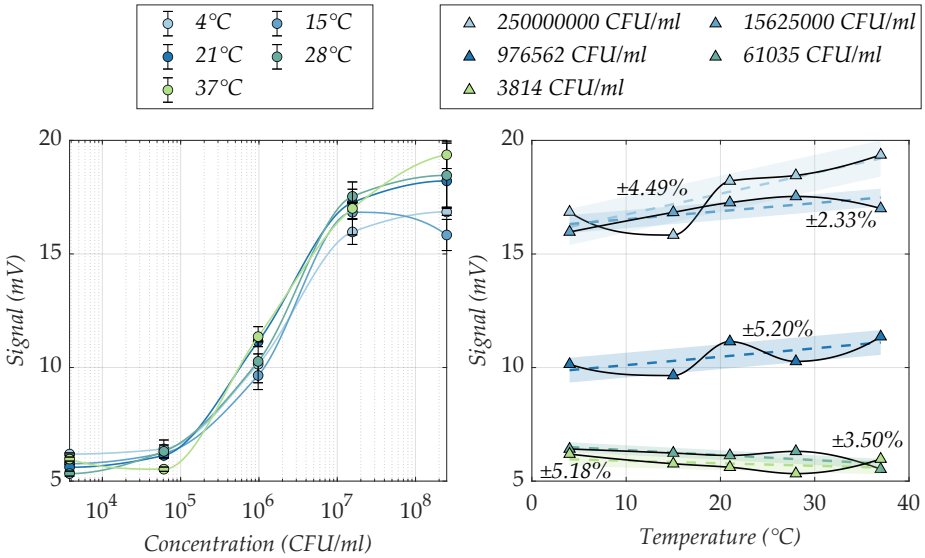

Figure 4.1: FMMD $f_1 + 2 \cdot f_2$ signal component amplitude measured for sequentially diluted enterococcus faecium in MIA (left). Change of measured signal amplitude with temperature for different constant ambient conditions (right). The shaded areas indicate the average error relative to the total measured signal amplitude based on linear regression.

First and foremost, one notices that the signal variations are not associated with a clear direction. Lower signal amplitudes decrease with temperature, while larger signals increase with temperature. Qualitatively, if the measured signal is closer to the background signal, the trend seems to be more negative, while the trend becomes more positive as the signal amplitude rises. This may indicate, that the background drifts differently for altering temperature conditions, compared to the signal generated by higher amounts of magnetic nanoparticles. The accuracy of each measurement is associated with the fluctuations of the measured values around the average amplitude in different measurement conditions. However, with ca. 2-5% signal variance around the linear regression, even at constant ambient conditions, we observe variations in the fluctuation. It is not only important how large the relative variance is, it is also crucial that a reliable and constant measure of accuracy can be provided.

4.2 Temperature Dependency of the Magnetic Sample

Aim of the next section is to analyze a temperature regulated example measurement in terms of sample heating influence on the signal. Special attention has been paid to the setup used to execute the measurements, regulate the LF coil temperature and remove potential signal line couplings from the prototype magnetic reader.

4.2.1 Laboratory Grade FMMD Setup

The quartz crystal and DDS chips from the PCB of the mobile magnetic reader were used to generate excitation signals of the high (HF) and low frequency (LF) components. The LF excitation component was calculated as $f_2 = \frac{2 \cdot 338 \cdot 50000000}{2^{28}}$, where 50 MHz is the stable clock frequency stemming from the crystal oscillator of the magnetic reader and 338 is the DDS setting needed in the present configuration to achieve the low frequency component f_2 at circa 62 Hz. Similarily f_1 was calculated to be 40554 Hz. The filtering, signal demodulation and data acquisition units of the magnetic reader were replaced with laboratory grade equipment. Also, python scripts were adopted for the communication with power amplifiers. The 2-point temperature regulation was also implemented in the respective program, with the logic represented in section 6.1.

In this setup the first demodulation step at f_1 was done analoguesly using a lock-in amplifier and the second demodulation step was performed digitally in the software at $2 \cdot f_2$.

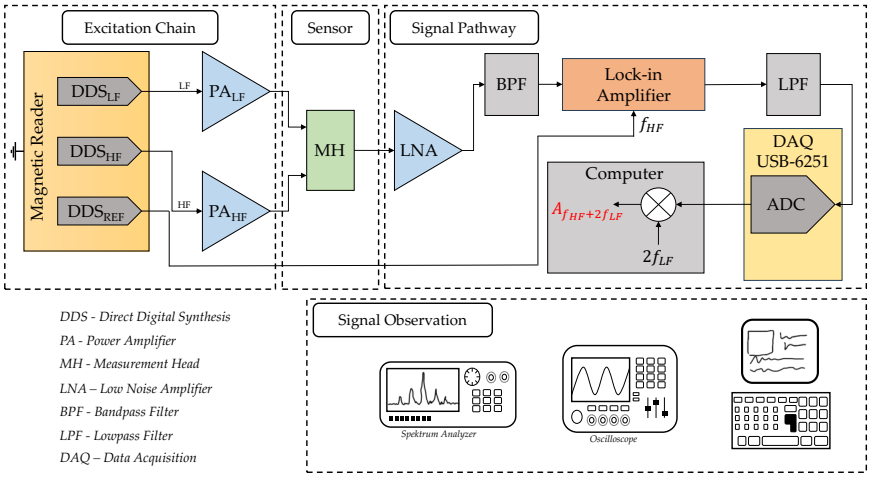

Figure 4.2: Block diagram of laboratory setup in three sections.1) Excitation Chain with DDS chips from magnetic reader and subsequent LF and HF power amplification, 2) MH sensor and 3) the signal pathway including signal filtering and combined analogue (lock-in amplifieder) and digital demodulation (in a PC) process. Blue triangles depict different amplifier types, grey rectangles depict signal filters, yellow colors indicate signal generation or readout components. Red text indicates the demodulated amplitude signal, depicted in figure 4.3.

The acquired MH sensor induction signal was low noise amplified with a 20 dB gain. The gain factor has an influence on how much the device noise contributes, so it can actually influence if we see signal in the spectrum analyzer or not. This was also the reason a potentiometer was used for tuning the fundamental frequency f_1. The signal subsequently was bandpass filtered between 39-41 kHz using a band pass filter (BPF) SR650 from Stanford® Research. This frequency band was observed in the spectrum analyzer and contains all harmonics in the given frequency range. Afterwards the signal was low pass

filtered and amplified again using the low noise amplifier (LNA) with integrated low pass filter (LPF) SR560 from Stanford® Research. A sampling rate of 1000000 samples per second for the ≈ 50 kHz signal was used. The Lock-In amplifier (SR830 DSP from Stanford® Research) was used for the first analogue demodulation step at f_1, provided by one of the reference DDS chips in the magnetic reader. The signal was fed to the USB-6251 DAQ from National Instruments. Since the USB-6251 DAQ is limited to an input of ± 1 V, a voltage divider was installed in front of the measuring card input.

With python scripts, it is possible to record the data fed to the National Instruments DAQ (USB-6251), drive the spectrum analyzer and control temperature regulation of the MH. With that it is possible to regulate the temperature to different levels and measuring particles at diverse but constantly regulated offset temperatures. Except for drastic ambient influences, this duty-cycle control enables us to exclude environmental temperature influence to a large extend and only observe sample behaviors and its effects on the detection signal (e.g. putting samples from different initial temperatures).

(To prevent phase differences between excitation/reference signals, when changing a DDS frequency, one should reset the DDS chips after every frequency change to synchronize the phases of respective parts.)

The second demodulation step was performed digitally, according to:

$$A = \sqrt{\left(\frac{1}{N}\sum_{i=1}^{N} x_i \cdot \sin(2\pi(2f_2)t_i)\right)^2 + \left(\frac{1}{N}\sum_{i=1}^{N} x_i \cdot \cos(2\pi(2f_2)t_i)\right)^2} \tag{4.2}$$

where x_i is the sampled signal sample at time t_i. N is the total number of samples. The demodulation frequency f is programmed to be $2 \cdot f_2$. The signal was windowed with a Hanning window before digital demodulation.

An important finding while setting up the laboratory equipment and sensor was, that the DS18B20 temperature sensor had been inexpertly located near the light barrier for sample insertion detection in some MH sensors. The light barrier requires a pull-down resistor. The Joule heating from this resistor altered the temperature measurement that was taken as a coil temperature reference in some previous works. Therefore, the sensor was relocated and affixed on the coil surface with thermal paste and cable ties. All measurements in this work were then conducted using this updated assembly.

4.2.2 The Heat Gun Experiment

Using a 2-point controller we can significantly reduce the heat up time by selecting a lower regulation temperature than the equilibrium temperature the MH sensor would eventually reach in continuous operation. However, by using a PWM approach, we will decrease the *on*-time of the excitation amplitudes, when ever the MH gets too hot and needs to cool passively. Therefore, this approach will be specifically used for the analysis of temperature influence on the signals and for biological applications at regulated temperatures (also see chapter 6). Finding a more suited solution to reduce heat up time and simultaneously increase excitation amplitude *on*-time will be discussed in chapter 5. A possible portable active cooling feature will be suggested in the outlook 6.6.

In the following experiments, a heat gun was used to influence the ambient temperature around the MH and observe the effects on the implemented controller and harmonic acquisition.

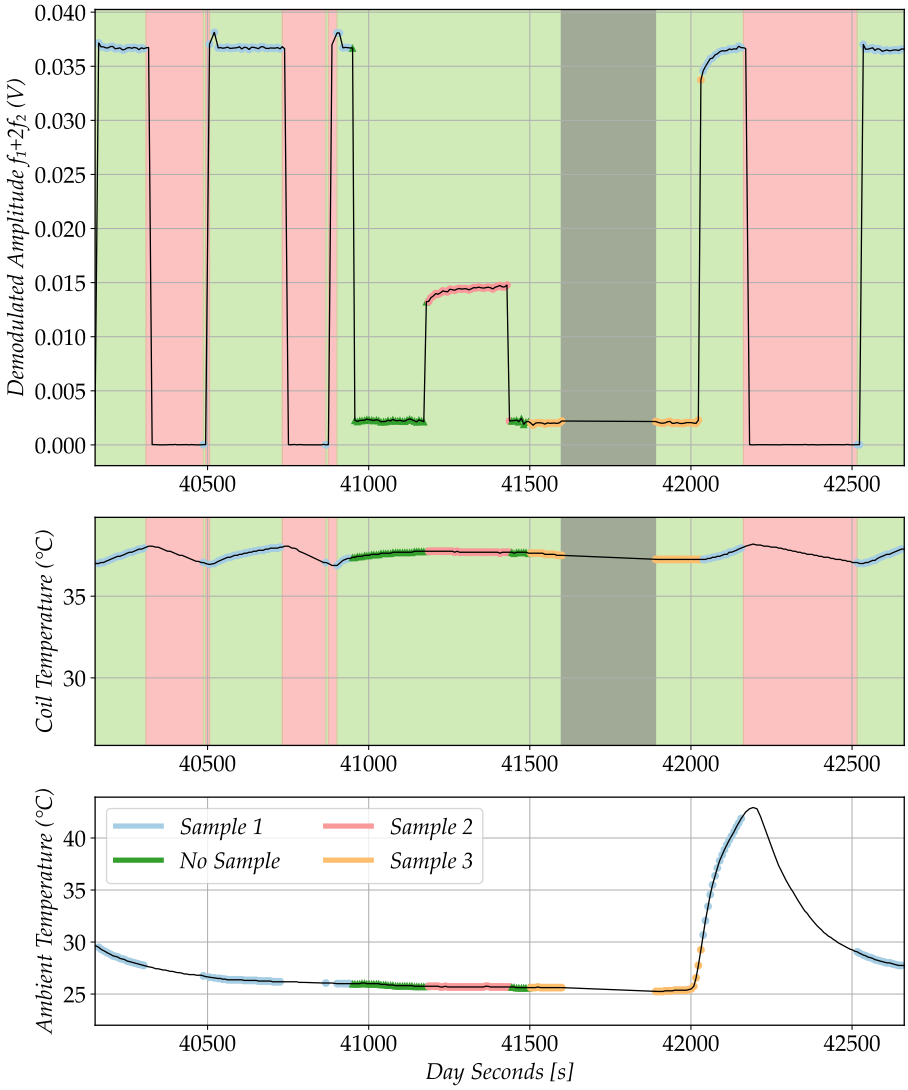

Figure 4.3: The upper subplot depicts the demodulated signal amplitude at $f_1 + 2 \cdot f_2$, the middle subplot depicts the measured temperature on the coil surface and the lower subplot depicts the ambient temperature away from the MH. Red and green background colors indicate on and off states of the excitation amplitudes, respectively. The grey background color indicates unrecorded intervals. The color markings on the plotted line indicate different samples (blue, red, yellow circles) or no sample (green triangles).

The red areas in Figure 4.3 indicate that the excitation amplitudes were switched off during

that period for regulatory purposes. The green regions, are regions of active measurement, where the LF and HF excitation amplitudes are turned on. A continous signal with low amplitude variance can be achieved, when the sample is not taken out of the MH sensor for a while (sample heat up allowed). In case of continous thermal regulation with inserted sample, the constant sample tempertaure leads to mostly stable signals with very low variance, most probably caused by thermal regulation. However, when inserting a sample, the experienced signal drift clearly depends on the sample's initial temperature and the type and or concentration of magnetic nanoparticles used. For the (blue) high concentration sample, the MH is brought out of thermal balance, everytime the sample is inserted although the demodulated amplitude stays relatively constant. This is not the case for all other investigated samples. To quantify the signal change, the relative signal change before and after drift up to visual saturation was calculated. The *No Sample* measurement (green triangles) was used as a background signal, to be subtracted from the signal amplitudes before and after drift. The *Sample 2* (red circles) signal saturates after around 12.24% amplitude drift. For *Sample 1*, a 8.9% drift was calculated. *Sample 3* (yellow circles) has a very low particle concentration, and a signal cannot be differentiated from the background. Interestingly, the recorded signals for *Sample 3* also do not alter upon sample insertion.

From 40800 to 42000 day seconds, the samples come from originally lower ambient temperatures (RT), than what the MH is regulated to. This seems to counteract the change in MH temperature and keeps it inside the measuring range. In general, the variation in sample temperature may be strongly dominated by the heat capacity of the sample holder rather than the magnetic nanoparticles themselves. It remains unclear to which exact extent temperature-related changes of the particles' magnetization contribute to the observed changes in FMMD signal. In MPS systems, it was simulated and measured that temperatures between $-20\,^{\circ}\mathrm{C}$ and $75\,^{\circ}\mathrm{C}$ already have noticable influence on the shape of the magnetization curve and therefore on the spectral magnitude of measured harmonic components [48]. It was also shown, that the influence of temperature becomes more pronounced, the higher the order of the harmonics measured. This holds especially true for freezed dried samples with supressed brownian relaxation [48]. Furthermore, James Wells and coauthors have shown, that different particle types actually obey different behavior at diverse tempertaures, by comparing harmonic amplitude ratios and phases of MPS and MPI signals [47]. Depending on the type of magnetic nanoparticle used, the harmonic amplitudes indicated anything between 2% up to 20% signal variation in a temperature span of 20 K [47]. Another study from Draack and collegues investigated temperature and viscosity dependence of MPS signals and established a clear connection between the harmonic signal amplitude and viscosity of the surrounding medium in brownian relaxation dominated samples [49]. It was proven, that this behavior translates into derivative techniques like MPI [49].

In assay applications of the FMMD technology we use filter matrices for the biological components to be captured (see section 4.1.1). In these immunofiltration columns, we neither have completely dried samples, nor liquid suspensions. It is likely, that the different relaxation contributions vary with liquid content, that naturally changes due to evaporation, especially in higher tempertaure. While the mentioned studies may not be directly translatable to the temperature influence on the FMMD technology, it is evident, that the sample temperature needs to be regulated or kept constant to provide accurate measurements upon sample insertion. Especially in PoC settings, where we do not want an increase in measurement duration due to waiting times for device and sample heat-up.

The rise of ambient temperature at around 42000 dayseconds was caused by a heat gun. Due to this temperature increase in combination with preliminary cooling of Sample 1, the downward regulation is prolonged and thus the *off*-time of the excitation amplitudes increased. Therefore, the efficiency of the controller algorithm is impaired. The ambient conditions also seems to influence the rate of signal change.

It is furthermore observable that for any decreasing ambient temperature interval in the measurement (Figure 4.3), the signal also decreases, even when the LF coil temperature is rising, although the magnitude of change is very little here since we work in a controlled environment. Since the MH system is not completely closed, there may be a contradictive relation of the FMMD signal with the ambient temperature and with the LF coil temperature, which leads to difficulties interpreting the results.

4.3 Conclusions

We have seen that the FMMD signal amplitude alters upon acquisition at different constant ambient conditions in section 4.1.3. We also exemplarily studied changes in the signal for a thermally regulated sensor unit. As described in section 4.2, the surroundings of the measurement head sensor were artificially heated, and the influence of temperature changes on the PWM controller as well as on the $f_1 + 2 \cdot f_2$ signal component were investigated. The time constant τ of the signal is sensitive to the initial sample temperature. In the assay application, no clear indication of linearity was observed, which may make the use of predictive algorithms more complicated. Different drift duration and a signal drift differences between 8.9% and 12.2% of the total signal amplitude were observed in the temperature regulated magnetic particle measurements. Meanwhile, signal variations of up to 5% in the bioassays at constant ambient temperatures were calculated. The seperation of the signal alterations that originate from a change in magnetization of the particles, variations in the assay temperature or thermal mass of the sampleholder are therefore not straight forward. Nevertheless, the magnitude of the observed changes highlights the need to develop more general methods (e.g., the numerical approach in chapter 5) to better understand the thermal behavior at different situations.

The measurement schemes presented in chapter 5 do not regulate the temperature to a specific value. Instead, they keep temperature fluctuations in both the measuring head and the sample as low as possible. This leads to more stable signal recording. This assumption is also supported in this chapter by the measured data shown in Figure 4.3. Specifically, from 40000s - 41000s, it can be observed that a constant measurement signal can be achieved for a constant sample temperature. Thus, achieving a constant temperature for magnetic particle samples is more important than achieving a specific target temperature. In the case of assay applications, for example, reaction kinetics, binding behavior, and, at higher temperatures, the evaporation of liquid in the filter column could have an additional influence on the signal behavior.

Reaching necessary sensitivity limits for bacterial concentration detection of single digit CFU to fulfill drinking water testing requirements is impossible at the current stage of development. In comparison to the Tecta® system from IDEXX [11], there is a trade off between sensitivity and response time, that needs to be considered. According to the THW, in many situations the advantages of rapid on-site testing outweigh the drawbacks of more time-consuming laboratory procedures with higher sensitivities. For example, quick

initial testing of e.g. *legionella* contaminations in the pipes of accommodations in crisis areas would already be a significant improvement. In other words, the FMMD technology provides the advantages of mobility, ease of use, very high selectivity and faster response time, whereas the gold standard Tecta® system provides maximum sensitivity. For FMMD, an increase in sensitivity can maybe be reached by additional procedures like the magnetic separation and sample preconcentration to improve sensitivity of subsequent measurement. In this approach, an increase in sensitivity by a factor 10^3 is expected.

The FMMD signal behavior suggests that both rate of temperature change and particle sample influence the readout in ways that are difficult to predict. This is also supported by earlier findings of the magnetic sensors group in appendix E.

Chapter 5

Low Frequency Coil System Modelling and Minimization of Resistance Fluctuations

In chapter 3 we have seen that the wire resistances of LF, HF excitation and detection coil change with temperature. A change in temperature in the immediate induction coil environment is inherently generated upon application of the LF excitation currents by means of the generated resistive heat. This also influences the amplitude settings, that carefully need to be selected in the offset scanning approach, to ensure that the LF driver signal does not deform. When settings are too high, the excitation signal is deformed, which leads to intermodulation frequencies in the FMMD signal readout. In chapter 4 we looked at the influence of additional thermal effects on the harmonic signal readout of FMMD. This readout may be influenced by the change in detection coil resistance, but also by a change of the sample temperature upon insertion into a heated MH sensor. Additional influences in field-applications may be constituted by environmental temperature changes and therefore varying convective cooling. We have also seen a substantial error in the readout of an immuno-assay signal in incubation rooms at different temperatures.

Determining an exact analytical function that the temperature-dependent FMMD signal follows for magnetic immuno- or DNA-assays, thus remains challenging (also see Appendix E, estimation of time constants). Given the nested dependencies in the system shown in the function description 5.1,

$$S_{FMMD} = S(\{R_i(T_i)\}_{i=1}^{3},\, \nu(T_s(T_{\text{amb}}, P_{LF})),\, M(T_s(T_{\text{amb}}, P_{LF}))) \tag{5.1}$$

a complete mathematical or even phenomenological separation of thermal effects on the FMMD signal may not be as not straightforward as initially expected. The LF-, HF- and detection coil resistances $\{R_i(T_i)\}_{i=1}^{3}$, the reaction kinetics of a biological sample $\nu(T_s(T_{\text{amb}}, P_{LF}))$ and the magnetization curve $M(T_s(T_{\text{amb}}, P_{LF}))$ of the SPM particles all depend on the sample temperature, which in turn depends on the ambient temperature and the heating power P_{LF} that is supplied by the magnetic reader.

For example, in chapter 4 we have seen $f_1 \pm 2 \cdot f_2$ FMMD signal amplitude acquisition of biological *Enterococcus Faecium* assay calibration curves (S_{FMMD}). The concentration

intervals that can be reliably measured and therefore the error ranges were shown to relate to changes in the temperature in some way. Whether the observed signal changes depend on changes in the coil resistances, magnetization curves or are dependent on the biological reaction behavior is unclear. Rather than finding an analytical solution or mathematical correction algorithm (see appendix D), we decided to follow numerical approaches to better understand the thermal behavior of the sensor, explore thermal regulation strategies to circumvent these challenges and built a theoretical understanding of the problem. Numerically, the problem can be observed in its entirety and a separation into singular effects may not be necessary from an engineering perspective.

More specifically, in this chapter we will suggest different model developments to simplify investigation of transient thermal MH behavior depending on ambient conditions. In section 5.1, we suggest a linear LPM to approximate the thermal behavior at the LF coil surface. In section 5.2, we will introduce the methodology of LF measurement schemes for FMMD signal acquisition as an alternative to the offset scans discussed in chapter 3. By adding a resistance feedback to the linear LPM, we will receive a nonlinear model that incorporates the temperature coefficient of resistance. This model will be compared to a multiphysics finite element method (FEM) of a single-layer test coil utilizing a variety of different LF measurement scheme inputs, to test the validity of the LPM with additional physical constraints.

To achieve stable FMMD signals, [96] reported significant waiting times for coil heat-up, sometimes with time periods as long as 70-80 minutes to reach stable temperatures without regulation strategies. This is not practicable in a PoC setting for obvious reasons. We will therefore discuss how to access the identification of an optimal measurement scheme, that causes the least thermal fluctuation and therefore yields maximum excitation signal and detection coil resistance stability. This approach offers absolutely no measurement downtime compared to traditional approaches like duty cycle regulation. While a PWM strategy may have significant benefits in terms of regulation to a desired temperature (which will be discussed and applied for an example use case in chapter 6), it carries the significant drawback of increased excitation signal *'off-time'*, even under laboratory conditions, which can clearly be seen from approaches discussed in [96] in a stationary laboratory setup. Depending on the surrounding environmental conditions, this challenge may become even more predominant, which underlines the importance of alternative approaches.

The following sections have been taken, adopted and modified from [59] to some extent. Supplementary data to support or discuss the claims will be presented. Additional and ongoing research will be shared.

5.1 Readout Electronic Independent Lumped Parameter Model

5.1.1 Model Structure Design

The general model structure was designed using a grey box approach. The following assumptions (logical derivations based on physical intuition or measurement) were made to design the basic model structure:

1. The peak current through the LF coil was 240 mA, yielding a power dissipation of approximately 2.4 W, whereas the HF coil current of 20 mA led to just 7 mW of heating power, 350-fold lower than the LF power. Therefore, the first assumption is, that the LF power contributes significantly more to MH heating than the HF coil power. Due to this circumstance, we will ignore HF coil heating in the following and just consider LF coil heating.
2. The ambient temperature influences the heating and cooling processes of the MH (heat dissipation is influenced by the temperature difference between the system under test and its surroundings - Newton's law of cooling, Stefan - Boltzmann law).
3. From 1 and 2, it follows that the model has at least two inputs (ambient temperature and average LF power).
4. Heat transfer is a non-integer order process (hence, Padé approximations in the heating and cooling paths).
5. The MH can store a certain amount of heat energy (it has a heat capacity, respectively) denoted by C_{vol}.

The simulation was set up using MATLAB Simulink (version R2023b). As a numerical method for solving the model equations, the auto-select Bogacki-Shampine solver was used.

5.1.2 Model Parameter Estimation

The free model parameters (K_{LF},K_{AMB}, C_{vol}, $a_1 - d_5$) in case of the linear LPM were estimated by solving a least squares optimization problem. Its objective or cost-function definition can be seen in equation 5.2, where y_p is the predicted value and y_m is the measured value.

$$J = min \sum_{i=1}^{n} (y_{p,i} - y_{m,i})^2 \tag{5.2}$$

This optimization problem was solved using the parameter estimator of the system identification toolbox in MATLAB, which iteratively combines different parameters and compares a measured dataset to the model output for each iterative set of parameters. This process is repeated until a cost-function minimum is reached.

Alternatively, the python package '*mystic*' can be utilized with the differential evolution '*diffev2*' function call to optimize parameters using a squared error objective function from '*numpy*'. This was done in case of the resistance feedback model described in 5.2.1. For the initial parameter estimate, two strategies were applied. The first one involved manual initial guess adjustment, based on the estimated parameters for the previous model or if applicable literature values (as for example for the temperature coefficient of resistance α). The second approach relied on defining parameter ranges. The initial parameter guess was then randomly selected from the respective range. The advantage of the python approach for parameter optimization is, that it is more accessible and easier to customize in terms of tolerances and solution population definition, which determines how long one iteration may take.

5.1.3 Model Performance Metrics

To compare the measured data to the simulated model output, the normalized root mean square error (NRMSE) was determined. Normalization can be performed with respect to the mean of the measured response data or with respect to the range of data points ($y_{max} - y_{min}$). Depending on whether the NRMSE is normalized with respect to the mean or the range of the measured dataset, it is sometimes also called coefficient of variation (CV). The latter was used in this study and the NRMSE was calculated according to Equation 5.3.

$$NRMSE = \frac{\sqrt{\frac{1}{n}\sum_{i=1}^{n}(y_{m_i} - y_{p_i})^2}}{y_{m,\max} - y_{m,\min}} \tag{5.3}$$

with the number of measurements, n, the measured value y_{m_i} and the predicted value y_{p_i}. The residual variance between the measured data and the simulated output for an estimated set of model parameters is lower when the NRMSE value is small. Furthermore, considering a predictor variable (number of inputs to the system) adjusted statistical metric, the standard error of estimate (SEE) was used in the linear/multi-linear models. Closely related to the root mean square error (RMSE), it accounts for the degrees of freedom in the system (see equation 5.4).

$$SEE = \sqrt{\frac{\frac{1}{n}\sum_{i=1}^{n}(y_{m_i} - y_{p_i})^2}{n - p}} \tag{5.4}$$

with p being the predictor variable, accounting for the number of independent variables in the system under test. Accordingly, for additional intuitive depiction, the % agreement was calculated based on the adjusted R^2 value.

These measures were also used in the optimization process of the python approach to parameter estimation for each input. To determine the parameter distribution function in 5.4, kernel density estimation was used which is introduced in 3.3.

5.1.4 Measurement Head Thermal Lumped Parameter Model

Using a LPM approach, we can evaluate the transient thermal behavior of our system for arbitrary ambient temperature inputs at the location of interest. Of course, in reality the MH underlies a spatially varying temperature distribution that changes radially throughout its cylindrical shape. The zero-dimensional assumption of the lumped parameter model considers solely the transient temperature behavior. In other words, this model structure is limited to predicting a single point temperature. However, major contributor to power dissipation is the LF coil, and simplification of the overall spatially varying wire temperature to a single representative point is valid due to the typically small temperature gradients along the wire. This holds especially true in the context of the lumped capacitance approximation. Formally, if the Biot number $\ll 0.1$, the lumped capacitance assumption - the assumption of internally uniform temperature distribution - is valid [87, 107]. Conduction is a fast process compared to convection in this case, so that the spatial change of temperature is

marginal. With a characteristic length of $L_c = 0.005$m, the thermal conductivity of copper $k_{Cu} \approx 385 \frac{\mathrm{W}}{\mathrm{m\,K}}$ [84] and an estimated natural convection coefficient of $\bar{h} \approx 9.97\ \mathrm{W/(m^2\,K)}$ (calculated according to scenario B in appendix F), the Biot number equates to $\mathrm{Bi} = \frac{hL_c}{k} \approx 1.29 \cdot 10^{-4} \ll 0.1$.

The LPM interconnects the temperature output of the system $T(t)$ (LF coil temperature measured on the LF surface with a DS18B20 temperature sensor) to the average dissipated power from the LF coil (P_{LF}) and the ambient temperature (T_{AMB}) through an effective thermal capacitance term $\frac{1}{C_{vol}}$. A feedback loop of the output temperature to the T_{AMB} input shows the cooling/heating dependence on the temperature difference of the MH and its surroundings.

To explain this, let us first introduce the system represented as the underlying differential equation:

$$\frac{dT(t)}{dt} + \frac{K_{AMB}}{C_{vol}} T(t) = \frac{K_{LF}}{C_{vol}} \overline{P_{LF}} + \frac{K_{AMB}}{C_{vol}} T_{AMB}(t) \tag{5.5}$$

The term $C_{vol} \frac{dT(t)}{dt}$ may remind of the energy storage term in the heat conduction equation (see chapter 2, section 2.4) without the spatial dependencies of thermal diffusivity, that is density and thermal conductivity. It is the core piece that allows transient analysis and influences the time constant of the system. K_{LF},K_{AMB},C_{vol} are the main parameters in the model. K_{AMB}, K_{LF} scale the influence of the system inputs $\overline{P_{LF}}$ and T_{AMB} on the MH's thermal output behavior.

Generally, the right side of the equation is a function, describing the inputs of the system, equivalent to the standard heat conduction description. Based on the heat conduction equation supplemented by the assumptions defined in 5.1.1, the model structure was iteratively determined. A more intuitive way to depict this system and a typical approach in control theory is the illustration as a block diagram. Each part in the block diagram represents either an input, an output, a constant or a Laplace-transformed portion of the underlying differential equation that determines the system dynamics. Figure 5.1 shows the block diagram that represents the thermal behavior of the MH in time.

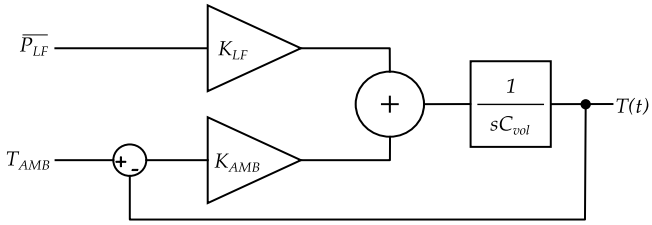

Figure 5.1: Block diagram of a lumped parameter model for the LF coil surface temperature.

In this block diagram, s is called the complex frequency variable (or Laplace parameter) resulting from the Laplace transform representing time derivatives at the order of the potency of s. The linearity of each transfer function in this first model structure allows the scaling of the input measures for achieving proportional changes in the model output. As can be seen easily from the differential form of the model, this is a linear first order multi-input single-output (MISO) system.

It was reported that heat conduction can be more accurately described by a non-integer order process [108]. We attempted integer-order polynomial approximations (Padé approximations) to model the non-integer order portion of the problem and enhance the accuracy of the model output compared to measured data. The higher the order of approximation, the more accurately the model output reflects the measured data. In one of the present cases, for example, a fourth order Padé approximation improved model accuracy in terms of the R^2 value by 13% over a second order Padé approximation. This improvement diminishes strongly with higher approximation orders. The drawback is that a higher number of parameters in the model is needed, so that the model requires higher computational parameter estimation effort and therefore more time [109]. Exemplary second order Padé approximations follow the form:

$$p_i^* = \frac{a_2 s^2 + a_1 s + a_0}{b_2 s^2 + b_1 s + b_0} \tag{5.6}$$

where p_i^* denotes the Padé block, with i being representative of the approximation purpose (heating (h) or cooling (c) influence, respectively) and a_i, b_i with $i = 0, 1, 2$ are constants. We decided to use two blocks of second order Padé approximations to "smoothen" the effect of each of the inputs $\overline{P_{LF}}$ and T_{AMB}. Multiplying the total system's transfer function by equation 5.6 equivalently for heating and cooling processes, enhanced the model accuracy. In case of the heat conduction equation, this would simply mean a multiplication with a term that represents the approximation (see equation 5.7).

$$\frac{dT(t)}{dt} + p_c^* \frac{K_{AMB}}{C_{vol}} T(t) = p_h^* \frac{K_{LF}}{C_{vol}} \overline{P_{LF}} + p_c^* \frac{K_{AMB}}{C_{vol}} T_{AMB}(t) \tag{5.7}$$

Translated into the block diagram, we get figure 5.2.

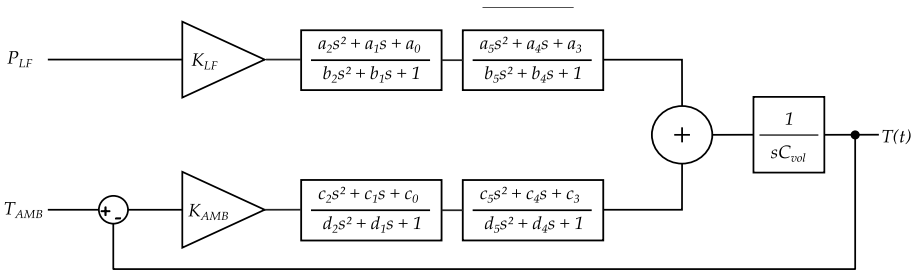

Figure 5.2: Block diagram of a lumped parameter model for the LF coil surface temperature with Padé approximations to enhance model accuracy [59].

The reason for using two blocks of second order approximations instead of one block of fourth order was simply that the computational effort is substantially reduced for two separate blocks in MATLAB. The values of parameters in each block can be seen in the description of a more practical use case in chapter 6, table 6.1.

When not using MATLAB simulink as a mediator for the model in form of a block diagram, the underlying differential equation is typically used for numerical simulations. To demonstrate coherence, one can equivalently derive the formulation of the heat conduction

equation by working backwards from the transfer function (TF)s of the model to equation 5.7, with the complex frequency variable s being equivalent to the time derivative $\frac{d}{dt}$.

5.1.5 System Identification and Validation

A model structure needs to be identified, for example by comparing the model output to a set of measured input and output data from the real system. If the error between the measured and simulated system output is acceptable, an independent second measured dataset needs to be used to validate the identification. In the present case, the measured output is equivalent to the temperature of the heating and cooling process of the MH upon application of the inputs, namely the LF driver signal and a recording of the ambient temperature T_{AMB} during application of that signal. The error between the simulated and the measured signal can then be iteratively minimized as suggested in 5.1.2, to find good parameters for the model.

In graph E and F of figure 5.3, we can see that the model captures the essential dynamics of the system very well, while seemingly ignoring faster changes in the ambient temperature inputs. This is due to the filtering nature of the model. In fact, the partial TF of the model output $T(t)$ with respect to the T_{AMB} input is very similar to the TF of a standard first order low pass filter. It is obtainable, using the Laplace transform of equation 5.5, that can be seen in equation 5.8. To find the relation of the output to a single input in a multi-input system, the other input, here the average power input $\overline{P_{LF}}$, needs to be set to zero. Then, we can reformulate the ratio of the system output to its input (equation 5.9) and we receive first order form that can be compared to the transfer function of a traditional low pass filter.

$$T(s) = \frac{\frac{K_{AMB}}{C_{vol}} \cdot T_{AMB} + \frac{K_{LF}}{C_{vol} R_0} \cdot \overline{P_{LF}}}{s + \frac{K_{AMB}}{C_{vol}}} \tag{5.8}$$

$$H_{T_{AMB}}(s) = \frac{T(s)}{T_{AMB}(s)} = \frac{\frac{K_{AMB}}{C_{vol}}}{s + \frac{K_{AMB}}{C_{vol}}} \tag{5.9}$$

The cutoff frequency of this filter is therefore $\frac{K_{AMB}}{C_{vol}}$, which determines whether the system responds to changes in the inputs or not, based on how rapidly it changes. For the parameters received for the model structure, represented in figure 5.2 (shown in table 6.1), a cutoff frequency of ≈ 0.001 Hz was calculated. This confirms the model reflects the slow nature of temperature change. Slow changes in the input will pass the filter property and rapid changes in the input will be attenuated.

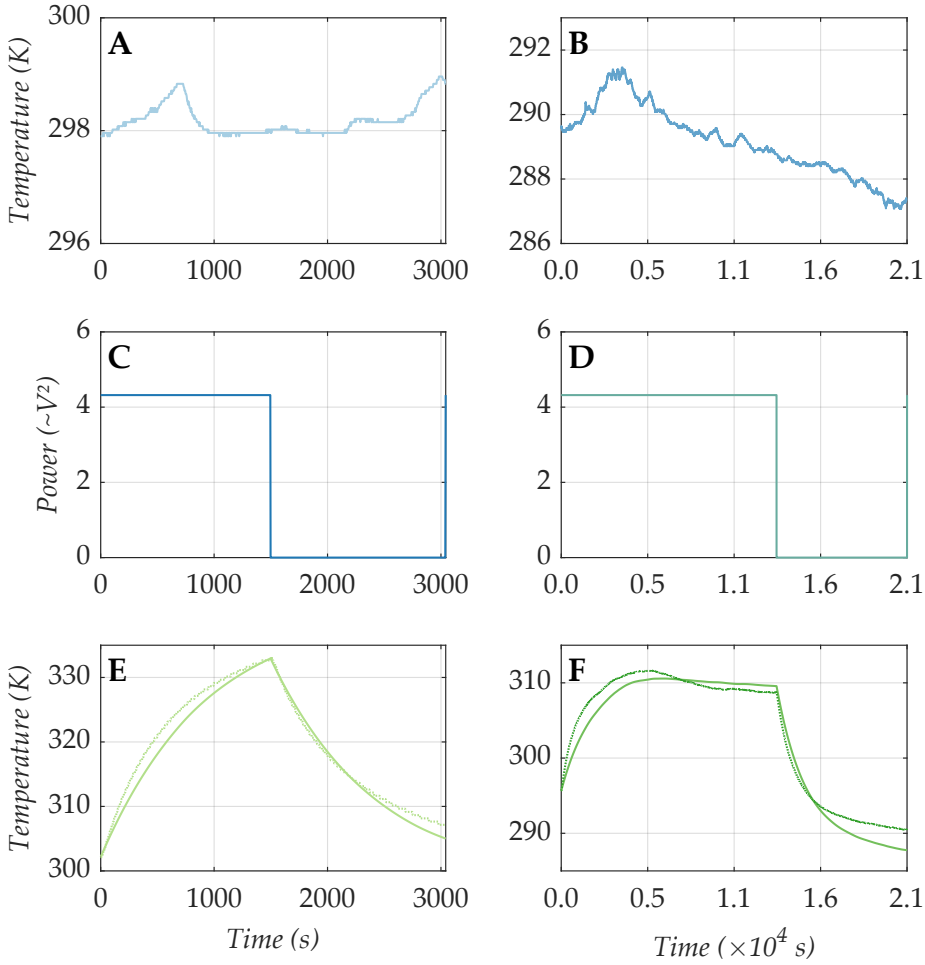

Figure 5.3: A and B are the measured ambient temperature inputs used for system identification (A) and validation (B). C and D depict the averaged power input used in each case. And E and F shows the system response to the inputs A-D (solid lines) and the measured data compared to it (dashed lines).

5.2 LF-Scanning and Measurement Schemes

The idea of the LF scan in comparison to the offset scan is to apply different LF amplitudes for a given time, rather than different magnetic offset-fields. Each of the applied LF amplitudes originates from logarithmic selection of values and is therefore unique during a single FMMD scan. Using this approach, the magnetization behavior of the superparamagnetic sample can be thoroughly scanned, especially in the nonlinear regime of the magnetization curve. The immediate technical advantages are, that no additional offset-generating circuitry or EM is needed. Additionally, the potential risk of electrical coupling effects between offset voltage and LF voltage in the electronic readout is mitigated.

The maximally achievable coil currents can furthermore be utilized to generate higher LF amplitudes rather than compromising between offset-field and LF amplitudes applied through the same load resistance (LF coil). This in turn allows for a broader range of superparamagnetic particles to be investigated and therefore widens the area of application.

The order in which the different LF field amplitudes are applied is generally variable. In the present setup developed by Timur Bikulov, the 40 unique amplitude settings are applied in sequence, each of which is maintained for $22s$. In this work, a variety of restructured measurement schemes were designed.

The designed measurement schemes were applied to a newly developed '*resistance feedback*' LPM and a COMSOL FEA. The aim was to identify measurement schemes, that potentially cause less thermal and thus less resistance changes. We propose, that such an optimized measurement scheme could then be utilized as a thermally optimized LF input in FMMD signal acquisition, for scanning the complete magnetization curve.

5.2.1 Resistance Feedback

Often, there are multiple, even mutually inconsistent model structures used to represent the same real system in physics under different initial conditions or with different sets of parameters [110]. For example, selecting the average of the LF power as an input and applying an approximation function like the Padé approximation, we can compensate for changes in the model output, such as those that would be caused by temperature-dependent resistances and the resulting variation in input voltage. This approach yielded excellent performance. It works particularly well when being applied to a model whose output is thermally regulated, ensuring that resistance fluctuations remain relatively small. Another advantage of this approach is that the model remains linear, which reduces the required simulation time especially for parameter optimization significantly and simplifies its implementation. For testing the performance of designed thermal control algorithms, the model is also very well-suited.

So while the previously discussed LPM stays valid, physical significance can be added by feeding back the temperature output through a TF that represents a temperature-dependent resistance, thereby influencing the input power. This allows for a more detailed investigation of the effect of resistance change (depending on the ambient conditions) on the applied input. This becomes especially important, if we want to minimize the measurement time needed, when not using PWM approaches with their undefined '*off-time*' to regulate to a desired temperature value, but rather optimize the input in terms of the least possible temperature fluctuations for a given set of amplitudes.

In terms of model structure assumptions formulated in section 5.1.1, we add:

- A change in LF coil wire resistance due to temperature changes can be approximated by the linear function: $R_0(1 + \alpha(T(t) - T_0))$, where R_0 is the resistance at a temperature T_0 and α is the temperature coefficient of resistance. If not averaged, the LF power input changes based on the change of wire resistance. We can modify the resistance-dependent power input by multiplying the applied squared voltage with the inverse of the linearly approximated resistance.

The resulting adjustment in the model structure can be seen in figure 5.4.

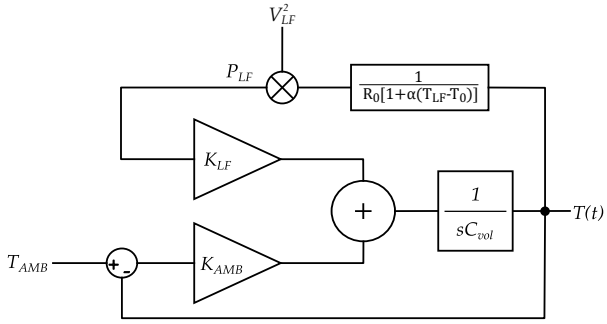

Figure 5.4: Block diagram of a lumped parameter model for the LF coil surface temperature depending on the changes in resistance with temperature.

For simplicity, the corresponding Padé approximation of the heating and cooling paths is omitted in 5.4. The energy conservation is thus given as shown in equation 5.11.

$$\underbrace{C_{\text{th}}\frac{dT(t)}{dt}}_{\text{rate of energy change}} = \underbrace{-K_{\text{AMB}}T(t)}_{\substack{Q_{\text{out}}\\ \text{cooling}}} + \underbrace{K_{\text{AMB}}T_{\text{AMB}}(t)}_{\substack{Q_{\text{AMB}}\\ \text{ambient}\\ \text{contribution}}} + \underbrace{\frac{K_{\text{LF}}V^2(t)}{R_0(1+\alpha(T(t)-T_0))}}_{\substack{Q_{\text{gen}}\\ \text{heat generation}}} \tag{5.10}$$

$$\frac{dT(t)}{dt} = -\frac{K_{\text{AMB}}}{C_{\text{th}}}T(t) + \frac{K_{\text{AMB}}}{C_{\text{th}}}T_{\text{AMB}}(t) + \frac{K_{\text{LF}}}{C_{\text{th}}}\frac{V^2(t)}{R_0(1+\alpha(T(t)-T_0))} \tag{5.11}$$

To better understand the behavior of the system in a context of varying input signals, let us define the effect of parameter changes more clearly. K_{LF} acts as an amplification factor for the influence of the $\frac{V^2}{R_0(1+\alpha(T(t)-T_0))}$ input on the system output $T(t)$. Therefore, a high K_{LF} increases the magnitude response for all frequencies in the input. K_{AMB} determines, how strong the heat dissipation to the surroundings is. A high K_{AMB} value consequently means weaker damping or, in other words, it enhances the system's response to faster changes. A higher C_{th} will lead to larger time constants, which causes the system to react more sensitively to low frequency components (slow changes in the input signal), and high frequency components will be filtered more rigorously. Vice versa, a low C_{th} will lead to more sensitivity towards higher frequencies in the input signal. So both, K_{AMB} and C_{vol} influence how fast changes in the input signal can be captured in the system response. Furthermore, it is very important to notice, that the temperature coefficient of resistance α leads to a nonlinear feedback loop. The magnetic reader is a voltage controlled system, which means that the electrical current is not necessarily kept constant, especially when the load resistance changes. Thus the change in resistance influences the power input inversely. For very small values of α, the influence is minimal, as $(T(t) - T_0)$ approaches 0 and the denominator of the feedback thus approaches 1. However, already at the order of $\alpha \approx 0.001$

($\frac{1}{4}$ of the literature value of copper), its influence on the system output can be critical. The effect of higher α values is a stronger modulation of frequency components and therefore might influence the amplification caused by K_{LF}. This makes clear, that the nonlinearity in the system makes it substantially more difficult to attribute the system behavior to a certain parameter influence, since the significance of the change in a parameter can be different depending on the state of the feedback. Also, nonlinear models cannot easily be represented as transfer functions or even in state space without linearization. It is feasible, however, to use data-driven approaches for system validation that do not necessarily require too complicated analysis. The approach used in this work will be discussed in section 5.4.

5.3 Transient COMSOL Finite Element Modelling of a Single Layer Coil

The adjusted LPM will be tested by using a multiphysics FEA of the problem at hand, performed with the software COMSOL, version 6.2.0.415. To be able to robustly test the models, a variety of different, artificially generated input shapes as described in section 5.2 were presented to both models and the corresponding outputs were compared. It was attempted to optimize the LPM parameters by fitting the models to each other and evaluating the objective function formulated in equation 5.2 for many iteratively adjusted sets of parameters. Furthermore, using FEA, it is possible to investigate phenomena like electrical, thermal and magnetic behavior over time (magnetic field amplitudes, heat dissipation, resistance changes), magnetic shielding capabilities and the existence of eddy currents, just to name a few. The model can also be utilized as a basis for new MH designs or design adjustments.

Since the amount of inputs tested cause very large simulation times already, and to test the approach in general, a simplified test problem was evaluated first, using a single-layer test coil rather than the complete measurement head. The results and comparison of the two models will be discussed in section 5.4. This section describes the setup of the FEA in COMSOL.

5.3.1 Finite Element Model Setup

Problem Definiton

The single-layer coil is a first test model, the extension of which will later lead to a model describing the total MH. The material and geometrical parameters used, correspond to the LF coil measures used in the MH for FMMD (see section 3.1 and appendix C), except for the number of coil turns. This study is particularly focused on the heat transfer within the miniaturized coil system, more specifically the average and single point change in temperature on the coil surface. We want to find the thermal reaction to different electrical inputs, in order to find the electrical stimulus suitable for FMMD, that creates the least thermal and resistance fluctuations possible. Validation of the models at hand should be performed by LPM and COMSOL model output cross-comparison. Finding the optimal measurement schemes is proposed to reduce measurement error and increase excitation signal stability, as the resistances in the system are stabilized, while minimizing measurement downtime. The proposed principle should be extendable to

other magnetic scanning techniques with inductive readouts, that suffer from influences of thermal variations.

COMSOL Physics Interface

For the base model, the packages '*magnetic fields*' and '*heat transfer in solids*' were utilized. The corresponding multiphysics module used was '*Electromagnetic Heating*', coupling the base model physics.

Geometry and Domains

The COMSOL model is axi-symmetric. As such, the geometry was defined in cartesian coordinates and later rotated 360° around its central axis. The length, thickness, inner and outer radii were globally parametrized. The wire diameter of the copper wire was 0.18 mm with a cross-sectional area of $3 \times 10^{-8}\,\mathrm{m}^2$. The length of the air-filled, hollow LF cylinder, that defined the length of the single coil layer, was 24 mm, and its diameter was set to be 6.5 mm. The parametric design enables easy adjustment of the geometrical measures in the model. Therefore, it can also easily be extended to the entire measurement head geometry later on. In cartesian coordinates, a circular domain was defined as the control volume that defined the air space in which the simulation was carried out.

The kind of coil used was specified in the *Magnetic Fields* tab using the homogenized multi-turn coil option, with a number of windings $N = 120$. The coil conductivity was taken as the electrical conductivity of copper, $6 \times 10^7\,\mathrm{S/m}$, divided by the temperature dependence of resistance. The ambient temperature was subtracted from the immediate temperature value for each time step of the electromagnetic heating multiphysics simulation to account for the change in resistance with temperature.

External Inputs and Boundary Conditions

The electrical current input to the coil was provided by a function switch, shifting through a variety of piecewise linear functions representing the electrical current based input measurement schemes, described in section 5.2 and partially depicted in figure 5.5 A, B and 5.6 A-D. In the frequency-transient study, the different amplitudes specified within these measurement schemes were applied sinusoidally at a constant frequency of 62 Hz, equivalent to the frequency used for LF excitation in FMMD.

As the main way of heat dissipation, the heat flux q''_{rad} (heat rate q_{rad} times the unit area, see 2.1) was defined. This '*Surface to Ambient Radiation*' (nonlinear Neumann condition) was then applied to the outer and inner boundary of the single layer coil. Therefore, a surface property node was created to define surface emissivity of the coil material. A thermal insulation boundary condition was applied to the boundary of the control volume. More particular, a Neumann condition was applied in the form $-n \cdot q'' = 0$, so that the heat flux at the boundary equals zero [111].

Alternatively, a fixed temperature boundary condition (Dirichlet) can be set on the outermost boundary, forcing the temperature to decay to the ambient temperature value T_{AMB}, 10 cm apart from the coil center. 10 cm is the radius of the whole orbital domain volume.

To ensure that no magnetic field lines pass the defined air boundaries, equivalently to the thermal insulation, a magnetic insulation boundary conditions was applied. It "sets the tangential components of the magnetic potential to zero at the boundary $n \times A = 0$" [112], where A is the magnetic vector potential.

The axial symmetry conditions are automatically applied by the selected 2D axi-symmetric model type.

Initial Conditions

The ambient properties were defined as ambient temperature $T_{AMB} = 293.15\,\mathrm{K}$ at an absolute pressure of $10^5\,\mathrm{Pa}$. Clear sky noon beam normal irradiance of $1000\ \mathrm{W \cdot m^{-2}}$ was used. Here, weather conditions would be adjustable in the COMSOL model. The initial value for the temperature simulation in all domains and boundaries of the geometry was $T = T_0$, with $T_0 = T_{AMB}$. While the ambient properties were kept constant throughout the simulation, the executed study was a frequency-transient study, taking into account the alternating input current as well as the development of material temperature over time.

Meshing

An automatically generated fine, physics-controlled mesh was used for the multiphysics simulations, with no mesh refinement being used.

Studies and Simulation

Using the '*Coil Geometry Analysis*' study for each input function sweep, the resistances, linearly dependent on temperature, were extracted. A resistance at reference temperature $(293K)$ of ca. $3.5\,\Omega$ was the starting point for the single layer coil simulation.

Using the '*frequency-transient study*', the change in heat transfer and magnetic fields with changing resistances over time was studied.

Exemplary images of the 2D axi-symmetric heat transfer, magnetic field and current density simulation outputs are presented in appendix G. In the main part of this thesis, we will focus on the average temperature response along the outer coil surface for model cross-comparison (figure 5.5, 5.6).

The total simulation time was 1000 s with 10 second time steps. However, since the input signal duration was 880 seconds, the simulation duration will only be visualized to that point in time.

Simulation Post Processing

Line plots of temperature over time as well as average temperature over time and resistance over time were extracted. As the change in resistance with temperature was defined by a linear approximation, the resistance graphs are not shown here. Their shape behaves congruently to the temperature simulations on a different scale.

5.4 Model Comparison

The resistance feedback LPM was compared against the COMSOL model for different voltage inputs to seek model identification. Since the duration for the FEA for the large number of different inputs with relatively long simulation times (880 seconds) requires significant computational power, the size of the time steps was selected to be relatively large with 10 seconds. The sharper edges resulting from these larger time steps, may cause challenges, when trying to fit the smooth LPM data. Therefore the COMSOL simulation output was low pass filtered, to ensure smooth continuous transitions, before comparing it to the LPM output.

The bounds for the parameter estimation process were determined using a heuristic approach. The linear model identification in 5.1.5 yielded for example $C_{th} = 36$ (6.1), which was the lower C_{th} boundary used in the estimation process for the resistance feedback model. The upper boundary of C_{th} was determined by iterative testing. Similarly, the bounds for K_{LF} and K_{AMB} were defined. The initial guess ranges were narrowed down from larger ranges, specified based on multiple simulation results. After the boundaries were defined, the parameter estimation process was repeated within the defined boundaries. The boundary ranges are therefore defined as shown in 5.12.

$$K_{LF} \in [0.1, 30], \quad K_{AMB} \in [0.01, 3], \quad C_{th} \in [36, 100]. \tag{5.12}$$

The initial guesses are within the intervals shown in 5.13, which correspond to parts of the total boundary ranges.

$$K_{LF}^{(0)} \in [1, 20], \quad K_{AMB}^{(0)} \in [0.01, 2], \quad C_{th}^{(0)} \in [45, 95]. \tag{5.13}$$

If the boundaries and initial guess ranges for the parameter estimation were to be adjusted for every input to find the corresponding optimal parameters, we may achieve better results for individual inputs. However, if we do so, we observe bi- or even trimodal parameter distributions in some cases. This suggests that different sets of K_{LF}, K_{AMB} and C_{th} parameters are viable to fullfil the model requirements. One could argue that this may be traced back to even more inputs that are needed to test and extend the necessary parent population. But it is more likely that the relation of the parameters to each other and their effect on the model output repeat. For example, as shown in 5.11, the parameters K_{LF} and K_{AMB} occur only in combination with C_{th}. If both parameters are adjusted by the same margin, their fraction does not change. In the nonlinear environment of the resistance feedback model, this could still apply for certain combinations of parameters.

While the variable parameters in the LPM changed for each input, the general system dynamics could be represented very well for power inputs with a slow rate of change.

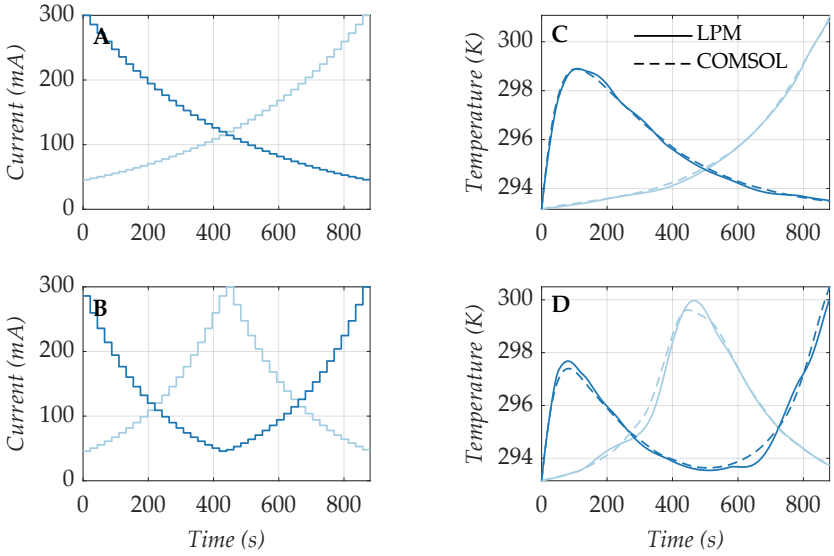

Figure 5.5: Plots A and B exemplarily show slowly changing LF measurement schemes. Plots C and D show the corresponding LPM and COMSOL model responses. Which model output belongs to which input is additionally color-coded.

Here, applied electrical currents are plotted to better reference maximally achievable coil currents. However, they can easily be scaled to a voltage applied to a reference resistance R_0 by multiplication according to Ohm's law. This is the input that was fed to the resistance feedback LPM. It is important to note, that the magnetic reader is a voltage controlled system. Therefore, the COMSOL multiphysics simulations should be repeated with constant voltage inputs, instead of constant current inputs.

As already mentioned in section 5.1.5, inputs with frequencies much higher than the cutoff frequency force the system to react to changes on a much shorter timescale than it is naturally equipped to handle, which may create oscillations in the solution. On the other hand, these oscillations require small time steps for accurate resolution in the simulation. So the generally slow system dynamics can result in a '*stiff*' reaction, if the input magnitude changes with a higher frequency.

In figure 5.6 C, it is observable that when the rate of change in the input power rises, the model output seems to be more phase-deviated at first. If the rate of input change is increased even further, the phase change cannot be compensated by parameter adjustments anymore, leading to instabilities, as can be seen most severely in figure 5.6 H at around 400 seconds. The parameters in the model are dependent on each other. If the thermal capacitance as a parameter is increased, K_{AMB} has the tendency to become larger. In other words, if the thermal energy is stored for longer, the factor that scales heat dissipation to the surroundings also needs to increase. For this reason, the model becomes the more unstable, the higher the discrepancy between K_{AMB} and C_{th} is. The change in the fraction of these two parameters may lead to fluctuations in the model output. For constant K_{AMB} and K_{LF}, a decreasing C_{th} has the same consequence. In a physical context, that means that the thermal energy can only be stored for a small amount of time if the thermal

capacitance is small. However, if a high C_{th} value is selected without adjusting the scaling factor (the influence of the input power (K_{LF})), the cutoff frequency of the system becomes larger, which lets higher frequencies pass, thus influencing the output dynamics. The COMSOL simulation does not reflect this influence of higher frequencies in the input.

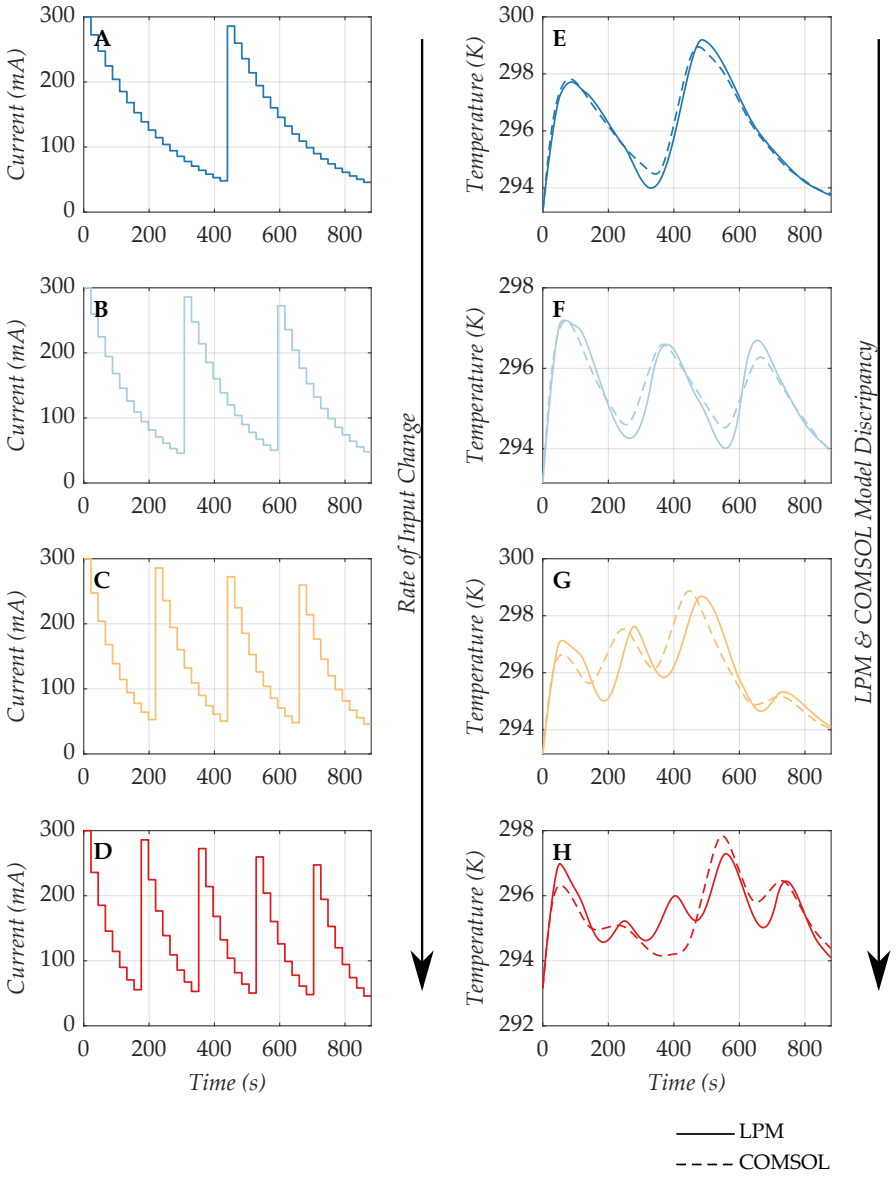

Figure 5.6: Plots A-D show examples for LF measurement schemes with an increasing rate of change in supplied electrical current along the vertical arrow on the right side of the input graphs. Plots E-H show the corresponding LPM and COMSOL model responses. Along the indication arrow on the right side of plots E-H, the discrepancy between the models increases.

In summary, for small input power frequencies, this model works very well, assuming literature values for the temperature coefficient of resistance of copper. Higher frequencies in the input power, however, may lead to unstable behavior, which can be due to several reasons:

1. Major way of heat dissipation in the COMSOL model is natural or mixed convection and not surface to ambient radiation. The result might be different time constants in the cooling and heating processes.
2. Solver adjustments may be necessary for reaction of the system to higher input frequencies.
3. Padé approximations were omitted for the nonlinear model, but as stated by Oprzedkiewicz et al. [113], these approximations may represent the non-integer order nature of the problem. Also, Padé approximations may mimic a missing input filter, supporting the nonlinear LPM.

So, this difficulty may be circumvented by pre-filtering of the inputs or selecting more suitable solvers. An adjustment of the COMSOL model may even be necessary in terms of the dominant way of heat dissipation, rather than a change in the nonlinear LPM. Qualitative assessment of the simulation results suggest that the LPM follows the respective input measurement scheme more closely, which was initially expected for the given timescale. Experimental data to compare both models or validate them individually against empirical measurements would be necessary to make further claims.

5.5 Outlook: Towards an Optimal Measurement Scheme

Once, the current nonlinear LPM structure is validated, the model outputs can be utilized to find the measurement scheme input that causes the least thermal changes in the system. In order to achieve that, different metrics can be used. The standard deviations of the temperature outputs around its mean can be a good measure if the priority is to minimize temperature variance. This in turn minimizes resistance variance, which is one of the goals. At the same time, the standard deviation will incorporate outliers. So an additional metric may be the maximum temperature change, which determines the largest deviation of the temperature from a selected reference baseline that is caused by an input. The integral of the temperature output can also be a useful measure, as it captures the cumulative deviation of the temperature from a baseline value over time. Minimal integral implies minimal overall temperature fluctuation.

In future, the temperature model and the resulting input power measurement scheme could be applied to the magnetic nanoparticles. Connection of the temperature model to a model of the inductive coil environment of the MH may lead to a holistic approach and testing environment for electrical property and FMMD signal variation. This way, different MH sensor designs, new particle types with different magnetization behavior and severe environmental influences could be tested fast and easily in a computational setting.

A practical test for a biological example application will be described in chapter 6, where RPA was used to validate that the linear LPM and the achievable control accuracy with simple control strategies is sufficient for biological use cases.

Chapter 6

Isothermal Amplification using Temperature Controlled Frequency Mixing Magnetic Detection Sensor Unit

In this chapter, an extended PWM logic is introduced in 6.1. This controller will be used to show feasibility of temperature controlled DNA amplification in form of RPA inside the sensor unit. We access basic controller-performance at the sample position in section 6.2 and then test the feasibility of RPA performed in the MH in section 6.3. To foresee changes in control performance in a real-world setting, we introduce a linear extrapolation model to investigate thermal behavior at the sample position in section 6.4. While this model is sufficient to investigate the effects of steady state ambient temperatures, this chapter will also expand the LPM (shown in 5) to simulate transient temperature changes at the sample position of the MH in a mobile (or stationary) setting. Using the original model output as a controller input, scaling it, adding a delay term and feeding it to the sample position part of the model, we expect that it can be used for NA amplification and improve magnetic detection using FMMD in resource-limited settings.

In chapter 4, section 4.1.3 we considered a use case for a magnetic antibody immunoassay. It was showcased in recorded calibration curves how biological concentration determination differed when conducting the measurement in thermal chambers at different but constant ambient temperature levels. To achieve a constant device and sample temperature, a preheating time of the device of ca. 70 minutes and a preheating time for the sample of ca. 10 minutes were necessary. The implemented regulation approach can also be applied to help facilitate the assay preparation, and stabilize the concentration measurement variations.

Large parts of the content in this chapter, including adopted graphs, were taken from material published by the writer [59].

6.1 Pulse Width Modulation

A 2-point PWM feedback controller for LF-amplitude duty cycle adjustment and therefore controlled heat supply was implemented in the Arduino microcontroller software (version v2.20.2) of the magnetic reader. The feedback temperature sensor used for control was a DS18B20 sensor from Maxim Integrated Products, Inc. (San Jose, CA, USA), mounted on the LF coil surface inside the measurement head. The suggested control algorithm incorporates two distinct, freely selectable error ranges. A first, wider error range for tuning the temperature in the desired interval and a second, narrower error range within which the temperature is kept during the FMMD measurement process. This makes it generally possible to heat up the amplification environment with maximum power fed to the LF coil, but then regulate the heat with, e.g., only half maximum power. The conditional equivalent logic for the duty cycle regulation within these error ranges based on the temperature difference between the measured output temperature and the set desired temperature input value followed the scheme in figure 6.1.

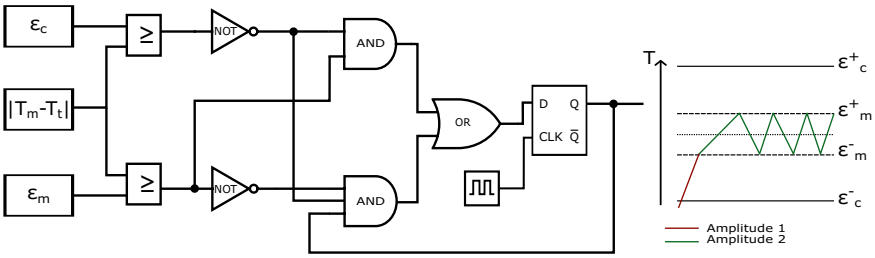

Figure 6.1: Equivalent logic for a PWM controller with differentially adjustable heating and measurement LF amplitude and schematic of controlled temperature using this logic.

Here, ϵ_c denotes the allowed temperature error range during heat up and tuning and ϵ_m denotes the allowed temperature error range during the FMMD measurement. T_m is the measured temperature at the LF coil surface and T_t is the set controller target temperature. The output of this equivalent logic defines the condition that determines if the LF amplitude is turned on or off with a first amplitude setting (Amplitude 1) or a second amplitude setting (Amplitude 2), different from the first one. Software-wise, this logic was implemented into the Arduino microcontroller using multi-tasking programming with a time-slicing scheduling technique to account for the wait time of the temperature sensor and measurement readout.

6.2 Controller Performance

Before testing the feasibility of RPA in the MH, the temperature controller should briefly be investigated in terms of its reliability in a test (lab) setting. While performing any NA amplification as well as during FMMD signal acquisition, the sample to be amplified or measured is inside the sample bore of the MH. Due to geometrical restrictions, sample and temperature sensors cannot be installed simultaneously at the current stage. Hence, the temperature sensor used for feedback control was mounted on the surface of the LF coil in the MH, a small distance apart from the center of the sample position. To visualize

this, please refer to the schematic of the MH, the temperature sensor and sample position, as well as the principle of the power to temperature conversion in Figure 6.2.

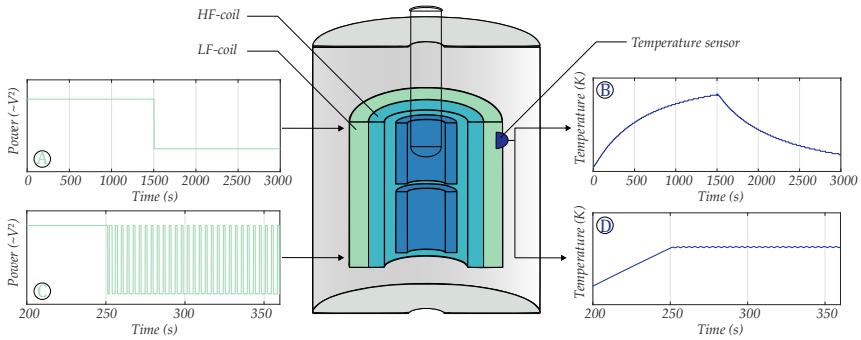

Figure 6.2: Schematic of the measurement head cross section, including the temperature sensor position. (A) Uncontrolled LF power input step. (B) Uncontrolled temperature output corresponding to the input depicted in (A). (C) Pulse width modulated low frequency power input. (D) Adjustable temperature output corresponding to the PWM input depicted in (C). Adopted and modified from [59].

Because of distinct control and amplification locations, it is important to not only characterize the controller and controllable temperature ranges at the position of the feedback sensor, but especially to test the temperature control at the sample position that is not directly controlled. The feedback sensor behavior was characterized for 10 different feedback temperature settings (30, 37, 38, 39, 40, 41, 45, 48, 50, 53 °C) set in ascending (heating) and descending (cooling) order between room temperature and 53 °C (Figure 6.3 A-D, solid lines). The corresponding temperatures at sample position were recorded with an epoxy-passivated temperature sensor in DI-water simultaneously (Figure 6.3 A-D, dashed lines).

The heating and cooling profiles at the sample position were determined for several different steady ambient conditions at 16 °C, 18 °C, 21 °C and 23 °C, similarly. To determine the sample position temperature for any feedback controller setting, first a "calibration" was performed. The relation of the temperature at the region of interest (sample position) was plotted against the temperature at the more accessible LF surface location, suited for controlling (figure 6.3 E). This way, a linear relationship of T_s (sample temperature) and T_f (feedback temperature) could be ensured to easily select the necessary amplification temperatures at the sample position. To initially estimate the reliability, the measured data at the recorded ambient temperatures were used to test the PWM controller strategy (at the sample position, where the amplification happens) in terms of heat up and cool down time constant, hysteresis and temperature control stability. The heat up and cool down time constants $\tau_{h_{16-23}}$ and $\tau_{c_{16-23}}$ were determined by exponential fits for each step of the heating and cooling data, respectively (plots can be found in Supplementary Figures S2 and S3).

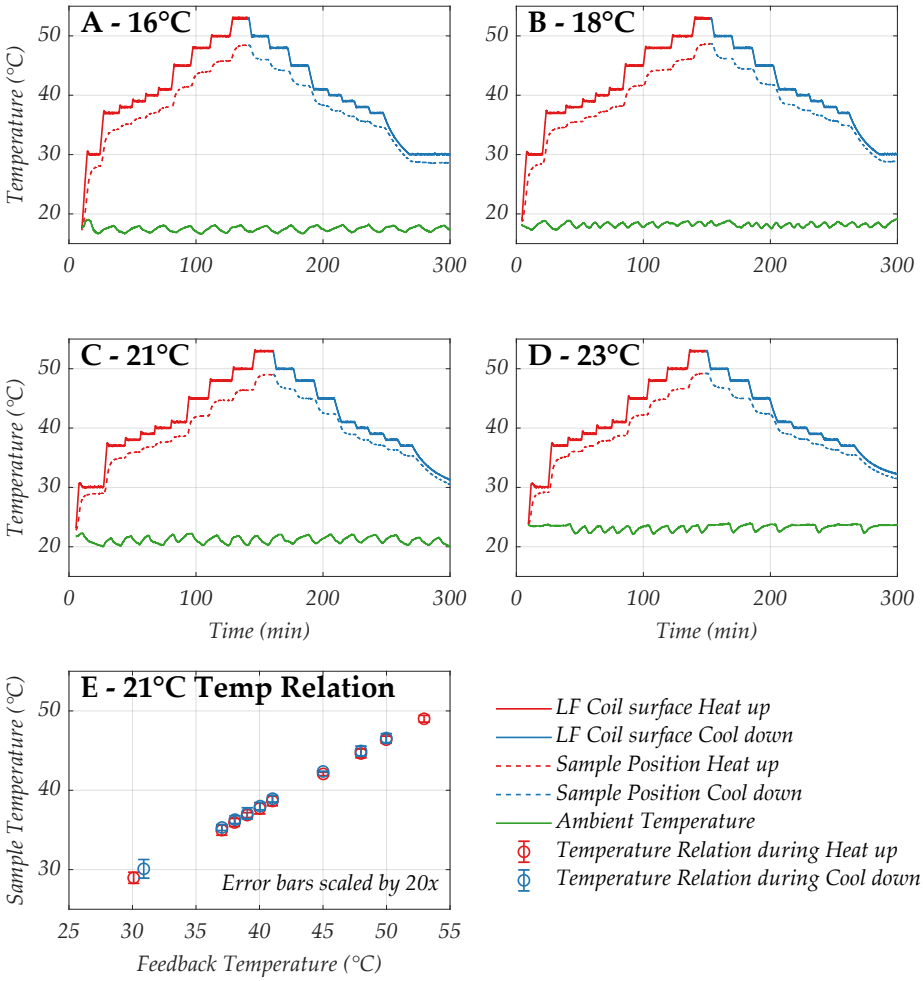

Figure 6.3: Recorded characterization data for feedback temperature control, sample position temperature and ambient (laboratory) temperature of 16 °C, 18 °C, 21 °C, 23 °C *(A-D) and linear exemplary dependency of controller temperature vs. sample position temperature at* 21 °C *(E). The standard deviation bars in E are scaled by* 20× *and indicate the stability of the temperature control at sample position. Adopted and modified from [59].*

The temperature data were fitted from their inflection point to the last point of their saturation by:

$$T_h(t) = K_h \cdot \left(1 - \exp\left(\frac{-(t - t_d)}{\tau_h}\right)\right) \tag{6.1}$$

The cooling data were fitted similarly with a decreasing exponential:

$$T_c(t) = K_0 + K_c \cdot \exp\left(\frac{-(t - t_d)}{\tau_c}\right) \tag{6.2}$$

where for the heating process fit, $T_h(t)$ eventually approaches the asymptotic value K_h. For the cooling process fit, $T_c(t)$ eventually approaches the offset-term K_0, while K_c indicates the initial deviation from K_0. The time t_d is the initial time and $\tau_{h,c}$ represents the time constant. The average heating and cooling time constants were calculated to be $\tau_{h16-23} = 137.13\,\text{s}$ and $\tau_{c16-23} = 158.59\,\text{s}$, respectively. Therefore, for all characterized $1-7\,^\circ\text{C}$ step cases, $\frac{2}{3}$ of the steady state signal was reached in less than 2.3 min for heating and 2.7 min for cooling. The hysteresis (here, the difference in temperature level for each step of the heating process compared to the corresponding step of the cooling process) of both, the feedback control temperature and the sample position temperature were determined for the same datasets. The average hysteresis of the PWM controller at feedback temperature position was calculated to be below the resolution limit of the digital DS18B20 temperature sensor ($< 0.0625\,^\circ\text{C}$) and therefore was not considered. The hysteresis of the temperature control at the sample position averaged $0.29\,^\circ\text{C}$ ($> 4\times$resolution of DS18B20). Although temperature control accuracy is crucial to ensure consistent amplification yield, RPA is generally feasible within a relatively large temperature span ($37-42\,^\circ\text{C}$). We defined a requirement of a $1-2\,^\circ\text{C}$ fluctuation at maximum, while in any case staying below $42\,^\circ\text{C}$, which could denature RPA components. The determined hysteresis at the sample position is therefore negligible. After reaching the desired steady temperature at the sample position, the importance of control stability becomes obvious. Therefore, the temperature stability of each temperature step was determined by means of its relative and absolute deviation from the mean over a 10 min time period, equivalent to the time that is at least needed for a recombinase polymerase amplification process [114],[115]. For all previously described constant ambient conditions, a maximal stability error of less than 0.3% was observed. A marginal error of 0.3% would amount to an absolute change in temperature of about $0.11\,^\circ\text{C}$. Considering the maximum error within standard RPA operating temperature ranges from $37-42\,^\circ\text{C}$ even stays below a 0.1% deviation. This peripheral temperature instability during the amplification process will not influence the efficiency of RPAs or most other biological reactions significantly.

6.3 Recombinase Polymerase Amplification in the FMMD Sensor Unit

6.3.1 RPA Reagents and Execution

TwistAmp® Liquid Basic kit was obtained from TwistDx™ Ltd (Maidenhead, United Kingdom). GeneRuler Ultra Low Range DNA Ladder, and DNA Gel Loading Dye (6×) were purchased from Thermo Fisher Scientific™ (Langerwehe, Germany). ROTI® Prep PCR Purification, and Agarose standard were obtained from Carl Roth GmbH (Karlsruhe, Germany). RedSafe DNA stain (20000×) was obtained from Hiss Diagnostics GmbH (Freiburg im Breisgau, Germany).

The RPA for positive control reactions was performed following the manufacturer's rec-

ommendation in the TwistAmp® Liquid Basic kit, with slight adjustments by reducing the reagent quantities to create a total volume of 25 μL. In the RPA reaction, a master mix was prepared containing 3.5 μL of oligo mix primers, 12.5 μL of 2× reaction buffer, 2.5 μL of 10× basic E-mix, 2.75 μL of dNTPs and 1.25μL of 20× core reaction. After mixing, 2 μL of MgOAc and 1 μL of positive control DNA were added to start the reaction. The RPA reaction was carried out at desired incubation temperatures and time inside the measurement head. After the amplification, the RPA was purified using ROTI® Prep PCR Purification kit through column centrifugation to remove reaction components. For the visualization of RPA products, 10 μL of the purified amplicons was analyzed using agarose gel electrophoresis on 2% agarose gel in 1× Tris Borate Ethylene Diamine Tetraacetic Acid (TBE) buffer at 100 V for 1h. The visualization was conducted with the charge-coupled device (CCD) camera ChemiDo™ XRS Imaging System (Bio-Rad Laboratories Co., Ltd., Hercules, CA, USA).

6.3.2 RPA validation using Gel-Electrophoresis

To test the functionality in terms of amplifying DNA at the sample position, we performed RPA in our temperature-controlled measurement head. The selection of RPA was based on its rapid amplification time compared with others techniques like loop mediated isothermal amplification (LAMP), rolling cycle amplification (RCA), nucleic acid sequence based amplification (NASBA) with similar sensitivity and specificity [116]. The typical incubation time of RPA is between 20-30 minutes [117]. However, several studies showed the capability of RPA to amplify DNA in less than 10 minutes [114],[115]. We achieved rapid and efficient amplification using our portable magnetic reader. By combining RPA with our previous work, which demonstrated the ability to rapidly detect amplified DNA in less than 10 minutes [63], a PoC analysis system can be suggested that does not require any sample pre-treatment in laboratories. As a proof of concept, we performed RPA amplification using the positive control template and oligo mix primers provided in the TwistAmp® Liquid Basic kit, which is expected to produce an amplicon of 289bp. The RPA reaction operates at constant temperature, typically between 37 °C and 42 °C. This temperature range is based on the optimal activity of the enzymes involved in the reaction such as recombinase enzymes, polymerases and other components. In our study, we tested the amplification across a range of temperatures, including 21 °C, 30 °C, 37 °C, 38 °C, 45 °C, and 50 °C. The selection of temperatures was chosen to investigate the amplification efficiency both within and outside the optimal operating temperature range of RPA. This way, we could assess how the variations of temperature controlled by PWM affect the performance of RPA amplification from the biological perspective. The amplification was done both inside our temperature-controlled measurement head and in a water bath as a reference method. In both cases the temperature was ranging from 30 °C to 50 °C with an incubation time of 30 minutes. Figure 6.4 shows the gel image of the RPA products amplified inside our measurement head and in a water bath, controlled to different temperatures. From the gel image, we confirm the successful RPA positive control amplification as the expected amplicons with the size of 289bp were observed at 37 °C and 38 °C in both our measurement head and water bath. When the amplification was tested outside the operating temperature of RPA, such as at low temperatures (21 °C and 30 °C) and at high temperatures (45 °C and 50 °C), no bands were observed. This can be explained by the decreased activity of the enzymes at lower temperatures and enzyme denaturation at higher temperatures, which result in inefficient amplification and the absence of bands on the agarose gel. From this result, we conclude that our implementation of a PWM controller regulated and controlled the temperature of the measurement head sufficiently, as the bands were observed at

optimal temperature range of RPA (37 °C and 38 °C), while no bands were observed at low and high temperatures.

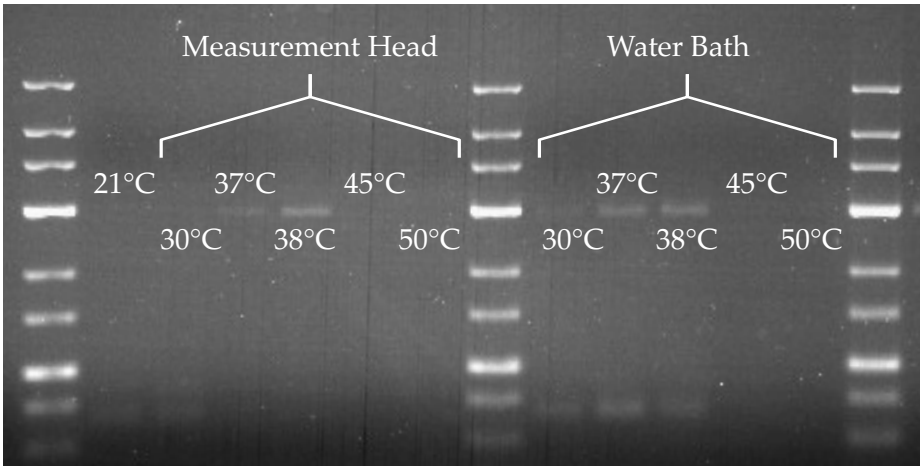

Figure 6.4: Gel image of RPA inside measurement head and water bath at different incubation temperatures. Adopted and modified from [59].

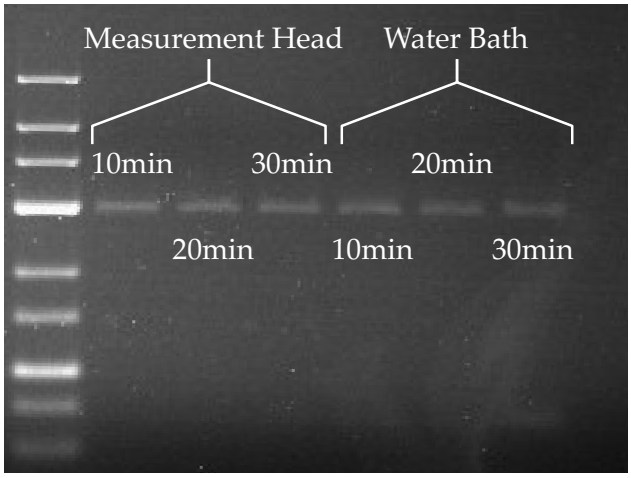

Figure 6.5: Gel image of RPA inside measurement head and water bath at different incubation times. Adopted and modified from [59].

To validate the temperature stability at the sample position in terms of the amplification performance, we performed RPA at different incubation times ranging from 10 to 30 minutes. Similar to previous investigations, the amplification was executed inside our measurement head and in a water bath at 38 °C. After the amplification, the amplified products were purified and loaded into the gel for 1 hour. As shown in figure 6.5, the band intensities for the RPA products amplified inside the measurement head and water bath were similar at all incubation times. This confirms that the stability of the temperature

controlled by PWM inside the measurement head and the water bath control performance are alike in terms of their potential for successful RPA.

6.4 Linear Extrapolation Model

After evaluating the PWM control approach and proving feasibility of RPA in the MH unit, we want to examine the applicability of RPA in our portable magnetic reader device.

Based on the previously presented results, the requirements for a successful RPA in the measurement head were defined as:

1. The controlled temperature at the sample position must not exceed 42 °C in any case, as amplification components may denature.
2. The PWM controller reached a temperature stability error of less than 0.3% at the sample position. With the successfully executed RPA presented in this section, this stability is exceedingly sufficient.
3. A maximum control error of ±1 °C was stipulated at the sample position, as the RPA worked well at 37 °C and 38 °C.

To first examine the applicability of RPA in the MH in a smaller ambient temperature working range 16 °C − 23 °C, a linear extrapolation model may suffice. Starting point for linear extrapolation is the T_s/T_f-relation curve, shown in figure 6.3 E. Similarly, curves for other ambient conditions were derived from figure 6.3 A,B and D.

While the slopes of the linear regression of the T_s/T_f-relation curves only change marginally for all investigated ambient conditions (see equations in figure 6.6), the T_s-axis intercept seems to linearly depend on the ambient temperature level. For this model, we assume that this linear dependency persists for arbitrary but steady ambient temperature values. Therefore, linear extrapolation can be performed, estimating T_s/T_f-relation curves for different steady ambient temperature levels. Due to the negligibly small slope changes, we averaged the slopes of heating and cooling curves, respectively. This slope can be kept for all predicted T_s/T_f-relation curves. The underlying linear relation between the y-axis intercept and ambient temperature can be described for the heating process by $T_{s,intercept,h} = 0.2T_{f,h} - 1.85$ and for the cooling process by $T_{s,intercept,c} = 0.15T_{f,c} - 0.08$, which was obtained by mapping the intercept value versus the ambient condition and fitting a linear function. To test the extrapolation approach, datasets for 16 °C, 18 °C and 21 °C were considered and the *'calibration curve'* data for 23 °C ambient temperature was estimated using the model. Subsequently, we compared the data estimated by the model to the measured data points. The real intercept of the measured data was 2.74, while the predicted intercept with the linear extrapolation model was 3.12. For this data sample, the measured data matches the predicted data with a R^2 value of 0.96 and a SEE of 0.79 °C. With the requirements for a successful RPA in the MH defined earlier, the estimation error in our model should be < 0.89 °C, taking into account the maximum control fluctuation of 0.11 °C at the sample position. Hence, these statistical metrics confirm that an accurate enough prediction is indeed possible relative to the measured data in the proposed steady state ambient temperature range.

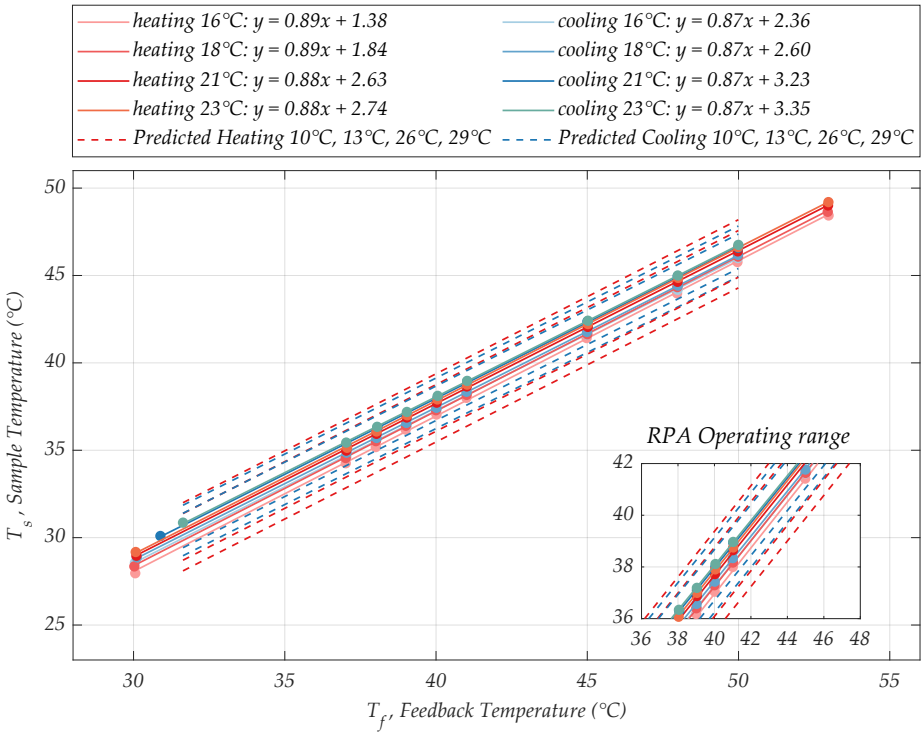

Figure 6.6: Linear heat-up and cool-down relationship of T_s and T_f at 16 °C, 18 °C, 21 °C and 23 °C ambient temperature. The same linear relation is zoomed in (plot inset) to the region of RPA operating temperatures with linear model-estimated calibration curves for 10 °C, 13 °C, 26 °C and 29 °C ambient temperature. Adopted and modified from [59].

Therefore, combining the PWM approach and FMMD technology with this linear regression model provide a simple, yet functional way to control the temperature for sample pre-processing. Moreover, the magnetization response of a magnetic nanoparticle-based immunoassay or DNA assay can potentially even be recorded simultaneously to temperature regulation, during the "on-time" of the duty cycle. While PWM and the linear regression model already meet all necessary requirements for RPA in the investigated environment and while stability errors being small for the presented data, the main limitation of the model is its steady state assumption for ambient temperature conditions around room temperature. Estimating error margins for predicted calibration curves turns out statistically insignificant without testing the control approach in many different environmental conditions first.

6.5 Model for Regulated Sample Position Temperature Simulation

To overcome the steady state assumption of the extrapolation model, we postulate that the LPM structure introduced in chapter 5 in section 5.1.4 can generally be utilized as a multi purpose linearized model. The model output, based on which the model parameters

are identified cannot only be used to describe the LF coil temperature. It is additionally possible to apply the same model structure to describe the temperature at the sample position of the MH, as the model inputs remain similar and the output just needs to be scaled by a delay time term in case of the sample position temperature description. Typically, transport delays occur as nonlinear elements in a first instance. Although, the sample position temperature model is consequentially time-delayed to the LF coil temperature model, hence nonlinear, both models remain linear relative to the T_{AMB} and $\overline{P_{LF}}$ inputs. The scaled transport-delayed temperature output at the sample position can therefore be considered as an output on the LF coil surface. Linearization of the delay time, which could classically be done by Padé approximations, can be omitted for now, which reduces the number of parameters in the model and makes simulations faster.

Model Parameters	**LPM LF Coil**	**LPM Sample Pos.**
K_{LF}	0.302	0.317
K_{AMB}	0.052	0.046
C_{vol}	36.266	45.572
$a_0 - a_5$	[1.103, 1.279, 0.001, 1.145, 1.139, 1.000]	[1.142, 1.305, 0.001, 1.048, 1.165, 1.000]
b_1, b_2, b_4, b_5	[0.737, 1.011, 0.877, 0.980]	[0.730, 1.011, 0.870, 0.980]
$c_0 - c_5$	[0.892, 0.999, 0.999, 0.839, 0.996, 1.018]	[0.806, 0.998, 0.999, 0.864, 0.995, 1.018]
d_1, d_2, d_4, d_5	[1.007, 1.007, 0.987, 0.997]	[1.010, 1.007, 0.988, 0.997]

Table 6.1: Estimated model parameters for LPM at feedback and sample position [59].

Metrics	$T_{f,\mathbf{pred}}$ **Identification/ Validation**	$T_{s,\mathbf{pred}}$ **Identification/ Validation**
NRMSE	0.049 / 0.075	0.047 / 0.066
%—Fit based on R^2_{adj}	96.91% / 96.04%	95.28% / 93.45%
SEE	1.523 / 1.600	1.693 / 2.257

Table 6.2: Statistical measures to evaluate the simulation quality based on measured data [59].

In other words, by adding a further conjecture to the list of assumptions in section 5.1.1 of chapter 5, namely:

- At the sample position, the system obeys a transport delay term that describes the time the heat needs to travel from the sensor to the sample position,

we can built a closely associated model structure design that can mimic the sample position temperature behavior. The parameters for the corresponding parts of the model are listed in table 6.1. The statistical metrics selected in 5.1.3 or [59], respectively, that represent the model performance, are collected in table 6.2.

For additional information, please refer to chapter 5 or to the peer-reviewed article [59].

6.5.1 Delay Time Estimation

While the temperature change, measured on the LF coil surface can be considered to be instantaneous, the temperature at the sample position is a time-delayed version of it. This is due to a nearly thermally insulating air gap between the sample holder and the coil structures, which slows down the temperature propagation to the sample. Therefore, the long transport delay time between the LF coil and the sample position was estimated to be $\tau_d = 48.27$s. It was determined at what time measured temperature data first exceeded $3\times$ the standard deviation of a linear regression line fitted to the initial linear data of the identification and validation datasets. To illustrate this more clearly, an example of a delay-time estimation based on the validation dataset of the sample position model can be found in figure 6.7.

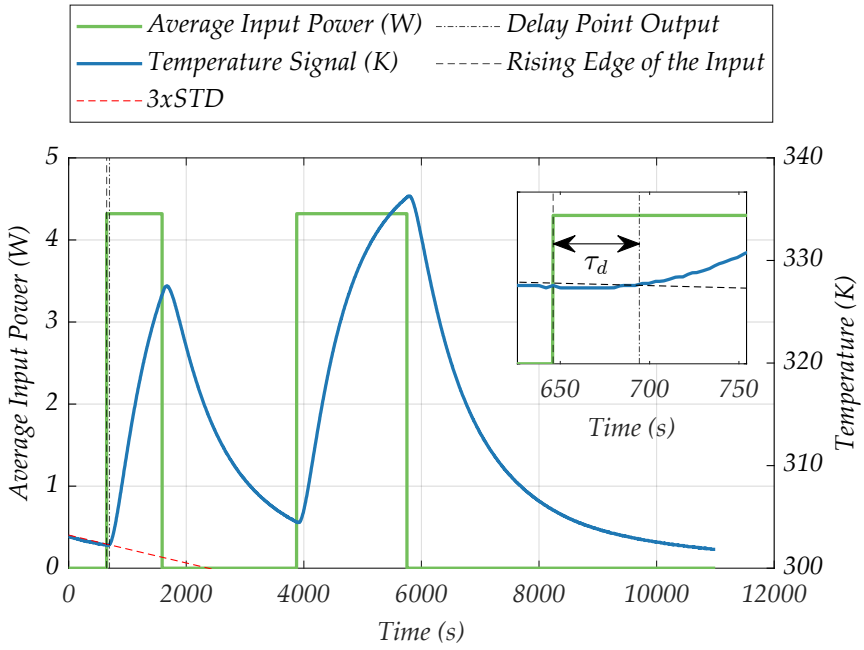

Figure 6.7: Delay time estimation for the sample position LPM. The red line indicates a slope-adjusted regression line at three times the standard deviation of the initial piece of the measured dataset. The green curve indicates the average input power to the system that causes the temperature output behavior (blue curve). Adopted and modified from [59].

6.5.2 Combined Lumped Parameter Model System

Finally, the last step was to connect the model structures of the LPM for $T_{f,pred}$ and $T_{s,pred}$ by using the controlled P_{LF} output of any controller (here, PWM as an example), generated based on the temperature feedback from the LF coil surface and feed it to both LPMs as the controllable input (see figure 6.8). The T_{AMB} input is also similar in this case for both models.

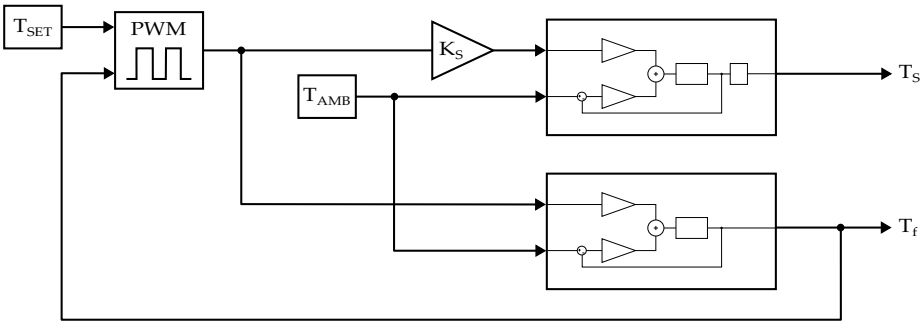

Figure 6.8: Combined model system block diagram with PWM controlled average power input, T_{SET} the desired control temperature and K_S a scaling factor for the control action at the sample position [59].

Doing this, the connected model presents the simulated control output for both the feedback position temperature $T_{f,pred}$ and the sample position temperature $T_{s,pred}$ (figure 6.9), exemplarily for 38 °C, a typical RPA operating temperature. The initial condition fed to the integrator of the models need to be distinct in this case — the LPM for feedback position uses the initial value of the feedback temperature and the LPM for sample position uses the temperature at the sample position at the start of the measurement. As was observed in the measured data, the temperature control at the sample position is a delayed and scaled version of the temperature at the LF coil surface. By introducing a simple scaling factor K_s to the input of the sample position model, we are able to predict these temperature curves at different MH positions for arbitrary ambient inputs. We propose that this enables the selection of sensible control approaches, depending on the severeness of ambient conditions in the field, and to further identify physical limitations for biological use cases.

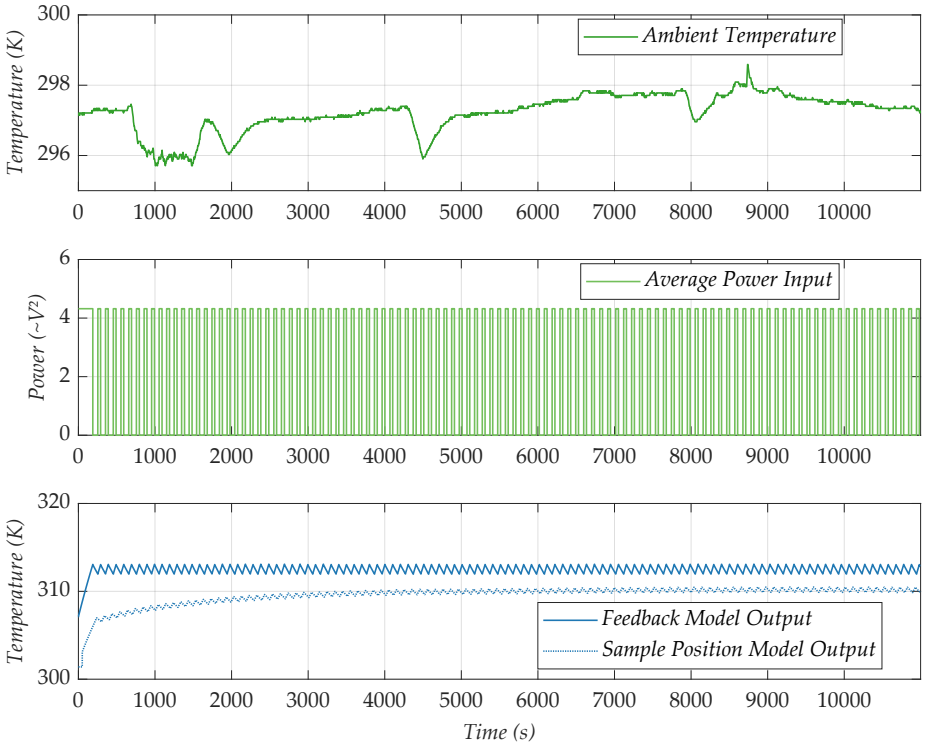

Figure 6.9: Ambient temperature input profile (top), duty cycle of the average power input (mid) and controlled temperature at the feedback position (blue) and sample position (purple) (bottom).

6.6 Remarks and Outlook for the Sample Position Temperature Prediction

The feasibility of performing RPA in the measurement head of the magnetic reader device prior to FMMD signal acquisition at continuously constant ambient conditions has been presented using a PWM approach with the inherently generated heat from the LF excitation coil of the system. This simple implementation has already proven to be a valuable addition to the mobile functionality of the FMMD device for the RPA based sample preparation. A linear relation of the sample temperature to the temperature at the position of the feedback sensor determined the necessary control temperature to set. Despite the sample opening in the MH, a level-shift in the ambient conditions lead to a shift of the T_s/T_f-relation curve towards the new ambient temperature state (figure 6.6). While the feedback temperature T_f stayed constant (as it is embedded within the MH and isolated from the environment), the sample position temperature shifted slightly for temperatures between $16\,°C - 23\,°C$. To investigate the reliability of the PWM approach at ambient conditions different from the tested ones, a linear regression model for prediction of the steady state and a LPM for prediction of the transient behavior of the temperature at the sample position for arbitrary ambient condition inputs was suggested.

Conclusions and Outlook

In this work, the influences of temperature on different aspects of the FMMD response were evaluated. It was assessed, whether the ambient conditions, the thermal behavior of the LF coil in the sensory unit and the sample temperature, influence, excitation signal generation or FMMD signal acquisition by any means. This work further tested simple control approaches, discussed its drawbacks and usability and suggested a computational, model-based strategy to assess thermal and electrical behavior of the MH with the aim to find input power shapes that provide minimal measurement duration and maximum thermal stability.

Notable drift in LF and offset magnetic excitation voltage amplitudes pointed towards strong local Joule heating effects in the excitation coils of the mobile magnetic reader. FMMD measurements of different MNP and MIAs suggested that the (sensor)temperature-to-(FMMD) signal dependency alters based on particle type and ambient temperature level (the temperature the sample is exposed to prior to insertion into the MH). In other words, to some extent the FMMD signal is modulated by thermal effects. A computational and fast way to reveal thermal behavior of the MH for arbitrary electrical input- and ambient temperature shapes is a transient LPM framework. With our model, it is now feasible to identify candidate measurement inputs for optimal thermal and electrical performance in terms of fluctuation in the FMMD readout and measurement duration for various input powers of lower frequencies. In combination with a parametric finite element COMSOL model of the MH, this framework will also support future sensor unit designs and investigation of its electrical and thermal properties.

For faster changing input powers, the model parameters are more difficult to identify. HF and LF coils are in close contact to one another in the current MH design. Therefore, the HF amplitude is also altered upon Joule heating. To improve the LPM framework, a next step could be to extend it for a high frequency input power, that is also connected to the resistance feedback of the LF coil. Model extension, or implementation of Padé approximations (discussed in chapter 5) into the input paths of the resistance feedback model, may help to achieve higher frequency input validity.

Further, we expect that upon connection of the thermal LPM to a transformer model of the miniaturized induction coil system in the MH, the developed framework offers a novel approach to computationally examine the FMMD signal behavior under different input and ambient conditions, but also for different magnetization curves and particle behaviors. The COMSOL model furthermore allows for designing a portable heat exchanger to regulate the sample temperature independent of the coil temperature. In future, we can also computationally estimate solar irradiation for the sensor and sample behavior and therefore its effects on the FMMD signal in PoC applications.

We examined the impact of ambient temperature on the induction-based recording of magnetic signals in MIAs. Our data are based on the measurement of FMMD signals in artificially generated surrounding conditions. This was achieved either by heat gun application or in temperature regulated cell-culturing rooms. Some inconsistent results were obtained, therefore field experiments would be beneficial or alternatively feeding the developed model with temperature profiles recorded during a practical in-field test.

In the scope of this work, we also implemented a thermal control approach and proved feasibility of RPA in the MH with the possibility of simultaneous signal acquisition (chapter 6). This could be the first step towards online reaction kinetics measurements for labeled assays. To achieve this, the simultaneous acquisition of real-time DNA amplification FMMD signal and the invention of data post-processing tools to extract kinetics information from these data are important in the future.

We tested the feasibility of RPA using positive control templates which typically consist of very 'clean', high quality DNA. In-field samples, especially waste water may be contaminated by ribonucleic acid (RNA) snippets or additional proteins that can strongly influence the amplification efficiency. This should be tested in future iterations. Further, each organism's DNA to be amplified will require appropriate primer design.

If time is not a critical factor, the FMMD method could also be used as a test for hazard classification based on secondary analytes. Sensitivity could later be assessed not relative to the colony-forming units required in, for example, drinking water regulations, but rather in relation to the detection of specific metabolic products or toxin concentrations of pathogens. Based on the type of toxins or metabolites involved, the corresponding pathogenic (e.g., E. coli) stain can often be identified. Possible subsequent steps could include combinations with next-generation DNA sequencing for bacterial identification or cell culture cultivation for further verification. Besides, FMMD could find application in the quality control of magnetic nanoparticle production and size distribution determination, providing a very cheap alternative to more common procedures.

Appendix A

Deformation of Sine

In chapter 3 the necessity of preventing intermodulation frequencies due to LF signal deformation was discussed thoroughly. Figure A.1 shows an oscilloscope snapshot from the deformed LF sine wave, measured at the LF output test point. THe deformation was observed when applying a magnetic DC offset field through the LF coil, while also applying the standard LF excitation. The total voltage extended the possible supply voltage. Further thermal drift or poorly adjusted potentiometers in the excitation signal generation chain can cause this variations and must be prevented.

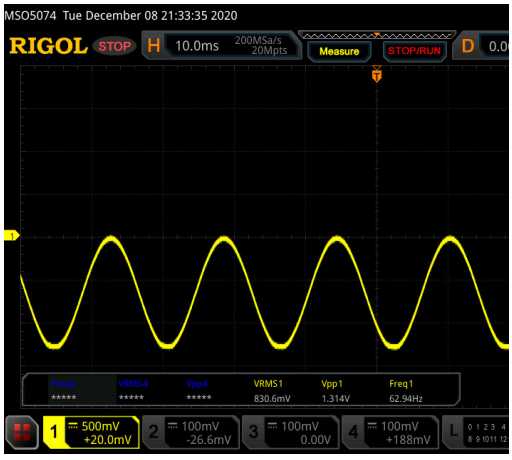

Figure A.1: Digital Oscilloscope snapshot with a deformed LF excitation sine wave, measured at TP11 (test point for low frequency output to the MH). The sine wave flattens at the lower peaks.

Appendix B

GUI and Measurement Process

Typically, the operators of the suggested mobile magnetic reader device are lab technicians who are familiar with established water analysis methods such as the IDEXX [11] system or volunteers in the respective organization. It cannot be assumed that they have any experience in operating a magnetic reader device. Therefore it is necessary to guide the operators through the measurement procedure by clear instructions and information.

In collaboration with the German civil and disaster protection organization THW, a simple measurement GUI and process was framed according to the request of untrained personnel that will later operate the magnetic reader device to quickly evaluate contaminants in drinking water in a crisis situation.

The measurement procedure to follow, indicated on the device's Nextion display is described in the following figure B.1. The Display layout and texts were designed using the Nextion Editor software.

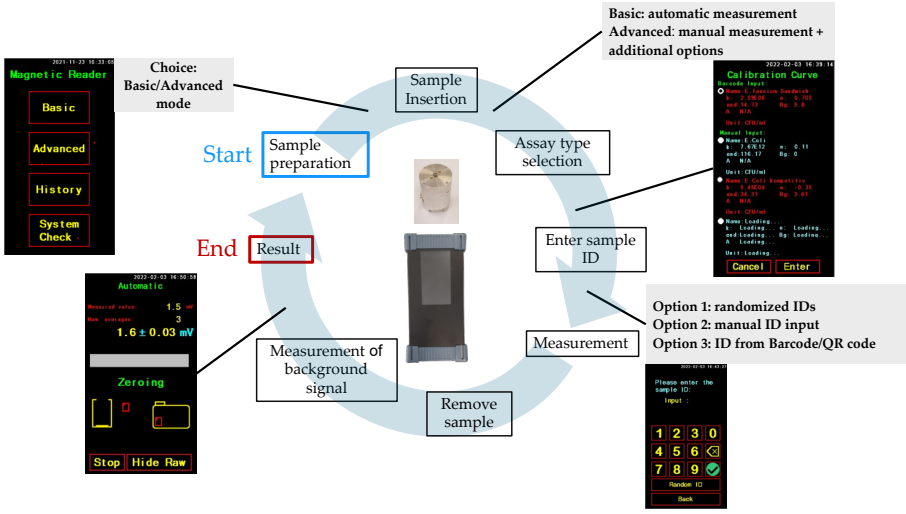

Figure B.1: Schematic of the measurement process with the 2020 version of the mobile magnetic reader. Snapshots of the measurement interface are shown.

Appendix C

Measurement Head Geometry

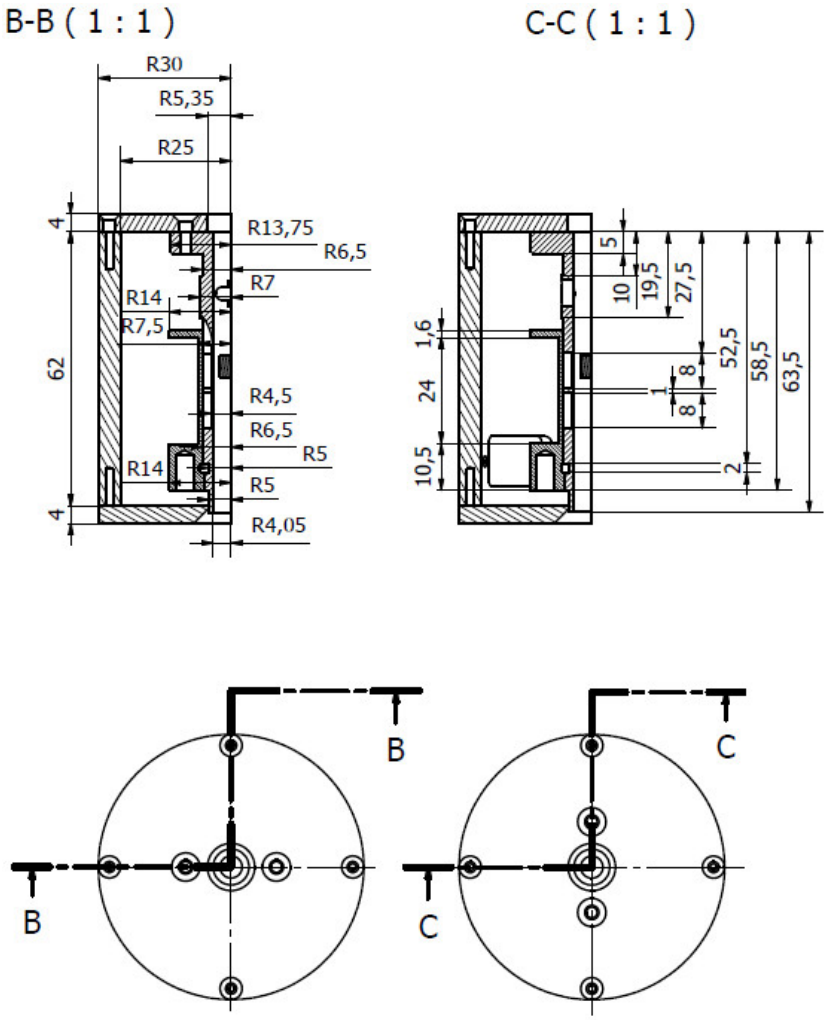

Figure C.1: Two sectional views B and C with rectangular cutting paths through the measurement head cylinder at different rotational orientations of the cylinder.

Appendix D

Mathematical Temperature Correction Algorithm

In the course of this project, one of the earlier attempts to correct the measured FMMD signal for its changes with temperature was a temperature correction algorithm. The algorithm was fundamentally based on the assumption of a purely linear dependence of the FMMD signal on temperature measurement data. The aim was, to calculate the FMMD signal at a certain reference temperature T_R (e.g. lab temperature) based on the signal and temperature measured at the time of recording.

This purely mathematical correction essentially consists of a function that correlates the FMMD signal $S(t)$ with the temperature change in the measurement head, using a proportionality constant α. Subsequently, the signal is weighted depending on the temperature at which the respective signal was recorded.

Generally both, FMMD signal and temperature measurement data follow the form:

$$S(t) = S_0 + \Delta S \left(1 - e^{-\frac{(t-t_0)}{\tau}}\right) \tag{D.1}$$

$$T(t) = T_0 + \Delta T \left(1 - e^{-\frac{(t-t_0)}{\tau}}\right) \tag{D.2}$$

with S_0 and T_0 as the initial signal and temperature values. The exponential expression well describes the typical shape of the measured data. In a physic context, τ shows how quickly the temperature and signal change with time, respectively. The assumption of linearity between signal and temperature is given as:

$$S(T) = T_{S_{T_0}} \cdot (1 + \beta \Delta T) \tag{D.3}$$

For this to hold true, τ needs to be approximately equal for the recorded FMMD signal and recorded temperature data. In this case, τ is a reader-dependent parameter, meaning it is different for each device. However, it should not be different for the acquired temperature data and FMMD signal, when the respective data are measured using the same device.

β indicates how strongly the signal for a specific particle changes with temperature. In other words, β is a particle-dependent parameter.

$$\overline{\Delta S} = \sum_{i=1}^{n} [S(t_i) - S(t_0)] \cdot \frac{1}{\sum_{i=1}^{n} \left[1 - e^{\frac{t_i - t_0}{\tau}}\right]} \tag{D.4}$$

$$\overline{\Delta T} = \sum_{i=1}^{n} [T(t_i) - T(t_0)] \cdot \frac{1}{\sum_{i=1}^{n} \left[1 - e^{\frac{t_i - t_0}{\tau}}\right]} \tag{D.5}$$

For higher temperatures, the correction of the FMMD signal needs to be weighted more strongly. Therefore, weighting was applied to the signal and temperature as the inverse of its behavior at each point in time.

The signal at a certain reference temperature can then be calculated by equation D.6.

$$S(T_R) = \frac{S_0 + \overline{\Delta S}}{1 + \beta(T_0 + \overline{\Delta T} - T_R)} \tag{D.6}$$

A major advantage of the mathematical correction in practical applications is that it is easy to implement and can be applied instantly when the device is switched on. As a result, the previously required warm-up phase for capturing the measurement signal is no longer necessary. However, this solution does not address the actual changes in coil wire resistances and thus does not prevent excitation signal deformation. Additionally, from collected data it is unclear, if a linear dependency, e.g. a similar time constant τ for temperature and signal, is always present (see E). Furthermore, the relation of ambient and MH temperature should be well-known to ensure a sufficiently accurate signal correction independent of ambient conditions. But up to date it is not evident, that we observe a correlation, independent on the sample used. Last but not least, it should be applicable to offset-adjusted measurements or measurement schemes with different low frequency amplitude values in sequence. For these reasons, this approach was abandoned later in this project [60].

Appendix E

FMMD Signal and Temperature Time Constant Investigation

In order for the temperature correction algorithm in D to be valid independent of the measurement condition, the requirement is the similarity of temperature and signal time constants. Otherwise, the assumption of proportionality between temperature and signal may not hold true for all cases.

A priori to some of the herein discussed topics, the group of magnetic sensors has collected many measurements of temperature and FMMD signals in lab conditions using a custom laboratory setup ([94], [96]). The offset-scans in these measurements required a piecewise increasing DC offset voltage of an external EM. After the acquisition of the signal at a particular offset field, the sample was taken out of the MH and put back in again when cooled to ambient temperature. However, without a particular thermal regulation each consecutive offset step, increased the temperature during the measurement process further. For each increase in temperature, an increase in signal was observed. Contrary, if the sample was taken out, the MH cooled down a bit.

In the data analysis, we attempted to match time constants of MH temperature behavior and FMMD signal behavior, by manual fitting. Equation E.1 was utilized to determine the time constants of the ca. 50 taken measurements at different offset-field *'heating conditions'*. For the FMMD signals the respective formula was used, replacing temperature with signal.

$$T(t) = \alpha \cdot \left(1 - e^{\frac{t_0 - t}{\tau}}\right) \tag{E.1}$$

α is the amplitude of temperature or FMMD signal. t_0 is the starting point of the measurement and the time constant τ of the system is the time needed to reach $1 - \frac{1}{e}$ of the maximum amplitude for an increasing exponential function.

The sum of squared differences was used to compare the measured data to the fitting curve. differential evolution (DE) was then utilized to minimize the error and find an initial parameter guess. DE helps to avoid local minima in the solution and the parameter guess allows us to apply Levenberg-Marquardt (LM) fit refinement.

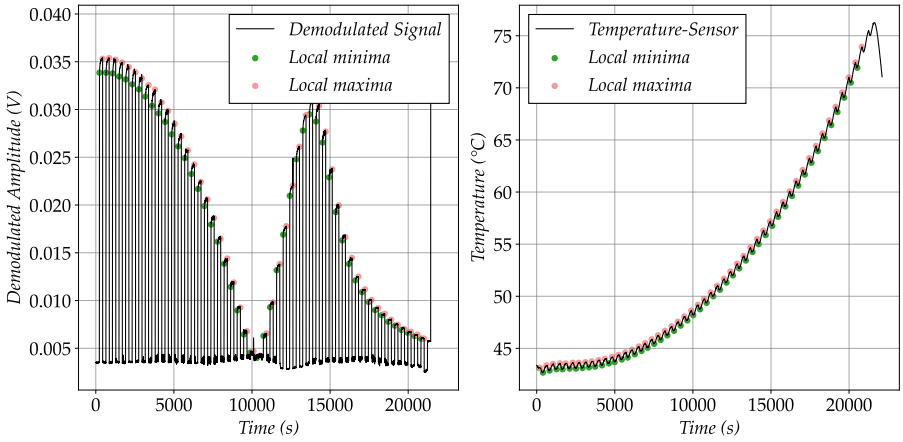

Figure E.1: Demodulated signal amplitude of $f_1 + 2f_2$ during offset scan (left) and corresponding temperature behavior of the MH (right). The local minima and maxima used for fitting are indicated by red and green dots.

Each set of data between a local minima and maxima indication in figure E.1 was used for the described analysis process. Within the FMMD signal time constants, the variance was reasonable with time constants ranging from $\tau = 34$ s to 50s, with an average of 45s, which amounts to a maximum of 32% variation in the cases that were most severe. The amplitudes α were about 1.2mV. However, the corresponding temperature fits varied between $\tau = 120$s and 500s, with an average of 314s and an amplitude of 1.4°C. While these fits could be repeated with measurements that saturate for longer to achieve better fits, part of the target was to feed the correction algorithm with the determined τ values after a short measurement time. This also indicates, that the time constants of heating and signal development behave severely different or it is at least not clear which factors determine a τ match.

Appendix F

Convection Coefficient Estimation

A critical part in developing a model that outputs the heat distribution in a geometry, is to determine the heat transfer coefficients in the system. Specifically, the convective heat transfer coefficient “h” is of interest here, as it determines, how the heat-sink in the system, natural or forced convection, will scale. Usually the average "$\bar{h}$" is estimated theoretically using natural convection correlations with the well-known dimensionless Grasshof, Prandtl and Rayleigh numbers from which the Nusselt number can be calculated for a certain geometry. The Nusselt number is also known as the dimensionless convective heat transfer coefficient and is directly related to the theoretical value of “h”. However, the relation differs, depending on the geometry of the body and the flow conditions (laminar/turbulent/mixed) of the surrounding medium at its surface. Further, having a coefficient, directly related to the heat dissipation in the system, is also helpful to estimate the validity of lumped parameter approximations by utilizing the Biot number.

The following equations and relations were taken from [107].

F.1 Theoretical Dimensionless Number Correlations of the Convection Coefficient

In the following, the theoretical convection coefficient was estimated for two different scenarios. Further, the estimations were carried out in a simplified MH geometry. The estimates can be used to complement the COMSOL simulations and to formally proof wether or not lumped parameter approximations can be applied to the MH system in a thermal context.

Lets call the two considered scenarios A and B. Both estimations do not include top and bottom of the cylinder but for simplification consider an open cylinder (estimation of $\bar{h}$ only for vertical side walls). Scenario A focusses on the convective heat transfer coefficient on the side walls of the aluminum housing of the MH. In Scenario B, the convection coefficient for the copper coil, simplified as a hollow cylinder with a thickness of both, the LF and HF coil structures, will be estimated.

The simplified cylinder geometry consists of the copper coil, assumed as a hollow cylinder inside the aluminum housing of the measurement head. Geometrical measures needed (lengths, diameters and thicknesses) can be extracted from the technical drawings in appendix C. However, all used material constants and parameters are listed below:

$L_{\mathrm{Al}} = 0.070\ m, \quad D_{\mathrm{Al},o} = 0.060\ m \quad D_{\mathrm{Al},i} = 0.050\ m$
$L_{\mathrm{Cu}} = 0.024\ m, \quad D_{\mathrm{Cu},o} = 0.028\ m, \quad D_{\mathrm{Cu},i} = 0.015\ m, \quad t_{\mathrm{Cu}} = 0.0065\ m$
$Gap_{\mathrm{Cu-Al}} = R_{\mathrm{Al},i} - R_{\mathrm{Cu},o} = 0.025\ m - 0.014\ m = 0.011\ m$
$T_\infty = 295\ \mathrm{K}, \quad T_{\mathrm{Al},o} = 315\ \mathrm{K}, \quad T_{\mathrm{coil}} = 330\ \mathrm{K}$
$\Delta T_A = T_{\mathrm{Al},o} - T_\infty = 20\ \mathrm{K},$
$\Delta T_B = T_{\mathrm{coil}} - T_\infty = 35\ \mathrm{K},$
$T_{f,A} = \frac{T_{\mathrm{Al},o}+T_\infty}{2} = 305\ \mathrm{K},$
$T_{f,B} = \frac{T_{\mathrm{coil}}+T_\infty}{2} = 312.5\ \mathrm{K},$
$g = 9.81\ \mathrm{m/s^2},$
$\beta \approx \frac{1}{T_f}$

The kinematic viscosity and thermal diffusivity changes with T_f and hence has slightly different values for the different scenarios.

$\nu_A = 1.63 \times 10^{-5}\ \mathrm{m^2/s},$
$\alpha_A = 2.24 \times 10^{-5}\ \mathrm{m^2/s},$
$Pr_A = \nu_A/\alpha_A \approx 0.728.$
$\nu_B = 1.70 \times 10^{-5}\ \mathrm{m^2/s},$
$\alpha_B = 2.31 \times 10^{-5}\ \mathrm{m^2/s},$
$Pr_B \approx 0.736$

The thermal conductivities of aluminum, copper and air at the respective film temperatures are taken from [118], were checked with reference sources [85], [84], [86] and are listed below.

$k_{\mathrm{Al}} = 205\ \mathrm{W/(m\,K)},$
$k_{\mathrm{Cu}} = 385\ \mathrm{W/(m\,K)},$
$k_{air_{T_{f,A}}} = 0.0261\ \mathrm{W/(m\,K)},$
$k_{air_{T_{f,B}}} = 0.0267\ \mathrm{W/(m\,K)},$

Variations of thermal conductivities of solids at the assumed $T_{f,A,B}$ are small and therefore not considered.

It is important to note, that the bottom and top of the cylinders, copper coil and aluminum housing, respectively, are not negligible for effective convection coefficient estimation and

will indeed change the coefficients. However, since the Biot number is four orders of magnitude smaller then 1, it will not influence the validity of the lumped capacitance approximation regardless.

The calculations follow Nellis and Klein's approach, described in [107].

First the rayleigh number needs to be calculated as a combination of Prandtl and Grashof numbers. It relates the buoyancy forces due to a temperature difference to the dampening effects of viscosity.

$$Ra_L = \frac{g\,\beta\,\Delta T\,L^3}{\nu\,\alpha}. \tag{F.1}$$

$$C_{\text{lam}} = \frac{0.671}{\left[1 + (0.492/Pr)^{9/16}\right]^{4/9}}, \qquad C_{\text{turb}} = \frac{0.13\,Pr^{0.22}}{\left(1 + 0.61\,Pr^{0.81}\right)^{0.42}}. \tag{F.2}$$

The empirical literature correlation numbers originally stem from Churchill and Chu [119]. The same methodology was followed by Nellis and Klein [107] and is also followed here.

$$\bar{Nu}_{\text{lam}} = \frac{2}{\ln\!\left(1 + \dfrac{2}{C_{\text{lam}}\,Ra_L^{1/4}}\right)}, \tag{F.3}$$

$$\bar{Nu}_{\text{turb}} = \frac{C_{\text{turb,V}}\,Ra_L^{1/3}}{1 + 1.4 \times 10^9\,Pr/Ra_L}. \tag{F.4}$$

The combination of laminar and turbulent free convection was taken from [120].

$$\bar{Nu}_{\text{plate}} = \left(\bar{Nu}_{\text{lam}}^{6} + \bar{Nu}_{\text{turb}}^{6}\right)^{1/6}. \tag{F.5}$$

Until now, calculations for vertical plates were used. Therefore, we need to correct for the vertical-cylinder curvature using:

$$\varepsilon = \frac{1.8}{\bar{Nu}_{\text{plate}}}\frac{L}{D}, \tag{F.6}$$

$$\bar{Nu}_{\text{cyl}} = \bar{Nu}_{\text{plate}} \cdot \frac{\varepsilon}{\ln(1+\varepsilon)}. \tag{F.7}$$

Finally the estimation of the average convection coefficient can be calculated for the vertical cylinder side walls in scenario A and B:

$$\boxed{\bar{h}_{A,B} = \frac{k_{A,B}}{L_{A,B}}\,\bar{Nu}_{\text{cyl}}}. \tag{F.8}$$

where $L_{A,B}$ is the length of the cylinders for either scenario.

Result for Scenario A: Aluminum housing → ambient When plugging in the parameters from above (scenario A) into the equations F.1-F.8, we receive:

$$Ra_L \approx 6.04 \times 10^5, \quad \bar{Nu}_{\text{plate}} \approx 15.38, \quad \bar{Nu}_{\text{cyl}} \approx 16.40.$$

$$\boxed{\bar{h}_A \approx 6.12 \text{ W/(m}^2\text{ K)}}.$$

Result for Scenario B: Copper coil → ambient For scenario B, we receive:

$$Ra_L \approx 3.87 \times 10^4, \quad \bar{Nu}_{\text{plate}} \approx 8.21, \quad \bar{Nu}_{\text{cyl}} \approx 8.96.$$

$$\boxed{\bar{h}_B \approx 9.97 \text{ W/(m}^2\text{ K)}}.$$

Both of these exemplarily estimated average convection coefficients result in a Biot number $<< 1$, which formally determines the validity of lumped capacitance approximations (see 5.1.4).

A practical overall uncertainty of ±(20–30)% is reasonable for such estimates [83, 87]. Even for significantly higher error margins, the lumped capacitance approximation in this thesis will stay valid.

Appendix G

COMSOL Simulation Results

In the course of chapter 5, COMSOL simulations were carried out to investigate the coil surface temperature as a multiphysics model result versus a lumped parameter model output for validation. Beyond the coil surface temperature the FEA makes 2D and 3D magnetic field, current density and temperature distribution investigation feasible. The herein presented supplementary data exemplary shows corresponding COMSOL outputs to emphasize its potential for measurement head design and analysis.

All of the COMSOL plots within this supplementary chapter are exemplary for the original measurement scheme shown in figure 5.5A (bright blue color). Figure G.1 specifically, is the equivalent 2D axi symmetric contour plot to the average temperature line plot shown in figure 5.5 B (bright blue color). The black line is the vertical cross-section of a single-layer homogenized multi-turn copper coil. The images G.1 and G.2 can be extended into three dimensions by 360° rotation that turns the black line into a hollow cylinder, representing the coil geometry.

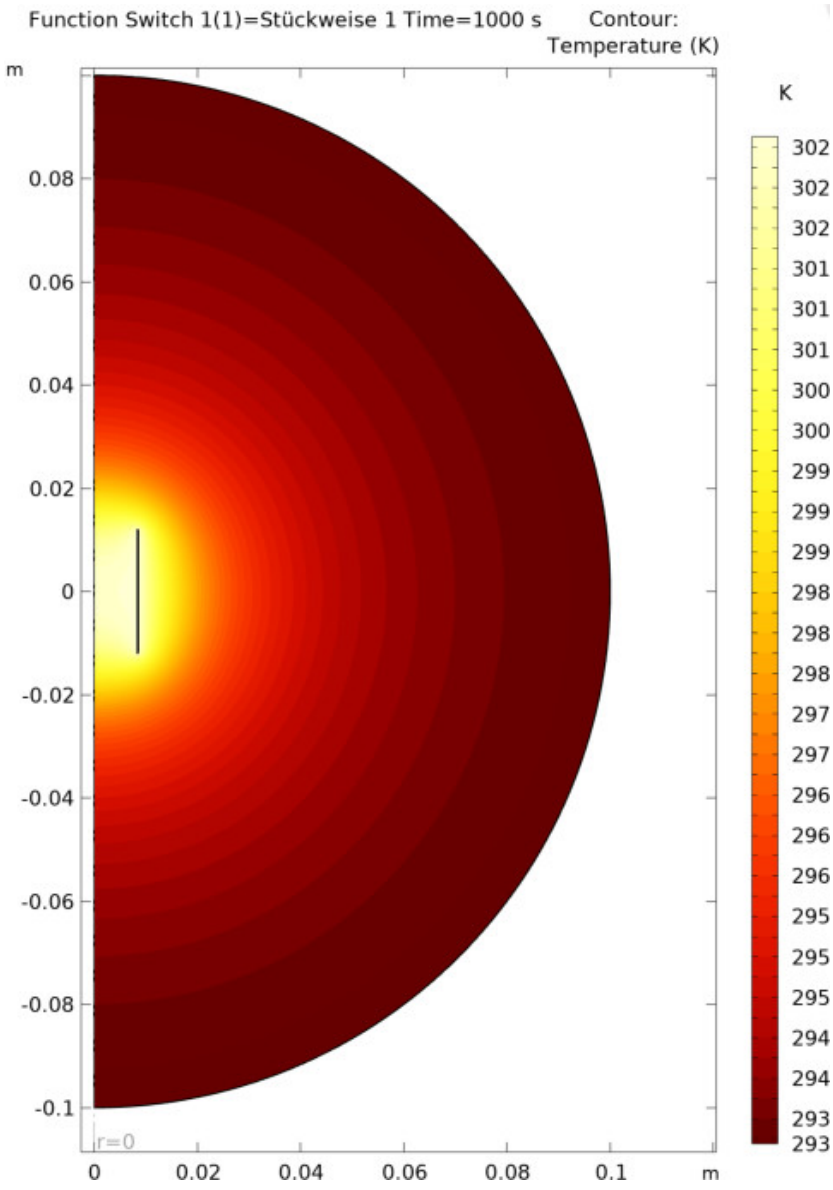

Figure G.1: Exemplary single layer test coil isothermal contours at maximum electrical input current for original monotonously increasing measurement scheme. The screenshot was taken from COMSOL, version 6.2.0.415 simulation panel.

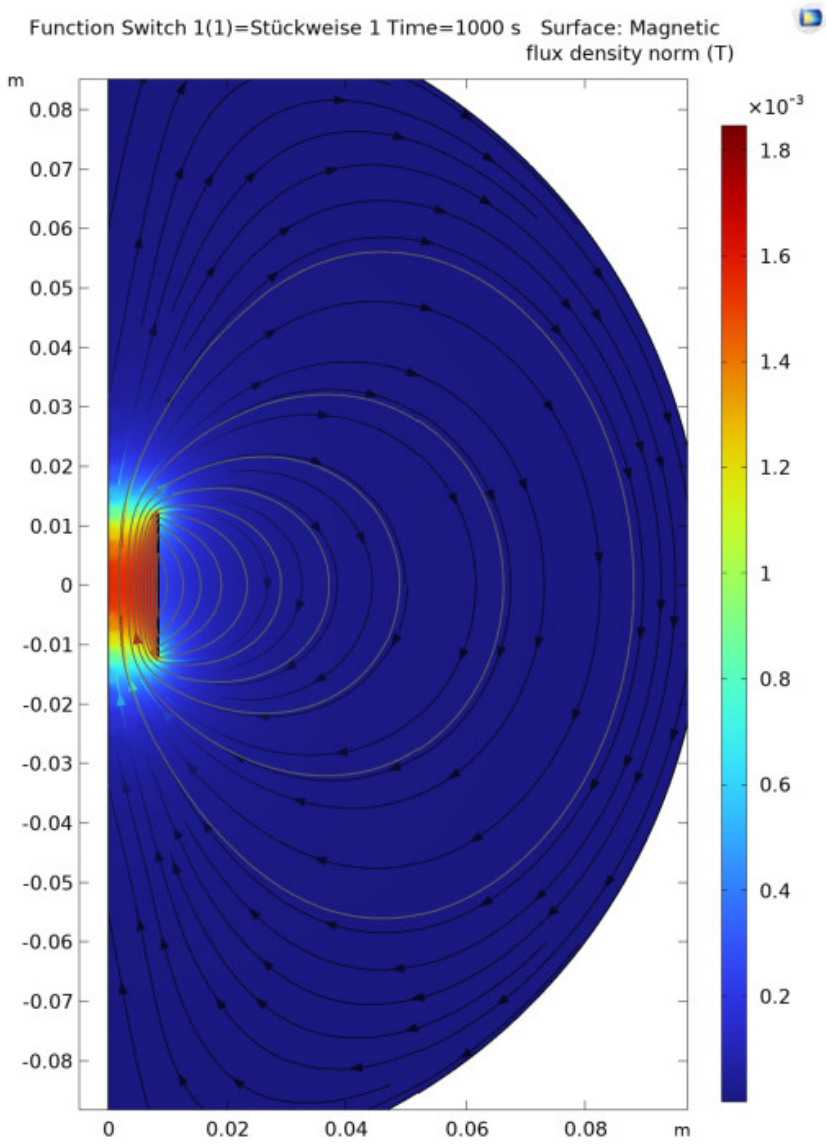

Figure G.2: Exemplary single layer test coil magnetic flux density at maximum electrical input current for original monotonously increasing measurement scheme. The screenshot was taken from COMSOL, version 6.2.0.415 simulation panel.

The FEA in COMSOL was extended from the single layer coil to the complete measurement head structure. Due to long simulation times, this was herein restricted to be performed for a single input measurement scheme. For comparison, the same measurement scheme was used in the exemplary single layer coil problem from figure G.1 and G.2.

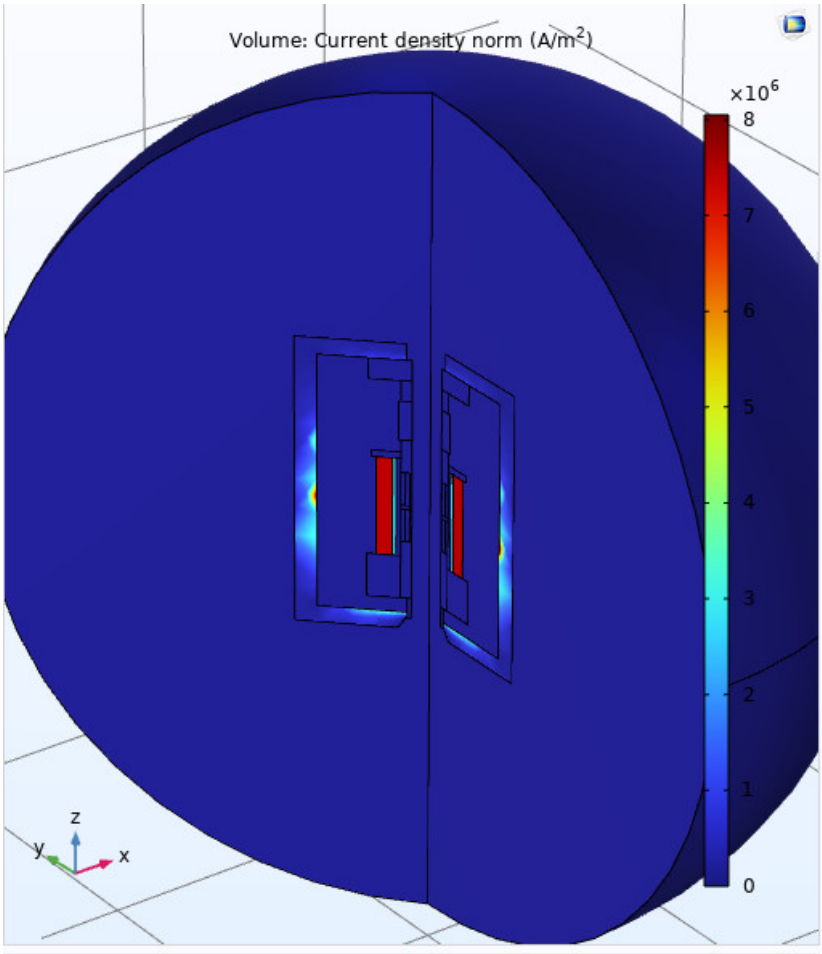

Figure G.3: Exemplary total measurement head current density at maximum electrical input current for original monotonously increasing measurement scheme. Eddy currents in the measurement head housing are indicated. The screenshot was taken from COMSOL, version 6.2.0.415 simulation panel.

From the current density plot in G.3, one can see that a partial source for heating within the measurement head might stem from eddy currents in the aluminum housing of the MH. Further investigation is necessary, to determine its significance.

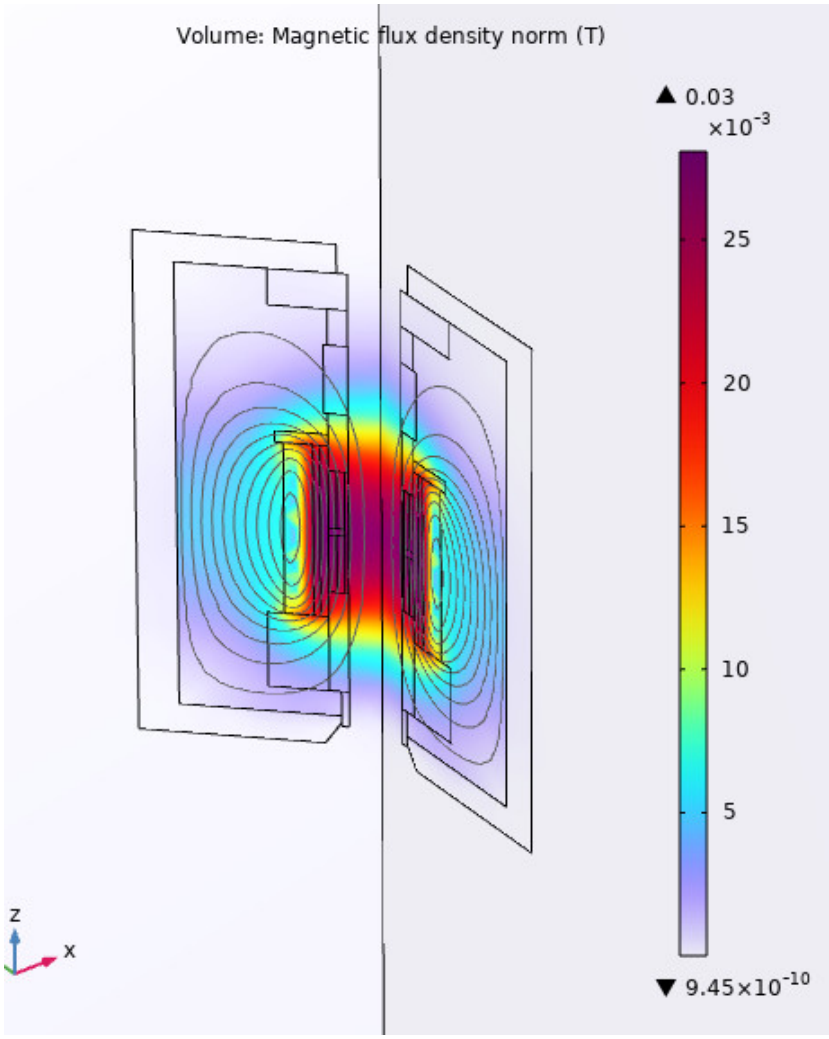

Figure G.4: Exemplary total measurement head magnetic flux distribution at maximum electrical input current for original monotonously increasing measurement scheme. The screenshot was taken from COMSOL, version 6.2.0.415 simulation panel.

Maximum magnetic field strengths of 25 mT agree well with the achieved maximum field amplitudes that were experimentally determined using Hall sensor measurements. In the simulation, the maximum applied electrical current was 300 mA, while the Hall sensor measurements were performed for an older MH with a maximum coil current of 240 mA. Therefore the magnetic field values are slightly higher in the COMSOL output, compared to the values shown in section 3.2, figure 3.4.

Appendix H

Mobile Power Supply

The magnetic reader needs a voltage supply of ±15 V. Multiple power source options can be utilized mobily, due to the integration of a DC/DC Converter into the mobile version of the magnetic reader. The TRACO POWER TEN 20-2423WIN DC/DC Converter features a wide input voltage range of $9 - 36$ V. Therefore, it is possible to connect it to either a 12 V car battery or a 24 V truck battery. Further Pb-gel batteries or different types of commercially available drill machine batteries can be used for mobile power supply.

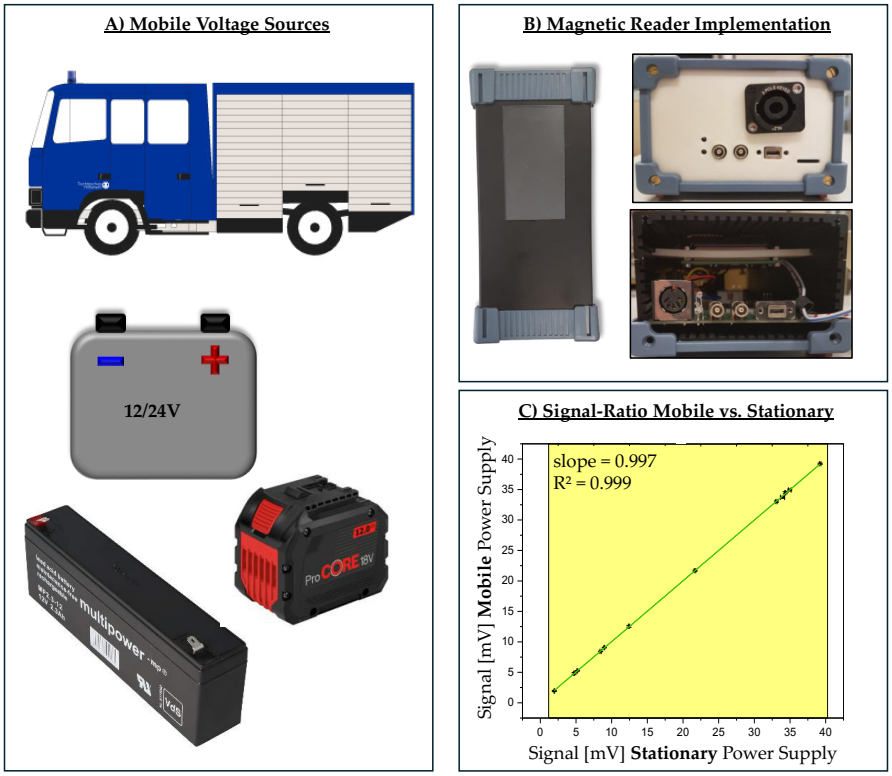

Figure H.1: THW emergency vehicles and exemplary Battery types (A) that can be connected to a magnetic reader integrated TRACO POWER DC/DC Converter of the 20WIN series (B) via a ICE certified NL2FX 2-pole plug (female connector in figure B). In C) the signal differences between stationary and mobile usage was tested for a series of synomag 70 nm magnetic particles.

Appendix I

Temperature during Offset Excitation Amplitude Investigation

During the Hall sensor offset field scans to determine the magnetic field amplitude behavior applied by the electrical excitation currents in the mobile version of the magnetic reader in section 3.3, the temperature of the MH was also recorded. Exemplary temperature recordings at settings of LF1000 and LF500 can be found in figure I.1.

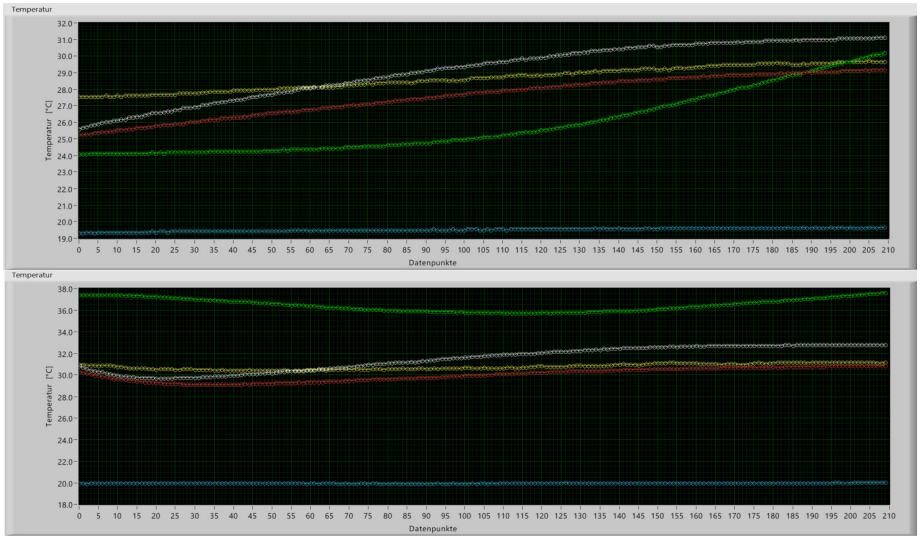

Figure I.1: Screen shots of temperature recordings in the MH (green graph) of the magnetic reader during offset scans with settings of LF500 and LF1000. A National Instruments DAQ and a custom LabView Software were used for data acquisition. The white, yellow and red graphs are recorded at different locations on the magnetic reader PCB. The blue graph indicates the temperature outside of the magnetic reader.

Due to the lower temperatures at around $24 - 30\,°C$, the amplitudes at theLF500 settings were higher compared to the amplitudes at higher MH temperature recordings as for example for settings of LF1000 with around $37\,°C$.

Bibliography

[1] N. Nwachcuku and C. P. Gerba, "Emerging waterborne pathogens: Can we kill them all?", *Current Opinion in Biotechnology*, vol. 15, no. 3, pp. 175–180, Jun. 2004, ISSN: 09581669. DOI: 10.1016/j.copbio.2004.04.010 Accessed: Jun. 2, 2025. [Online]. Available: https://linkinghub.elsevier.com/retrieve/pii/S095816690400062X

[2] G. Bitton, *Microbiology of Drinking Water: Production and Distribution*, 1st ed. Wiley, Dec. 2014, ISBN: 978-1-118-74392-8. DOI: 10.1002/9781118743942 Accessed: Jun. 2, 2025. [Online]. Available: https://onlinelibrary.wiley.com/doi/book/10.1002/9781118743942

[3] F. Y. Ramírez-Castillo et al., "Waterborne pathogens: Detection methods and challenges", *Pathogens (Basel, Switzerland)*, vol. 4, no. 2, pp. 307–334, May 2015, ISSN: 2076-0817. DOI: 10.3390/pathogens4020307

[4] S. A. Collier et al., "Estimate of Burden and Direct Healthcare Cost of Infectious Waterborne Disease in the United States", *Emerging Infectious Diseases*, vol. 27, no. 1, pp. 140–149, Jan. 2021, ISSN: 1080-6059. DOI: 10.3201/eid2701.190676

[5] M. S. Horwitz, L. M. Bradley, J. Harbertson, T. Krahl, J. Lee, and N. Sarvennick, "Diabetes induced by Coxsackie virus: Initiation by bystander damage and not molecular mimicry", *Nature Medicine*, vol. 4, no. 7, pp. 781–785, Jul. 1998, ISSN: 1078-8956, 1546-170X. DOI: 10.1038/nm0798-781 Accessed: Jun. 2, 2025. [Online]. Available: https://www.nature.com/articles/nm0798-781

[6] M. Roivainen et al., "Mechanisms of Coxsackievirus-Induced Damage to Human Pancreatic β -Cells[1]", *The Journal of Clinical Endocrinology & Metabolism*, vol. 85, no. 1, pp. 432–440, Jan. 2000, ISSN: 0021-972X, 1945-7197. DOI: 10.1210/jcem.85.1.6306 Accessed: Jun. 2, 2025. [Online]. Available: https://academic.oup.com/jcem/article-lookup/doi/10.1210/jcem.85.1.6306

[7] H. P. Endtz et al., "Molecular Characterization of *Campylobacter jejuni* from Patients with Guillain-Barré and Miller Fisher Syndromes", *Journal of Clinical Microbiology*, vol. 38, no. 6, pp. 2297–2301, Jun. 2000, ISSN: 0095-1137, 1098-660X. DOI: 10.1128/JCM.38.6.2297-2301.2000 Accessed: Jun. 2, 2025. [Online]. Available: https://journals.asm.org/doi/10.1128/JCM.38.6.2297-2301.2000

[8] C. Wilson, H. Tiwana, and A. Ebringer, "Molecular mimicry between HLA-DR alleles associated with rheumatoid arthritis and as the aetiological basis for autoimmunity", *Microbes and Infection*, vol. 2, no. 12, pp. 1489–1496, Oct. 2000, ISSN: 12864579. DOI: 10.1016/S1286-4579(00)01303-4 Accessed: Jun. 2, 2025. [Online]. Available: https://linkinghub.elsevier.com/retrieve/pii/S1286457900013034

[9] N. Uemura et al., "*Helicobacter pylori* Infection and the Development of Gastric Cancer", *New England Journal of Medicine*, vol. 345, no. 11, pp. 784–789, Sep. 2001, ISSN: 0028-4793, 1533-4406. DOI: 10.1056/NEJMoa001999 Accessed: Jun. 2, 2025. [Online]. Available: http://www.nejm.org/doi/abs/10.1056/NEJMoa001999

[10] Technisches Hilfswerk. "Bundesanstalt technisches hilfswerk". Accessed: 2025-06-03. [Online]. Available: https://www.thw.de/DE/Startseite/startseite_node.html

[11] IDEXX Laboratories. "Tecta® water microbiology system". Accessed: 2025-04-25. [Online]. Available: https://www.idexx.com/en/water/other-products-services/tecta-water-microbiology-system/

[12] Q. A. Pankhurst, J. Connolly, S. K. Jones, and J. Dobson, "Applications of magnetic nanoparticles in biomedicine", *Journal of Physics D: Applied Physics*, vol. 36, no. 13, R167–R181, Jul. 2003, ISSN: 0022-3727, 1361-6463. DOI: 10.1088/0022-3727/36/13/201 Accessed: Mar. 16, 2024. [Online]. Available: https://iopscience.iop.org/article/10.1088/0022-3727/36/13/201

[13] J. Chomoucka, J. Drbohlavova, D. Huska, V. Adam, R. Kizek, and J. Hubalek, "Magnetic nanoparticles and targeted drug delivering", *Pharmacological Research*, vol. 62, no. 2, pp. 144–149, Aug. 2010, ISSN: 10436618. DOI: 10.1016/j.phrs.2010.01.014 Accessed: Jun. 3, 2025. [Online]. Available: https://linkinghub.elsevier.com/retrieve/pii/S1043661810000289

[14] S. Lyer, R. Singh, R. Tietze, and C. Alexiou, "Magnetic nanoparticles for magnetic drug targeting", *Biomedical Engineering / Biomedizinische Technik*, vol. 60, no. 5, Jan. 2015, ISSN: 1862-278X, 0013-5585. DOI: 10.1515/bmt-2015-0049 Accessed: Jun. 3, 2025. [Online]. Available: https://www.degruyter.com/document/doi/10.1515/bmt-2015-0049/html

[15] K. Khoshnevisan, E. Poorakbar, H. Baharifar, and M. Barkhi, "Recent Advances of Cellulase Immobilization onto Magnetic Nanoparticles: An Update Review", *Magnetochemistry*, vol. 5, no. 2, p. 36, Jun. 2019, ISSN: 2312-7481. DOI: 10.3390/magnetochemistry5020036 Accessed: Jun. 3, 2025. [Online]. Available: https://www.mdpi.com/2312-7481/5/2/36

[16] E. Katz, "Magnetic Nanoparticles", *Magnetochemistry*, vol. 6, no. 1, p. 6, Jan. 2020, ISSN: 2312-7481. DOI: 10.3390/magnetochemistry6010006 Accessed: Jun. 3, 2025. [Online]. Available: https://www.mdpi.com/2312-7481/6/1/6

[17] S. Laurent, S. Dutz, U. O. Häfeli, and M. Mahmoudi, "Magnetic fluid hyperthermia: Focus on superparamagnetic iron oxide nanoparticles", *Advances in Colloid and Interface Science*, vol. 166, no. 1-2, pp. 8–23, Aug. 2011, ISSN: 00018686. DOI: 10.1016/j.cis.2011.04.003 Accessed: Jun. 2, 2025. [Online]. Available: https://linkinghub.elsevier.com/retrieve/pii/S0001868611000972

[18] S. V. Spirou, M. Basini, A. Lascialfari, C. Sangregorio, and C. Innocenti, "Magnetic Hyperthermia and Radiation Therapy: Radiobiological Principles and Current Practice †", *Nanomaterials*, vol. 8, no. 6, p. 401, Jun. 2018, ISSN: 2079-4991. DOI: 10.3390/nano8060401 Accessed: Jun. 3, 2025. [Online]. Available: https://www.mdpi.com/2079-4991/8/6/401

[19] D. Chang et al., "Biologically Targeted Magnetic Hyperthermia: Potential and Limitations", *Frontiers in Pharmacology*, vol. 9, p. 831, Aug. 2018, ISSN: 1663-9812. DOI: 10.3389/fphar.2018.00831 Accessed: Jun. 3, 2025. [Online]. Available: https://www.frontiersin.org/article/10.3389/fphar.2018.00831/full

[20] A. Jordan, R. Scholz, P. Wust, H. Fähling, and Roland Felix, "Magnetic fluid hyperthermia (MFH): Cancer treatment with AC magnetic field induced excitation of biocompatible superparamagnetic nanoparticles", *Journal of Magnetism and Magnetic Materials*, vol. 201, no. 1-3, pp. 413–419, Jul. 1999, ISSN: 03048853. DOI: 10.1016/S0304-8853(99)00088-8 Accessed: Jun. 2, 2025. [Online]. Available: https://linkinghub.elsevier.com/retrieve/pii/S0304885399000888

[21] U. M. Engelmann, *Assessing Magnetic Fluid Hyperthermia: Magnetic Relaxation Simulation, Modeling of Nanoparticle Uptake inside Pancreatic Tumor Cells and in Vitro Efficacy*. Lübeck: Infinite Science Publishing, 2019, ISBN: 978-3-945954-58-4.

[22] R. S. Chaughule, S. Purushotham, and R. V. Ramanujan, "Magnetic Nanoparticles as Contrast Agents for Magnetic Resonance Imaging", *Proceedings of the National Academy of Sciences, India Section A: Physical Sciences*, vol. 82, no. 3, pp. 257–268, Sep. 2012, ISSN: 0369-8203, 2250-1762. DOI: 10.1007/s40010-012-0038-4 Accessed: Jun. 6, 2025. [Online]. Available: http://link.springer.com/10.1007/s40010-012-0038-4

[23] J. Gallo, N. J. Long, and E. O. Aboagye, "Magnetic nanoparticles as contrast agents in the diagnosis and treatment of cancer", *Chemical Society Reviews*, vol. 42, no. 19, p. 7816, 2013, ISSN: 0306-0012, 1460-4744. DOI: 10.1039/c3cs60149h Accessed: Jun. 6, 2025. [Online]. Available: https://xlink.rsc.org/?DOI=c3cs60149h

[24] C. Felton, A. Karmakar, Y. Gartia, P. Ramidi, A. S. Biris, and A. Ghosh, "Magnetic nanoparticles as contrast agents in biomedical imaging: Recent advances in iron- and manganese-based magnetic nanoparticles", *Drug Metabolism Reviews*, vol. 46, no. 2, pp. 142–154, May 2014, ISSN: 0360-2532, 1097-9883. DOI: 10.3109/03602532.2013.876429 Accessed: Jun. 6, 2025. [Online]. Available: http://www.tandfonline.com/doi/full/10.3109/03602532.2013.876429

[25] A. Avasthi, C. Caro, E. Pozo-Torres, M. P. Leal, and M. L. García-Martín, "Magnetic Nanoparticles as MRI Contrast Agents", *Topics in Current Chemistry*, vol. 378, no. 3, p. 40, Jun. 2020, ISSN: 2365-0869, 2364-8961. DOI: 10.1007/s41061-020-00302-w Accessed: Jun. 6, 2025. [Online]. Available: https://link.springer.com/10.1007/s41061-020-00302-w

[26] J. He, M. Huang, D. Wang, Z. Zhang, and G. Li, "Magnetic separation techniques in sample preparation for biological analysis: A review", *Journal of Pharmaceutical and Biomedical Analysis*, vol. 101, pp. 84–101, Dec. 2014, ISSN: 07317085. DOI: 10.1016/j.jpba.2014.04.017 Accessed: Jun. 6, 2025. [Online]. Available: https://linkinghub.elsevier.com/retrieve/pii/S0731708514002088

[27] M. Iranmanesh and J. Hulliger, "Magnetic separation: Its application in mining, waste purification, medicine, biochemistry and chemistry", *Chemical Society Reviews*, vol. 46, no. 19, pp. 5925–5934, 2017, ISSN: 0306-0012, 1460-4744. DOI: 10.1039/C7CS00230K Accessed: Jun. 6, 2025. [Online]. Available: https://xlink.rsc.org/?DOI=C7CS00230K

[28] K. Wu et al., "Magnetic nanoparticles and magnetic particle spectroscopy-based bioassays: A 15 year recap", *Nano Futures*, vol. 6, no. 2, p. 022 001, Jun. 2022, ISSN: 2399-1984. DOI: 10.1088/2399-1984/ac5cd1 Accessed: Jun. 3, 2025. [Online]. Available: https://iopscience.iop.org/article/10.1088/2399-1984/ac5cd1

[29] S. Carinelli, M. Luis-Sunga, J. L. González-Mora, and P. A. Salazar-Carballo, "Synthesis and Modification of Magnetic Nanoparticles for Biosensing and Bioassay Applications: A Review", *Chemosensors*, vol. 11, no. 10, p. 533, Oct. 2023, ISSN: 2227-9040. DOI: 10.3390/chemosensors11100533 Accessed: Jun. 3, 2025. [Online]. Available: https://www.mdpi.com/2227-9040/11/10/533

[30] F. Öisjöen, J. F. Schneiderman, A. P. Astalan, A. Kalabukhov, C. Johansson, and D. Winkler, "A new approach for bioassays based on frequency- and time-domain measurements of magnetic nanoparticles", *Biosensors and Bioelectronics*, vol. 25, no. 5, pp. 1008–1013, Jan. 2010, ISSN: 09565663. DOI: 10.1016/j.bios.2009.09.013 Accessed: Jun. 3, 2025. [Online]. Available: https://linkinghub.elsevier.com/retrieve/pii/S0956566309005004

[31] F. Janicek, A. Cerman, M. Perny, I. Brilla, L. Marko, and S. Motycak, "Applications of superconducting quantum interference devices", in *2015 16th International Scientific Conference on Electric Power Engineering (EPE)*, Kouty nad Desnou, Czech Republic: IEEE, May 2015, pp. 429–432, ISBN: 978-1-4673-6788-2. DOI: 10.1109/EPE.2015.7161204 Accessed: Jun. 6, 2025. [Online]. Available: http://ieeexplore.ieee.org/document/7161204/

[32] C.-B. Kim, E.-G. Lim, S. W. Shin, H. J. Krause, and H. Hong, "Magnetic immunoassay platform based on the planar frequency mixing magnetic technique", *Biosensors and Bioelectronics*, vol. 83, pp. 293–299, Sep. 2016, ISSN: 09565663. DOI: 10.1016/j.bios.2016.04.076 Accessed: Jun. 3, 2025. [Online]. Available: https://linkinghub.elsevier.com/retrieve/pii/S0956566316303517

[33] K. Wu et al., "A Portable Magnetic Particle Spectrometer for Future Rapid and Wash-Free Bioassays", *ACS Applied Materials & Interfaces*, vol. 13, no. 7, pp. 7966–7976, Feb. 2021, ISSN: 1944-8244, 1944-8252. DOI: 10.1021/acsami.0c21040 Accessed: Jun. 3, 2025. [Online]. Available: https://pubs.acs.org/doi/10.1021/acsami.0c21040

[34] V. K. Chugh, S. Liang, P. Yari, K. Wu, and J.-P. Wang, "A method for multiplexed and volumetric-based magnetic particle spectroscopy bioassay: Mathematical study", *Journal of Physics D: Applied Physics*, vol. 56, no. 31, p. 315 001, Aug. 2023, ISSN: 0022-3727, 1361-6463. DOI: 10.1088/1361-6463/acd0bd Accessed: Jun. 3, 2025. [Online]. Available: https://iopscience.iop.org/article/10.1088/1361-6463/acd0bd

[35] A. M. Rauwerdink, A. J. Giustini, and J. B. Weaver, "Simultaneous quantification of multiple magnetic nanoparticles", *Nanotechnology*, vol. 21, no. 45, p. 455 101, Nov. 2010, ISSN: 1361-6528. DOI: 10.1088/0957-4484/21/45/455101

[36] L. Tu, K. Wu, T. Klein, and J.-P. Wang, "Magnetic nanoparticles colourization by a mixing-frequency method", *Journal of Physics D: Applied Physics*, vol. 47, no. 15, p. 155 001, Apr. 2014, ISSN: 0022-3727, 1361-6463. DOI: 10.1088/0022-3727/47/15/155001 Accessed: May 19, 2025. [Online]. Available: https://iopscience.iop.org/article/10.1088/0022-3727/47/15/155001

[37] S. Achtsnicht, A. M. Pourshahidi, A. Offenhäusser, and H.-J. Krause, "Multiplex Detection of Different Magnetic Beads Using Frequency Scanning in Magnetic Frequency Mixing Technique", *Sensors*, vol. 19, no. 11, p. 2599, Jun. 2019, ISSN: 1424-8220. DOI: 10.3390/s19112599 Accessed: May 6, 2024.

[38] K. Wu, Y. Wang, Y. Feng, L. Yu, and J.-P. Wang, "Colorize magnetic nanoparticles using a search coil based testing method", *Journal of Magnetism and Magnetic Materials*, vol. 380, pp. 251–254, Apr. 2015, ISSN: 03048853. DOI: 10.1016/j.jmmm.2014.10.034 Accessed: Jun. 3, 2025. [Online]. Available: https://linkinghub.elsevier.com/retrieve/pii/S0304885314009342

[39] V. K. Chugh et al., "Magnetic Particle Spectroscopy with One-Stage Lock-In Implementation for Magnetic Bioassays with Improved Sensitivities", *The Journal of Physical Chemistry C*, vol. 125, no. 31, pp. 17 221–17 231, Aug. 2021, ISSN: 1932-7447, 1932-7455. DOI: 10.1021/acs.jpcc.1c05126 Accessed: Jun. 3, 2025. [Online]. Available: https://pubs.acs.org/doi/10.1021/acs.jpcc.1c05126

[40] A. V. Orlov, S. L. Znoyko, V. R. Cherkasov, M. P. Nikitin, and P. I. Nikitin, "Multiplex Biosensing Based on Highly Sensitive Magnetic Nanolabel Quantification: Rapid Detection of Botulinum Neurotoxins A, B, and E in Liquids", *Analytical Chemistry*, vol. 88, no. 21, pp. 10 419–10 426, Nov. 2016, ISSN: 1520-6882. DOI: 10.1021/acs.analchem.6b02066

[41] S. Achtsnicht et al., "3D Printed Modular Immunofiltration Columns for Frequency Mixing-Based Multiplex Magnetic Immunodetection", *Sensors*, vol. 19, no. 1, p. 148, Jan. 2019, ISSN: 1424-8220. DOI: 10.3390/s19010148 Accessed: May 12, 2025. [Online]. Available: https://www.mdpi.com/1424-8220/19/1/148

[42] H.-J. Krause et al., "Magnetic particle detection by frequency mixing for immunoassay applications", *Journal of Magnetism and Magnetic Materials*, vol. 311, no. 1, pp. 436–444, Apr. 2007, ISSN: 03048853. DOI: 10.1016/j.jmmm.2006.10.1164 Accessed: Nov. 25, 2023.

[43] P. I. Nikitin, P. M. Vetoshko, and T. I. Ksenevich, "New type of biosensor based on magnetic nanoparticle detection", en, *Journal of Magnetism and Magnetic Materials*, vol. 311, no. 1, pp. 445–449, Apr. 2007, ISSN: 03048853. DOI: 10.1016/j.jmmm.2006.10.1180 Accessed: Nov. 24, 2023. [Online]. Available: https://linkinghub.elsevier.com/retrieve/pii/S0304885306025789

[44] T. Bikulov, M.-B. Abbas, H.-J. Krause, A. Offenhäusser, and U. Engelmann, "Dual-frequency MPS enables direct MNP size reconstruction: Verification with micromagnetic simulation data", *International Journal on Magnetic Particle Imaging IJMPI*, vol. 11, no. 1 Suppl 1, Mar. 2025, Publisher: International Journal on Magnetic Particle Imaging IJMPI. DOI: 10.18416/IJMPI.2025.2503005 Accessed: Jun. 6, 2025. [Online]. Available: https://www.journal.iwmpi.org/index.php/iwmpi/article/view/837

[45] T. Bikulov, A. Offenhäusser, and H.-J. Krause, "Passive mixer model for multicontrast magnetic particle spectroscopy", *International Journal on Magnetic Particle Imaging IJMPI*, vol. 9, no. 1 Suppl 1, Mar. 2023, ISSN: 2365-9033. DOI: 10.18416/IJMPI.2023.2303087 Accessed: Apr. 12, 2024.

[46] T. Bikulov, F. Eivazi, A. Offenhäusser, and H.-J. Krause, "Multicontrasting MPS by dual-tone nonlinearity probing", *International Journal on Magnetic Particle Imaging IJMPI*, vol. 10, no. 1 Suppl 1, Mar. 2024. DOI: 10.18416/IJMPI.2024.2403014 Accessed: Sep. 28, 2024.

[47] J. Wells, H. Paysen, O. Kosch, L. Trahms, and F. Wiekhorst, "Temperature dependence in magnetic particle imaging", *AIP Advances*, vol. 8, no. 5, p. 056 703, May 2018, ISSN: 2158-3226. DOI: 10.1063/1.5004506 Accessed: May 13, 2025. [Online]. Available: https://pubs.aip.org/adv/article/8/5/056703/1021374/Temperature-dependence-in-magnetic-particle

[48] S. Draack, T. Viereck, C. Kuhlmann, M. Schilling, and F. Ludwig, "Temperature-dependent MPS measurements", *International Journal on Magnetic Particle Imaging*, vol. Vol.3, 4 pages, 2017, Artwork Size: 4 pages Publisher: Infinite Science Publishing, ISSN: 2365-9033. DOI: 10.18416/IJMPI.2017.1703018 Accessed: May 8, 2025. [Online]. Available: https://journal.iwmpi.org/index.php/iwmpi/article/view/66

[49] S. Draack, M. Schilling, and T. Viereck, "Magnetic particle imaging of particle dynamics in complex matrix systems", *Physical Sciences Reviews*, vol. 8, no. 2, pp. 213–237, Feb. 2023, ISSN: 2365-659X. DOI: 10.1515/psr-2019-0123 Accessed: May 13, 2025. [Online]. Available: https://www.degruyter.com/document/doi/10.1515/psr-2019-0123/html

[50] J. B. Weaver, A. M. Rauwerdink, and E. W. Hansen, "Magnetic nanoparticle temperature estimation", *Medical Physics*, vol. 36, no. 5, pp. 1822–1829, May 2009, ISSN: 0094-2405, 2473-4209. DOI: 10.1118/1.3106342 Accessed: Jun. 6, 2025. [Online]. Available: https://aapm.onlinelibrary.wiley.com/doi/10.1118/1.3106342

[51] M. Zhou et al., "Study of Magnetic Nanoparticle Spectrum for Magnetic Nanothermometry", *IEEE Transactions on Magnetics*, vol. 51, no. 9, pp. 1–6, Sep. 2015, ISSN: 0018-9464, 1941-0069. DOI: 10.1109/TMAG.2015.2434322 Accessed: Jun. 6, 2025. [Online]. Available: http://ieeexplore.ieee.org/document/7109877/

[52] J. Zhong, M. Schilling, and F. Ludwig, "Excitation frequency dependence of temperature resolution in magnetic nanoparticle temperature imaging with a scanning magnetic particle spectrometer", *Journal of Magnetism and Magnetic Materials*, vol. 471, pp. 340–345, Feb. 2019, ISSN: 03048853. DOI: 10.1016/j.jmmm.2018.09.112 Accessed: Oct. 21, 2024.

[53] R. Berger, J.-C. Bissey, J. Kliava, H. Daubric, and C. Estournès, "Temperature dependence of superparamagnetic resonance of iron oxide nanoparticles", *Journal of Magnetism and Magnetic Materials*, vol. 234, no. 3, pp. 535–544, Sep. 2001, ISSN: 03048853. DOI: 10.1016/S0304-8853(01)00347-X Accessed: Jun. 6, 2025. [Online]. Available: https://linkinghub.elsevier.com/retrieve/pii/S030488530100347X

[54] V. Blanco-Gutiérrez, E. Climent-Pascual, R. Sáez-Puche, and M. J. Torralvo-Fernández, "Temperature dependence of superparamagnetism in $CoFe_2O_4$ nanoparticles and $CoFe_2O_4$ /SiO_2 nanocomposites", *Physical Chemistry Chemical Physics*, vol. 18, no. 13, pp. 9186–9193, 2016, ISSN: 1463-9076, 1463-9084. DOI: 10.1039/C6CP00702C Accessed: Jun. 6, 2025. [Online]. Available: https://xlink.rsc.org/?DOI=C6CP00702C

[55] S. Kunikin, A. Zakinyan, and Y. Dikansky, "Temperature dependence of dynamic magnetic properties of superparamagnetic magnetite nanoparticles powder", *Journal of Magnetism and Magnetic Materials*, vol. 483, pp. 178–182, Aug. 2019, ISSN: 03048853. DOI: 10.1016/j.jmmm.2019.03.116 Accessed: Jun. 6, 2025. [Online]. Available: https://linkinghub.elsevier.com/retrieve/pii/S0304885318342100

[56] V. H. Ojha and K. M. Kant, "Temperature dependent magnetic properties of superparamagnetic CoFe2O4 nanoparticles", *Physica B: Condensed Matter*, vol. 567, pp. 87–94, Aug. 2019, ISSN: 09214526. DOI: 10.1016/j.physb.2019.04.035 Accessed: Jun. 6, 2025. [Online]. Available: https://linkinghub.elsevier.com/retrieve/pii/S0921452619302674

[57] V. K. Chugh, A. Di Girolamo, V. D. Krishna, K. Wu, M. C.-J. Cheeran, and J.-P. Wang, "Frequency and Amplitude Optimizations for Magnetic Particle Spectroscopy Applications", *The Journal of Physical Chemistry C*, vol. 127, no. 1, pp. 450–460, Jan. 2023, ISSN: 1932-7447, 1932-7455. DOI: 10.1021/acs.jpcc.2c07534 Accessed: Jun. 10, 2025. [Online]. Available: https://pubs.acs.org/doi/10.1021/acs.jpcc.2c07534

[58] A. M. Pourshahidi, S. Achtsnicht, A. Offenhäusser, and H.-J. Krause, "Frequency Mixing Magnetic Detection Setup Employing Permanent Ring Magnets as a Static Offset Field Source", *Sensors*, vol. 22, no. 22, p. 8776, Nov. 2022, ISSN: 1424-8220. DOI: 10.3390/s22228776 Accessed: Oct. 19, 2024.

[59] M. P. Jessing, A. Abuawad, T. Bikulov, J. R. Abresch, A. Offenhäusser, and H.-J. Krause, "Isothermal Amplification Using Temperature-Controlled Frequency Mixing Magnetic Detection-Based Portable Field-Testing Platform", *Sensors*, vol. 24, no. 14, p. 4478, Jul. 2024, ISSN: 1424-8220. DOI: 10.3390/s24144478 Accessed: Oct. 30, 2024.

[60] M. Jessing and H.-J. Krause, "Nanosonden basierte Schnellanalytik von Trinkwasser in Krisensituationen (NANObeST) – Teilvorhaben: Magnetische Detektion", Forschungszentrum Jülich GmbH Institut für Biologische Informationsprozesse (IBI-3), NANObeST Schlussbericht TIB Hannover 13N15253, 2022.

[61] S. Rettcher et al., "Simple and Portable Magnetic Immunoassay for Rapid Detection and Sensitive Quantification of Plant Viruses", *Applied and Environmental Microbiology*, vol. 81, no. 9, pp. 3039–3048, May 2015. DOI: 10.1128/AEM.03667-14 Accessed: Sep. 22, 2023.

[62] J. Pietschmann, H. Spiegel, H.-J. Krause, S. Schillberg, and F. Schröper, "Sensitive Aflatoxin B1 Detection Using Nanoparticle-Based Competitive Magnetic Immunodetection", *Toxins*, vol. 12, no. 5, p. 337, May 2020, ISSN: 2072-6651. DOI: 10.3390/toxins12050337 Accessed: May 29, 2024.

[63] A. Abuawad, Y. Ashhab, A. Offenhäusser, and H.-J. Krause, "DNA Sensor for the Detection of Brucella spp. Based on Magnetic Nanoparticle Markers", *International Journal of Molecular Sciences*, vol. 24, no. 24, p. 17 272, Dec. 2023, ISSN: 1422-0067. DOI: 10.3390/ijms242417272 Accessed: Oct. 30, 2024.

[64] J. Pietschmann et al., "Development of Fast and Portable Frequency Magnetic Mixing-Based Serological SARS-CoV-2-Specific Antibody Detection Assay", *Frontiers in Microbiology*, vol. 12, 2021, ISSN: 1664-302X. Accessed: Sep. 22, 2023.

[65] A. Aharoni, *Introduction to the Theory of Ferromagnetism*. Oxford University Press, 2000, ISBN: 978-0-19-850808-3.

[66] K. M. Krishnan, *Fundamentals and Applications of Magnetic Materials*. Oxford: Oxford university press, 2016, ISBN: 978-0-19-957044-7.

[67] C. Shasha and K. M. Krishnan, "Nonequilibrium Dynamics of Magnetic Nanoparticles with Applications in Biomedicine", *Advanced Materials*, vol. 33, no. 23, p. 1 904 131, Jun. 2021, ISSN: 0935-9648, 1521-4095. DOI: 10.1002/adma.201904131 Accessed: Nov. 30, 2023.

[68] J. M. D. Coey, *Magnetism and Magnetic Materials*, Repr. Cambridge: Cambridge Univ. Press, 2013, ISBN: 978-0-521-81614-4.

[69] A. P. Guimarães, *Principles of Nanomagnetism* (Nanoscience and Technology). Berlin Heidelberg: Springer, 2009, Literaturangaben, ISBN: 978-3-642-01481-9.

[70] P. Datta, "Magnetic gels", in *Polymeric Gels*, Elsevier, 2018, pp. 441–465, ISBN: 978-0-08-102179-8. DOI: 10.1016/B978-0-08-102179-8.00017-X Accessed: Jun. 23, 2025. [Online]. Available: https://linkinghub.elsevier.com/retrieve/pii/B978008102179800017X

[71] T. D. Clemons, R. H. Kerr, and A. Joos, "Multifunctional Magnetic Nanoparticles: Design, Synthesis, and Biomedical Applications", in *Comprehensive Nanoscience and Nanotechnology*, Elsevier, 2019, pp. 193–210, ISBN: 978-0-12-812296-9. DOI: 10.1016/B978-0-12-803581-8.10462-X Accessed: Jun. 23, 2025. [Online]. Available: https://linkinghub.elsevier.com/retrieve/pii/B978012803581810462X

[72] T. Knopp and T. M. Buzug, *Magnetic Particle Imaging: An Introduction to Imaging Principles and Scanner Instrumentation*. Heidelberg , New York Dordrecht London: Springer, 2012, Literaturangaben, ISBN: 978-3-642-04198-3.

[73] K. Wu, D. Su, R. Saha, J. Liu, V. K. Chugh, and J.-P. Wang, "Magnetic Particle Spectroscopy: A Short Review of Applications Using Magnetic Nanoparticles", *ACS Applied Nano Materials*, vol. 3, no. 6, pp. 4972–4989, Jun. 2020, ISSN: 2574-0970, 2574-0970. DOI: 10.1021/acsanm.0c00890 Accessed: Jan. 6, 2024.

[74] J. Rahmer, J. Weizenecker, B. Gleich, and J. Borgert, "Signal encoding in magnetic particle imaging: Properties of the system function", *BMC Medical Imaging*, vol. 9, no. 1, p. 4, Dec. 2009, ISSN: 1471-2342. DOI: 10.1186/1471-2342-9-4 Accessed: Jan. 6, 2024.

[75] T. Knopp et al., "Model-Based Reconstruction for Magnetic Particle Imaging", *IEEE Transactions on Medical Imaging*, vol. 29, no. 1, pp. 12–18, Jan. 2010, ISSN: 0278-0062, 1558-254X. DOI: 10.1109/TMI.2009.2021612 Accessed: Jan. 6, 2024.

[76] J. Rahmer, J. Weizenecker, B. Gleich, and J. Borgert, "Analysis of a 3-D System Function Measured for Magnetic Particle Imaging", *IEEE Transactions on Medical Imaging*, vol. 31, no. 6, pp. 1289–1299, Jun. 2012, ISSN: 0278-0062, 1558-254X. DOI: 10.1109/TMI.2012.2188639 Accessed: Jan. 6, 2024.

[77] H.-J. Krause and U. M. Engelmann, "Fundamentals and Applications of Dual-Frequency Magnetic Particle Spectroscopy: Review for Biomedicine and Materials Characterization", *Advanced Science*, vol. 12, no. 13, p. 2 416 838, Apr. 2025, ISSN: 2198-3844, 2198-3844. DOI: 10.1002/advs.202416838 Accessed: May 13, 2025. [Online]. Available: https://advanced.onlinelibrary.wiley.com/doi/10.1002/advs.202416838

[78] A. M. Pourshahidi, S. Achtsnicht, M. M. Nambipareechee, A. Offenhäusser, and H.-J. Krause, "Multiplex Detection of Magnetic Beads Using Offset Field Dependent Frequency Mixing Magnetic Detection", *Sensors*, vol. 21, no. 17, p. 5859, Aug. 2021, ISSN: 1424-8220. DOI: 10.3390/s21175859 Accessed: Oct. 19, 2024.

[79] U. M. Engelmann, B. Simsek, A. Shalaby, and H.-J. Krause, "Key Contributors to Signal Generation in Frequency Mixing Magnetic Detection (FMMD): An In Silico Study", *Sensors*, vol. 24, no. 6, p. 1945, Mar. 2024, ISSN: 1424-8220. DOI: 10.3390/s24061945 Accessed: Oct. 21, 2024.

[80] Q. Wang et al., "Simulation of a single-sided MPI handheld device with offset magnetic field for spatial encoding", *International Journal on Magnetic Particle Imaging IJMPI*, vol. 10, no. 1 Suppl 1, Mar. 2024, Publisher: International Journal on Magnetic Particle Imaging IJMPI. DOI: 10.18416/IJMPI.2024.2403041 Accessed: May 19, 2025. [Online]. Available: https://www.journal.iwmpi.org/index.php/iwmpi/article/view/755

[81] J. H. Lienhard, *A Heat Transfer Textbook*, Fifth edition. New York: Dover Publications, 2020, ISBN: 978-0-486-83735-2.

[82] J. P. Holman, *Heat Transfer* (McGraw-Hill Series in Mechanical Engineering), 10th ed. Boston: McGraw Hill Higher Education, 2010, ISBN: 978-0-07-352936-3.

[83] T. L. Bergman, A. S. Lavine, F. Incropera, and D. P. DeWitt, *Fundamentals of Heat and Mass Transfer*. Wiley, 2020, OCLC: 1464846710, ISBN: 978-1-119-72248-9.

[84] *Thermal insulation and energy economy in buildings — part 4: Hygrothermal design values*, Berlin: DIN Deutsches Institut für Normung e.V., Nov. 2020.

[85] Y. S. Touloukian, P. E. Liley, and S. C. Saxena, *Thermophysical Properties of Matter, Vol. 3: Thermal Conductivity*. New York: IFI/Plenum Press, 1970.

[86] Y. A. Çengel and J. M. Cimbala, *Fluid Mechanics: Fundamentals and Applications*, 3rd ed. New York: McGraw-Hill Education, 2014, Appendix A, Table A–9: Properties of air at 1 atm pressure.

[87] F. P. Incropera, D. P. DeWitt, T. L. Bergman, and A. S. Lavine, Eds., *Principles of Heat and Mass Transfer*, 7. ed., international student version. Hoboken, NJ: Wiley, 2013, Abweichender Titel der internationalen Ausg. - US-Ausg. weiterhin u.d.T.: Fundamentals of heat and mass transfer, ISBN: 978-0-470-50197-9.

[88] S. S. Goodrich and W. R. Marcum, "Natural convection heat transfer and boundary layer transition for vertical heated cylinders", *Experimental Thermal and Fluid Science*, vol. 105, pp. 367–380, Jul. 2019, ISSN: 08941777. DOI: 10.1016/j.expthermflusci.2019.04.010 Accessed: Oct. 12, 2023.

[89] R. P. Schaudies, *Biological identification: DNA amplification and sequencing, optical sensing, lab-on-chip and portable systems* (Woodhead Publishing series in electronic and optical materials number 59), eng. Amsterdam: Elsevier Woodhead Publishing, 2014, ISBN: 978-0-85709-501-5.

[90] R. K. Saiki et al., "Primer-Directed Enzymatic Amplification of DNA with a Thermostable DNA Polymerase", en, *Science*, vol. 239, no. 4839, pp. 487–491, Jan. 1988, ISSN: 0036-8075, 1095-9203. DOI: 10.1126/science.2448875 Accessed: Feb. 27, 2025. [Online]. Available: https://www.science.org/doi/10.1126/science.2448875

[91] C. Mülhardt, *Der Experimentator Molekularbiologie/Genomics*, de. Berlin, Heidelberg: Springer Berlin Heidelberg, 2013, ISBN: 978-3-642-34635-4 978-3-642-34636-1. DOI: 10.1007/978-3-642-34636-1 Accessed: Feb. 27, 2025. [Online]. Available: http://link.springer.com/10.1007/978-3-642-34636-1

[92] T. Koressaar and M. Remm, "Enhancements and modifications of primer design program Primer3", en, *Bioinformatics*, vol. 23, no. 10, pp. 1289–1291, May 2007, ISSN: 1367-4811, 1367-4803. DOI: 10.1093/bioinformatics/btm091 Accessed: Feb. 27, 2025. [Online]. Available: https://academic.oup.com/bioinformatics/article/23/10/1289/197299

[93] Ivan Magriñá Lobato and Ciara K. O'Sullivan, "Recombinase polymerase amplification: Basics, applications and recent advances", *Trends in Analytical Chemistry*, vol. 98, pp. 19–35, Jan. 2018. DOI: 10.1016/j.trac.2017.10.015

[94] S. Achtsnicht, "Multiplex-Magnetdetektion von superparamagnetischen Beads zur Identifizierung von Trinkwasserkontaminationen", Ph.D. dissertation, RWTH Aachen University, 2020.

[95] G. H. Hostetter, H. J. Lane, and R. T. Stefani, "Engineering Circuit Analysis Jack E. Kemmerly William H. Hayt", *IEEE Transactions on Education*, vol. 20, no. 2, pp. 120–120, May 1977, ISSN: 0018-9359, 1557-9638. DOI: 10.1109/TE.1977.4321132 Accessed: Oct. 19, 2024.

[96] A. M. Pourshahidi, "Frequency mixing magnetic detection for characterization and multiplex detection of superparamagnetic nanoparticles", Monographie, RWTH Aachen University, 2023.

[97] U. M. Engelmann, A. Shalaby, C. Shasha, K. M. Krishnan, and H.-J. Krause, "Comparative Modeling of Frequency Mixing Measurements of Magnetic Nanoparticles Using Micromagnetic Simulations and Langevin Theory", *Nanomaterials*, vol. 11, no. 5, p. 1257, May 2021, ISSN: 2079-4991. DOI: 10.3390/nano11051257 Accessed: Oct. 21, 2024.

[98] M. Rosenblatt, "Remarks on Some Nonparametric Estimates of a Density Function", *The Annals of Mathematical Statistics*, vol. 27, no. 3, pp. 832–837, Sep. 1956, ISSN: 0003-4851. DOI: 10.1214/aoms/1177728190 Accessed: Oct. 21, 2024.

[99] E. Parzen, "On Estimation of a Probability Density Function and Mode", *The Annals of Mathematical Statistics*, vol. 33, no. 3, pp. 1065–1076, Sep. 1962, ISSN: 0003-4851. DOI: 10.1214/aoms/1177704472 Accessed: Oct. 21, 2024.

[100] B. W. Silverman, *Density Estimation for Statistics and Data Analysis* (Chapman and Hall/CRC Monographs on Statistics and Applied Probability v.26). Boca Raton: Routledge, 1986, ISBN: 978-0-412-24620-3.

[101] S. Achtsnicht et al., "Sensitive and rapid detection of cholera toxin subunit B using magnetic frequency mixing detection", *PLOS ONE*, vol. 14, no. 7, J. Chalmers, Ed., e0219356, Jul. 2019, ISSN: 1932-6203. DOI: 10.1371/journal.pone.0219356 Accessed: Sep. 22, 2023.

[102] U. Erhardt and C. Erhardt, "Carrier material loadable by a through flow for solid phase assays", Patent WO1997028448A1, Jan. 1997.

[103] H. Hartmann, B. Lübbers, M. Casaretto, W. Bautsch, A. Klos, and J. Köhl, "Rapid quantification of C3a and C5a using a combination of chromatographic and immunoassay procedures", *Journal of Immunological Methods*, vol. 166, no. 1, pp. 35–44, Nov. 1993, ISSN: 00221759. DOI: 10.1016/0022-1759(93)90326-3 Accessed: Apr. 24, 2025. [Online]. Available: https://linkinghub.elsevier.com/retrieve/pii/0022175993903263

[104] A. Lucht et al., "Development of an Immunofiltration-Based Antigen-Detection Assay for Rapid Diagnosis of Ebola Virus Infection", *The Journal of Infectious Diseases*, vol. 196, no. s2, S184–S192, Nov. 2007, ISSN: 0022-1899, 1537-6613. DOI: 10.1086/520593 Accessed: Apr. 24, 2025. [Online]. Available: https://academic.oup.com/jid/article-lookup/doi/10.1086/520593

[105] J. Pietschmann, D. Dittmann, H. Spiegel, H.-J. Krause, and F. Schröper, "A Novel Method for Antibiotic Detection in Milk Based on Competitive Magnetic Immunodetection", *Foods*, vol. 9, no. 12, p. 1773, Dec. 2020, ISSN: 2304-8158. DOI: 10.3390/foods9121773 Accessed: Sep. 22, 2023.

[106] Florian Schröper, Jan Pietschmann, *Standardarbeitsanweisung: Durchführung Sandwich/Competitive MID Assay*, Interne SOP-Version, Gruppe für Innovative Detektionstechnologien des Fraunhofer IME, Aachen, 2022.

[107] G. Nellis and S. Klein, *Heat Transfer*, 1st ed. Cambridge University Press, Dec. 2008, ISBN: 978-0-521-88107-4. DOI: 10.1017/CBO9780511841606 Accessed: Sep. 2, 2025. [Online]. Available: https://www.cambridge.org/core/product/identifier/9780511841606/type/book

[108] Krzysztof Oprzedkiewicz and Wojciech Mitkowski, "Accuracy Analysis for Fractional Order Transfer Function Models with Delay", in *Theory and Applications of Non-integer Order Systems*, ser. Lecture Notes in Electrical Engineering (LNEE), vol. 407, Springer International Publishing, 2017.

[109] F. N. Deniz, B. B. Alagoz, N. Tan, and M. Koseoglu, "Revisiting four approximation methods for fractional order transfer function implementations: Stability preservation, time and frequency response matching analyses", *Annual Reviews in Control*, vol. 49, pp. 239–257, Jan. 2020, ISSN: 1367-5788. DOI: 10.1016/j.arcontrol.2020.03.003 Accessed: Apr. 16, 2024.

[110] C. Lisciandra and J. Korbmacher, "Multiple models, one explanation", *Journal of Economic Methodology*, vol. 28, no. 2, pp. 186–206, Apr. 2021, ISSN: 1350-178X, 1469-9427. DOI: 10.1080/1350178X.2021.1892800 Accessed: May 24, 2025. [Online]. Available: https://www.tandfonline.com/doi/full/10.1080/1350178X.2021.1892800

[111] COMSOL AB. "Heat transfer module user's guide". Accessed: 2025-02-25. [Online]. Available: https://doc.comsol.com/5.5/doc/com.comsol.help.heat/heat_ug_ht_features.09.075.html

[112] COMSOL AB. "Ac/dc module user's guide". Accessed: 2025-02-25. [Online]. Available: https://doc.comsol.com/5.5/doc/com.comsol.help.comsol/comsol_ref_acdc.17.74.html

[113] Krzysztof Oprzedkiewicz and Wojciech Mitkowski, "Accuracy Analysis for Fractional Order Transfer Function Models with Delay", in *Theory and Applications of Non-integer Order Systems*, ser. Lecture Notes in Electrical Engineering (LNEE), vol. 407, Springer International Publishing, 2017.

[114] A. A. E. Wahed et al., "Recombinase Polymerase Amplification Assay for Rapid Diagnostics of Dengue Infection", *PLOS ONE*, vol. 10, no. 6, e0129682, Jun. 2015, ISSN: 1932-6203. DOI: 10.1371/journal.pone.0129682 Accessed: Apr. 12, 2024.

[115] A. Larrea-Sarmiento, J. P. Stack, A. M. Alvarez, and M. Arif, "Multiplex recombinase polymerase amplification assay developed using unique genomic regions for rapid on-site detection of genus Clavibacter and C. nebraskensis", *Scientific Reports*, vol. 11, no. 1, p. 12 017, Jun. 2021, ISSN: 2045-2322. DOI: 10.1038/s41598-021-91336-7 Accessed: Apr. 12, 2024.

[116] B. B. Oliveira, B. Veigas, and P. V. Baptista, "Isothermal Amplification of Nucleic Acids: The Race for the Next "Gold Standard"", *Frontiers in Sensors*, vol. 2, 2021, ISSN: 2673-5067. Accessed: Sep. 22, 2023.

[117] A. James and J. Macdonald, "Recombinase polymerase amplification: Emergence as a critical molecular technology for rapid, low-resource diagnostics", *Expert Review of Molecular Diagnostics*, vol. 15, no. 11, pp. 1475–1489, Nov. 2015, ISSN: 1473-7159, 1744-8352. DOI: 10.1586/14737159.2015.1090877 Accessed: Oct. 30, 2024.

[118] "Thermophysical properties of fluid systems", National Institute of Standards and Technology (NIST), Accessed: Sep. 6, 2025. [Online]. Available: https://webbook.nist.gov/chemistry/fluid/

[119] S. W. Churchill and H. H. Chu, "Correlating equations for laminar and turbulent free convection from a horizontal cylinder", *International Journal of Heat and Mass Transfer*, vol. 18, no. 9, pp. 1049–1053, Sep. 1975, ISSN: 00179310. DOI: 10.1016/0017-9310(75)90222-7 Accessed: Sep. 6, 2025. [Online]. Available: https://linkinghub.elsevier.com/retrieve/pii/0017931075902227

[120] S. W. Churchill and R. Usagi, "A general expression for the correlation of rates of transfer and other phenomena", *AIChE Journal*, vol. 18, no. 6, pp. 1121–1128, Nov. 1972, ISSN: 0001-1541, 1547-5905. DOI: 10.1002/aic.690180606 Accessed: Sep. 6, 2025. [Online]. Available: https://aiche.onlinelibrary.wiley.com/doi/10.1002/aic.690180606

Acknowledgements

Zuallererst möchte ich meinem Doktorvater **Prof. Dr. Andreas Offenhäusser**, dem Leiter des Instituts für Biologische Informationsverarbeitung (IBI-3), für die Möglichkeit danken, meine Promotion an der von Ihm geleiteten Einrichtung durchführen zu dürfen, sowie für das sorgfältige Korrekturlesen meiner Dissertation.

Ein besonders herzlicher Dank gilt meinem vor-Ort Betreuer **Prof. Dr. Hans-Joachim Krause**. Du standest jederzeit für Fragen zur Verfügung, bist allen Mitgliedern der Gruppe stets mit großem Respekt begegnet und hast nie Druck ausgeübt. Vielen Dank, dass Du mir sowohl auf persönlicher als auch auf wissenschaftlicher Ebene viel Freiraum gelassen hast. Ich bin überzeugt, im Namen der gesamten Arbeitsgruppe für Magnetsensorik zu sprechen, wenn ich mich herzlich für die Unterstützung bedanke. Danke auch für das mehrmahlige Korrekturlesen meiner Dissertation!

So möchte ich auch gerne **Prof. Dr. Jörg Fitter** danken, der freundlicherweise die Rolle des Zweitprüfers übernommen hat.

Ebenso möchte ich meinen Kolleginnen und Kollegen **Timur Bikulov**, **Faranak Eivazi**, **Abdalhalim Abuawad**, **Ali Pourshahidi** und **Dieter Lomparski**, dem Ingenieur der Arbeitsgruppe für Magnetsensorik, meinen Dank aussprechen.

First, I would like to thank **Tim**. Thank you so much for both the personal and professional exchange we've had. During our time at the Forschungszentrum, you've become a friend. No matter the ups and downs, I've always valued our relationship and everything we've worked toward together. I've learned a lot from you, and I'll do my best to build on that knowledge!

Dear **Faranak**, thank you for the many walks and talks we had and thank you for being a good friend. I always really enjoyed sharing experiences and ideas with you. I appreciate our relationship and I wish you all the best. I hope we will stay in contact.

Abed, thank you very much for our collaboration. I enjoyed the work on our joint journal article and the many ideas we've discussed. Thank you for being such a great colleague and friend.

Ein großer Dank geht auch an **Dieter**. Danke für deine Hilfe bei technischen Zeichnungen! Die vielen entspannten Gespräche beim Kaffee haben dafür gesorgt, das man sich bei euch sehr wohl gefühlt hat. Wir hatten viel Spass! Ich wünsche dir alles Gute.

Ebenfalls möchte ich sowohl **Dieter**, **Tim** aber auch **Jan Abresch** und **Phil Schmieder** (unseren MATSE's) für die programmatische Unterstützung danken.

Danke an **Ali** und **Stefan Achtsnicht** für die Einführung in die Messaparaturen zu Beginn meiner Zeit am Forschungszentrum.

Des Weiteren geht ein ganz besonderer Dank an **Dr. Ulrich Engelmann**. Du hast dir immer wieder Zeit für mich genommen, mir Mut zugesprochen und mir mögliche Wege für mein weiteres Vorgehen aufgezeigt. Ich würde mich freuen, weiterhin Kontakt mit dir zu halten!

Vielen herzlichen Dank auch an **Niklas**, **Mike**, **Sylvia** und **Thomas Dienstbier**. Eure ganze Familie ist mir sehr wichtig und ich bin dankbar für die vielen Aufmunterungen. **Nik** und **Mike**, Euch bin ich besonders dankbar für die viele Zeit, die Ihr mir geschenkt habt und in der Ihr mir zugehört und geholfen habt.

Rebecca Siwek, meine Leidensgenossin! Vielen Dank für die regelmäßigen Gespräche über unsere Ergebnisse. Danke für unsere Treffen im "virtuellen Büro" um an unseren Dissertationen zu arbeiten. Klasse, wie wir uns gegenseitig immer wieder motivieren konnten.

Danke an den Gruppenleiter für Innovative Detektionstechnologien am Fraunhofer IME **Dr. Florian Schröper** und auch an **Dr. Jan Pietschmann** für die angenehme Zusammenarbeit im NANObeST Projekt. Danke auch an das Fraunhofer Institut IME in Aachen für die Infrastruktur, die uns für etwaige Experimente zur Verfügung gestellt wurde. Ein spezieller Dank geht an **Maria Stroot** - Danke für die netten Gespräche und die Zusammenarbeit bei der Durchführung magnetischer Immunoassays!

Großer Dank gilt dementsprechend natürlich auch den Projektpartnern des THW. Speziell **Dr. Angela Kaltenbach** möchte ich danken, die in Zusammenarbeit mit **Prof. Dr. Hans-Joachim Krause** das Projekt koordiniert hat. Liebe **Angela**, danke vor allem auch für die Organisation des Messestandes auf der INTERSCHUTZ in Hannover, bei der wir gemeinsam den magnetischen Reader vorführen konnten. **Felix Klinke**, **Christiane Bettin** und auch allen anderen hier nicht explizit genannten Teilnehmern an den Projektmeetings danke ich für den regen Austausch und die freundliche Zusammenarbeit im NANObeST Projekt.

Selbstverständlich gilt meine Dankbarkeit auch den assoziierten Partnern **DITABIS Digital Biomedical Imaging Systems AG** und dem **Institut für Wasser- und Abwasseranalytik - IWA GmbH (IWA)**. Speziell hervorheben möchte ich allerdings **Micromod Partikeltechnologie GmbH** als Teil des Projektbeirates. Vielen Dank für die gemeinsamen Diskussionen und das Teilen von Magnetpartikelproben und Daten.

Der letzte Dank ist der persönlichste und zugleich wichtigste von allen. Er geht an die mir am Nahe stehendesten Menschen. Zunächst herzlichsten Dank an meine Eltern **Sabine** und **Michael**, die mich von Anfang an in dem Vorhaben zu Promovieren unterstützt haben und das durch Zeiten finanzieller aber auch persönlicher Unsicherheit hinweg. Danke auch an meine Geschwister. Vor allem aber möchte ich meine Partnerin **Thu Van** hervorheben. Es gibt keinen Menschen, mit dem ich lieber die Abende nach der Arbeit verbracht habe. Dein unerschütterlicher Optimismus, dein Verständnis und deine liebevolle Art sind maßgeblich dafür verantwortlich, dass ich diesen Abschnitt meines Lebens erfolgreich abschließen konnte!

Zum Schluss möchte ich noch sagen, dass ich die Erfahrungen, die ich während meiner Zeit

am Forschungszentrum gemacht habe sehr zu schätzen weiß. Nichts desto trotz freue ich mich auf den neuen Lebensabschnitt voller interessanter Themen aber ohne akademische Prüfungsleistungen!

Band / Volume 112
Software-Configurable Analog-To-Digital Converters for Configurable Pulse Detection
L. Krystofiak (2025), xvii, 113 pp, xxix
ISBN: 978-3-95806-826-1

Band / Volume 113
Development of Superparamagnetic Based Biological Sensor for the Detection of Brucella DNA Using Frequency Mixing Magnetic Detection
A. Abuawad (2025), X, 129 pp
ISBN: 978-3-95806-836-0

Band / Volume 114
A System for the Cryogenic Power Management of Quantum Computing Electronics: Development, Integration, and Test
A. R. Cabrera Galicia (2025), xxv, 110, lviii pp
ISBN: 978-3-95806-844-5

Band / Volume 115
Investigation of 2D Materials using Low Energy Electron Microscopy (LEEM)
H. Yin (2025) viii, 137 pp
ISBN: 978-3-95806-848-3

Band / Volume 116
Topotactic phase transition in $La_{0.6}Sr_{0.4}CoO_{3-\delta}$ thin films: oxygen content, dynamics and reversibility
S. He (2025) ix, 137 pp
ISBN: 978-3-95806-868-1

Band / Volume 117
Electrical anisotropy and shear-resistant topology in the quasi one-dimensional van-der-Waals material α-Bi_4Br_4
J.K. Hofmann (2025) xv, 129 pp
ISBN: 978-3-95806-869-8

Band / Volume 118
Spin-orbital mixing in the topological ladder of the two-dimensional metal $PtTe_2$
M. Qahosh (2025), ix, 170 pp
ISBN: 978-3-95806-872-8

Band / Volume 119
Functions of SNNs constrained by biology
A. Korcsak-Gorzo (2025), xvi, 145 pp
ISBN: 978-3-95806-876-6

Band / Volume 120
On Scalable Integrated Charge State Tuning for Semiconductor Quantum Dot Devices
F. A. Hader (2026), xx, 145 pp
ISBN: 978-3-95806-884-1

Band / Volume 121
Efficient Massively Space-Time-Parallel Simulations with Adaptive Spectral Deferred Correction
T. Saupe (2026), v, 149 pp
ISBN: 978-3-95806-886-5

Band / Volume 122
Controlled single-molecule manipulation
P. Kopp (2026), viii, 136 pp
ISBN: 978-3-95806-887-2

Band / Volume 123
Growth and Excitation Dynamics of Epitaxial 2D Materials and Molecular Layers Studied by Electron and Momentum Microscopy
M. E. Raths (2026), xvi, 161, XXIX pp
ISBN: 978-3-95806-892-6

Band / Volume 124
Ferroelectric and Resistive Switching in Epitaxial $Hf_{0.5}Zr_{0.5}O_2$
J. R. Knabe (2026), 145 pp
ISBN: 978-3-95806-895-7

Band / Volume 125
Temperature Influences on Frequency Mixing Magnetic Detection for mobile Drinking Water Analysis in Crisis Areas
M. Jessing (2026), xx, 113 pp
ISBN: 978-3-95806-902-2

Weitere ***Schriften des Verlags im Forschungszentrum Jülich*** unter
http://wwwzb1.fz-juelich.de/verlagextern1/index.asp

Information
Band / Volume 125
ISBN 978-3-95806-902-2

Mitglied der Helmholtz-Gemeinschaft

JÜLICH
Forschungszentrum